ELECTRICAL AND OPTICAL CHARACTERIZATION OF DEFECT LEVELS IN $Bi_{12}GeO_{20}$ AND $Bi_{12}SiO_{20}$

By

DANNING WILFORD BLOOM

Bachelor of Arts

St. Cloud State University

St. Cloud, Minnesota

1989

Submitted to the Faculty of the
Graduate College of the
Oklahoma State University
in partial fulfillment of
the requirements for
the Degree of
DOCTOR OF PHILOSOPHY
May, 1997

ELECTRICAL AND OPTICAL CHARACTERIZATION

OF DEFECT LEVELS IN $Bi_{12}GeO_{20}$

AND $Bi_{12}SiO_{20}$

Thesis Approved:

Thesis Advisor

Thomas C. Collins

Dean of the Graduate College

ACKNOWLEDGEMENTS

I have to thank a number of people for their help and support during this work, but first I would like to thank my advisor, Dr. Steve McKeever, for his supervision and guidance during this project. He was very understanding, even at times when I was going off in the wrong direction in my attempt to get things to work. In addition I would like to thank the physics department for providing me with continuous support of one kind or another during my graduate work. The office staff, Susan, Cheryl and, more recently, Mary, also deserve thanks for all the help they have given me throughout the years with various things.

I would like to thank Dr. Martin as he provided me with samples to perform measurements on. Without them this would have been a much shorter dissertation. I also have to thank Dr. Martin for letting me borrow (keep?) so much lab equipment and for letting me perform the photorefractive measurements in his lab.

I have a number of students to thank as well. First of all, Brian Markey was an invaluable help to me for my first couple of years in the lab. He always had time to answer my questions and drop whatever he was doing to help me if I needed it. Thanks Brian. I also want to thank all of my friends who made Oklahoma a much more bearable place to live. I don't want to mention names for fear of leaving someone out.

Finally I would like to thank my parents for their continual love, support and free mountain biking trips to Colorado. They made home a nice place to escape to when I could get away.

TABLE OF CONTENTS

LIST OF TABLES

LIST OF FIGURES

Chapter 1

Introduction

$Bi_{12}GeO_{20}$ (BGO) and $Bi_{12}SiO_{20}$ (BSO) are two related materials which have potential for use in applications such as optical data storage, filtering, optical computing, holography, two-beam coupling, beam amplification and many others due to their photorefractive properties. The photorefractive effect is a light-induced change in crystal's refractive index and was discovered in 1966 by researchers at Bell Laboratories [1]. The researchers observed that focusing a blue or green laser beam on a $LiNbO_3$ or $LiTaO_3$ crystal caused a change in refractive index. It was originally thought that the effect was detrimental to the optics of non-linear crystals, but it was later realized that the photorefractive effect had many applications. Since then the photorefractive effect has been observed in a great number of materials including ferroelectrics such as $BaTiO_3$ and $Sr_xBa_{1-x}Nb_2O_6$ (SBN), insulators such as BGO and BSO, semiconductors like GaAs, CdTe and InP and, more recently, organics [2].

The photorefractive effect is induced by illuminating the sample with nonuniform light, for example, the interference pattern generated by crossed laser beams. Under illumination of the proper wavelength charge is excited out of defect states to one or both of the delocalized bands in the bright regions of the sample where it is then free to drift and diffuse to the dark regions where it can be trapped. This redistribution of charge creates a space-charge field which deforms the lattice slightly and modulates the index of refraction via the electro-optic effect. In crystals which lack a center of

inversion symmetry the linear (Pockels) electro-optic effect is present and dominates the quadratic electro-optic effect which can be seen in non-centrosymmetric crystals.

One of the most exciting applications for photorefractive materials is as the storage medium in data storage devices. Holographic storage devices may provide many advantages in comparison to other storage media. For example, holographic storage devices have the potential to store huge amounts of information in a small photorefractive crystal. Diffraction limited storage densities in photorefractive media would approach terabytes per cubic centimeter [3] and this data could be read and written at rates of $\sim$10 Gbits/s or greater. Holographic storage devices also have an advantage over other storage media in that they are less sensitive to imperfections of the storage medium. In holographic storage the Fourier transform of the pattern of bits is stored, so each bit is stored throughout the medium rather than in one position. Rather than completely wiping out a series of bits dust, for example, would just decrease the signal-to-noise ratio overall.

An information storage device based on BSO was demonstrated in 1971 by Hou and Oliver [4]. Hou and Oliver built a Pockels Readout Optical Memory (PROM) using a single BSO crystal which was illuminated through a transparent electrode. The back electrode was made reflecting to cancel the optical activity of the crystal. An image was written using UV excitation to excite free electrons to the conduction band which then traveled under an applied voltage to the interfacial region between the electrode and dielectric film. This charge density depolarizes the voltage applied to the crystal in the illuminated regions, so that a voltage pattern mirroring the UV image is created. When the read beam passes through the crystal the parts of the beam which travel through regions where the depolarization charge density is present experience a different phase retardation than the light which travels through regions without the depolarization charge. After placing the sample between a pair of crossed

Glan Thompson prisms the light output is proportional to $\sin^2 \Gamma$ where Γ is the phase retardation. Both positive and negative images can be read depending on whether there is an applied voltage during reading. The image can be erased by exposing the device to UV with shorted electrodes. Dark storage times were found to be about 2 hours.

Several data storage devices utilizing photorefractive materials have been demonstrated [5,6]. Heanue et al. [5] showed that digital data can be stored and retrieved with high accuracy using $LiNbO_3$ as the storage medium. Bit error rates of 1 in 10^6 were achieved and the system was used to store and reconstruct the digital data representing an image of the Mona Lisa.

Data storage is only one of the possible applications of photorefractive materials, however. Other potential applications of photorefractive materials include real-time holography, optical filtering, adaptive optics, optical logic, edge enhancement, optical switching and laser applications [3,7-9].

Important characteristics of the photorefractive effect in any given material are the photorefractive sensitivity, dynamic range, photorefractive write and erase times, thermal stability and dark decay times, electric field dependence and laser wavelength needed to induce the effect. These characteristics depend greatly on materials properties such as the existence and concentration of defect states (both for generation of carriers and trapping), energy depth of trapping states, mobility and photosensitivity. The defect states which act as the source of charge carriers must reside at an energy from the corresponding delocalized band which matches existing laser wavelengths. For a given value of the electro-optic coefficient the concentration of trapping states essentially determines the maximum strength of the effect since they determine the maximum size of the internal space-charge field which can be generated. It is important to note, however, that if the concentration of photogenerated carriers during

grating writing is so great that all the trapping states are filled the trapped carriers won't contribute to the space-charge field at all since they are uniformly distributed. The depth of the trapping states is important because it affects the thermal stability of the effect and the drift mobility plays a part in determining the response time during writing and erasure. Lastly, high photosensitivity is generally desirable, so that comparatively little power is required to generate a large number of freed carriers during writing. Also, parameters such as temperature, light intensity and strength of applied electric field (if any) play an important role.

In comparison to other materials BSO and BGO may offer several advantages. The response time of BSO is several orders of magnitude better than for $LiNbO_3$ or $BaTiO_3$. According to Arizmendi [10] the response times are ~ 1, ~ 0.1 and $\sim 10^{-4}$ s for $LiNbO_3$, $BaTiO_3$ and BSO, respectively, with an intensity of 1 W/cm^2. The fast response of BGO and BSO comes at the expense of the maximum value of the change in refractive index, however. Ferroelectrics such as $LiNbO_3$ and $BaTiO_3$ have larger electro-optic coefficients giving larger refractive index changes. Another advantage of BSO is that the energy of the source needed for grating writing is much lower. Often the holographic sensitivity is defined as the energy density needed to obtain a diffraction efficiency of 1% with a fringe contrast of 1 [11]. Using this definition the sensitivity of undoped $LiNbO_3$ is typically 10–100 J/cm^2, for $BaTiO^3$ it is $\sim 10^{-2}$ J/cm^2 and for BSO it is on the order of 10^{-3} J/cm^2.

1.1 Crystal Structure and Growth

Ballman first grew single crystals of BGO and BSO in 1966, using the Czochralski technique [12]. They were grown from melts containing Bi_2O_3 and SiO_2 or GeO_2 mixed in molar proportions of 6:1. Since then it has been found that crystals can be grown with melt compositions which deviate slightly from this 6:1 ratio [13]. Brice

found that $Bi_xSiO_{1.5x+2}$ can be grown with x varying between 11.77 and 12.05. This variation in composition can result in differences in point defect densities and therefore can affect the photorefractive behavior.

BGO, BSO and BTO have the sillenite body-centered cubic structure. Sillen first associated this structure with the γ-phase of Bi_2O_3 [14]. From pyroelectric properties and x-ray diffraction measurements it has been deduced that it belongs to the space-group I23. A detailed study of the atomic positions of Czochralski-grown BGO was performed by Abrahams et al. [15].

The unit cell of BGO is shown in Fig. 1.1. The lattice constant has been reported to be 10.1455 Å by Bernstein [16]. The tetrahedra at the corners and center of the cube are formed by O atoms surrounding the M atom (M = Ge, Si or Ti). The symmetry requires that the four atoms of the tetrahedra lie along the unit cell body diagonals. Each Bi atom is surrounded by 7 O atoms. The arrangement of Bi and the surrounding O atoms is shown in Fig. 1.2. All of the Bi-O distances and O-Bi-O angles are different. The location of the Bi atoms in the unit cell is shown in Fig. 1.3.

1.1.1 Materials Properties

Table 1.1 lists materials properties of the sillenites which are relevant to photorefractive applications. BGO and BSO are optically active and both left-handed and right-handed rotation of the plane of polarization have been observed [17,18]. The optical rotatory power of BGO, BSO and BTO is given in Table 1.1 for several wavelengths. The optical activity makes measurement of material properties such as the electro-optic coefficient problematic and can cause difficulties with certain applications.

BSO and BGO are cubic, but become uniaxial under an applied field. In BSO the electro-optic coefficient has been found to be about $r_{41} = 5 \times 10^{-12}$ m/V [19] and the

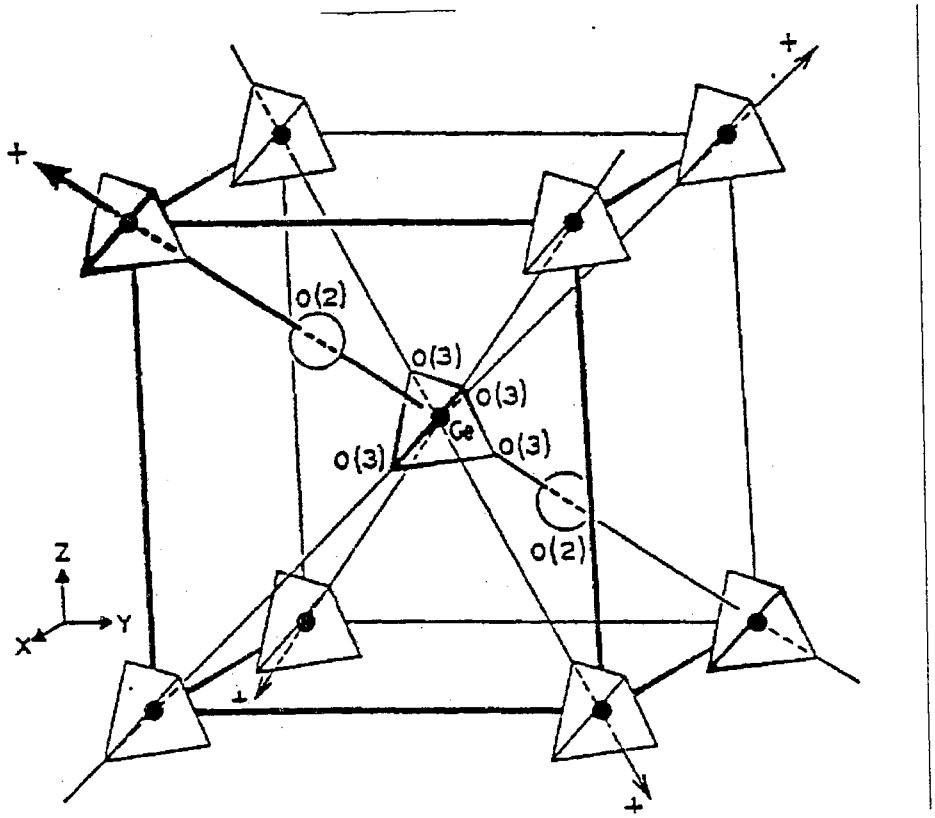

Figure 1.1: The unit cell of $Bi_{12}GeO_{20}$. The O tetrahedra around the Ge atoms are shown (from Abrahams et al.).

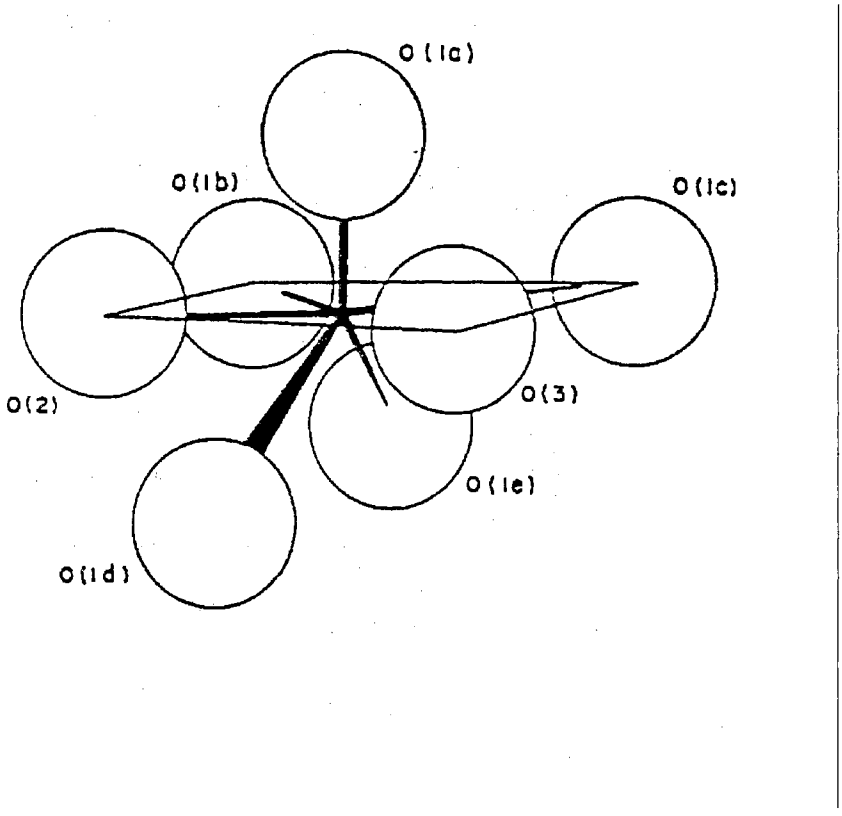

Figure 1.2: Arrangement of O atoms surrounding Bi in the BMO lattice (from Abrahams et al.).

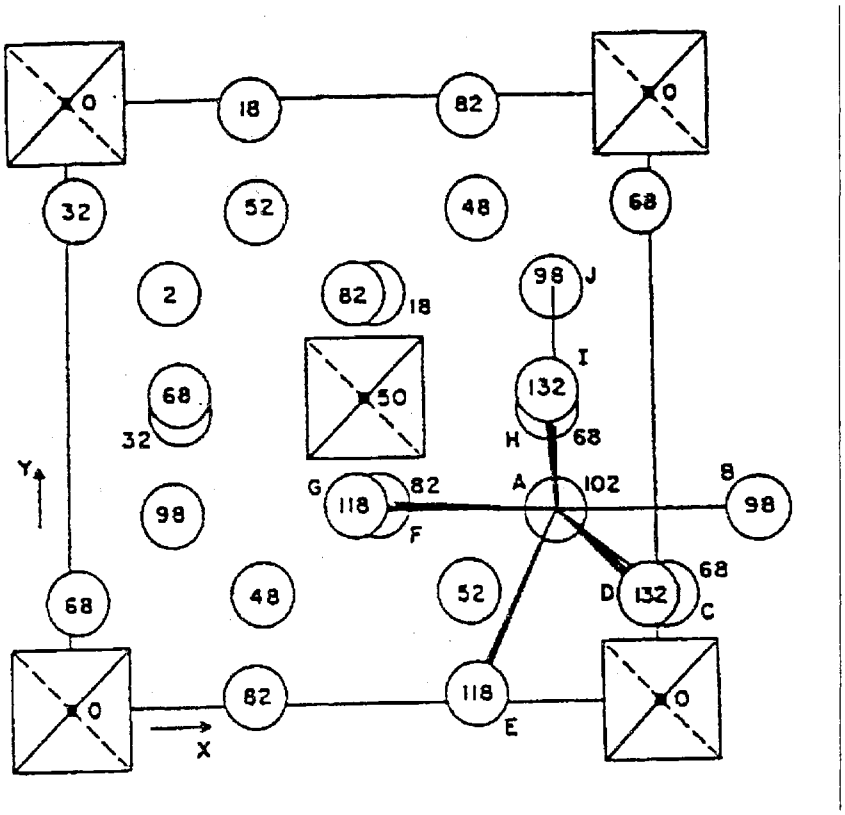

Figure 1.3: Location of Bi atoms (circles) in the unit cell of BGO. The oxygen tetrahedra are indicated (squares) as well. The numbers indicate the z-coordinate (from Abrahams et al.).

half-wave voltage is about 4 to 4.5 kV [11].

The dark resistivity of undoped BGO and BSO has been measured a number of times with widely varying values being obtained [19-21]. Values range from about 5×10^{10} to approximately 10^{15} Ω cm. Also, it has been found that the dark resistivity decreases by several orders of magnitude when dopants such as Al or Ga are added to the melt.

The band-gap of BGO and BSO is about 3.25 eV at room temperature and increases to $\sim$3.40 eV at 80 K. The characteristic yellow coloration of undoped BGO and BSO Czochralski-grown crystals is due to a level (referred to as a "deep donor") situated about 2.7 eV below the conduction band. This level is responsible for a broad absorption shoulder in Czochralski-grown samples, but the shoulder is absent in hydrothermally-grown crystals [22,23]. The absorption level is present in a concentration of $\sim10^{25}$ m^{-3} which rules out the possibility of it being an extrinsic defect due to the purity of the starting materials. The deep donor level is the level out of which electrons are normally excited during grating writing as its depth in the conduction band matches wavelengths which are readily available in lasers and its high concentration makes it a plentiful source for electrons. It has been found by a number of experimenters that doping with Group III elements such as Al or Ga reduces the absorption shoulder [20,24-26]. The extent of the reduction depends on the amount of dopant added to the melt.

BGO and BSO are strongly photoconductive when placed under blue illumination and the photoconductivity in undoped crystals has been assumed to be predominantly n-type, while the dark conductivity is p-type [3,20,24,27]. Doping with Al or Ga in sufficient concentrations causes the photoconductivity to become p-type as well. Unexcited crystals are much less photoconductive in the red and infrared, but excitation with blue light causes additional photoconductivity and absorption bands to appear

at long wavelengths [20,26,28,29].

Czochralski-grown crystals are highly defective materials having many states in the forbidden band. These states can be studied using a variety of techniques including thermally stimulated conductivity (TSC), thermoluminescence (TL), optical absorption and others. Unfortunately, however, TSC, TL and optical absorption don't provide a direct determination of defect type.

1.2 Thesis Project

In order to optimize a material for an application the properties of that material must be understood. Since the materials properties determine the characteristics of the photorefractive effect (write and erase times, thermal stability, dynamic range, etc.) it is necessary to have knowledge of the trapping states before reliable devices can be commercially produced. Additionally, it is desirable to understand the origins of defect states, so that crystals can be grown that have desirable properties which are present with little variability between crystals grown at different times or in different laboratories.

It is the goal of this dissertation to advance the knowledge of the materials parameters of $Bi_{12}GeO_{20}$ and $Bi_{12}SiO_{20}$ which are important to the photorefractive effect and, therefore, to device development. Since the trapping states play a crucial role in the photorefractive response of these materials particular importance will be given to studying the trapping kinetics. Parameters of interest are trap densities, activation energies and frequency factors, drift mobility and the effect of dopants on these parameters. Identification of the dominant traps during hologram writing and erasing is also desired. A variety of experimental techniques were used in this work including thermally stimulated conductivity, thermoluminescence, photoconductivity, optical absorption, dark conductivity, time-of-flight and photorefractive measurements.

Table 1.1: Materials properties of the sillenites (from Arizmendi [10]).

Property	BSO	BGO	BTO	units
Dielectric constant	56	38.7	47	-
Refractive index				
488 nm	2.650	2.650		
514 nm	2.615	2.615		
633 nm	2.530	2.530	2.58	
Rotatory power				mm^{-1}
488 nm	44	45	14	
514 nm	38	38	11	
633 nm	22	22	6	
Optical bandgap				eV
room temperature	3.25	3.25	3.1	
80 K	3.40			
Electro-optic coeff. r_{41}	$3.6 - 5.0 \times 10^{-12}$	3.8×10^{-12}	5.8×10^{-12}	m/V
Lattice constant	10.102	10.145	10.175	Å
Dark Resistivity	7.5×10^{15}	5.3×10^{15}		Ω cm

Chapter 2 presents the results of measurements of steady-state photoconductivity, optical absorption, thermally stimulated conductivity and luminescence, and dark conductivity which were performed on undoped and Ga-doped BGO. These measurements provide a qualitative picture of the defect structure in these materials. Also, the types of defects present in BGO and BSO are discussed.

In Chapter 3 the theory of TSC and TL is presented to provide a basis for discussion of the analysis of the TSC spectra of BGO which is deferred until Chapter 4. Many researchers gloss over the analysis of TSC and TL spectra, but a proper analysis can provide detailed information about the various trapping levels. The TSC analysis allows us to find estimates for trapping parameters such as frequency factors and activation energies.

The results of mobility measurements using the time-of-flight technique are discussed in Chapter 5. It was found that the drift mobility is trap limited over the temperature range from 200 to 300 K and the trap which limits the mobility is seen in the TSC spectra at about 150 K.

The thermal stability of laser-induced gratings and the effect of temperature on grating strength was measured and is discussed in Chapter 6. It was found that the temperature dependencies are consistent with the thermal stability of traps which was determined from the TSC, photoconductivity and optical absorption. The results of simulations of the photorefractive effect will be presented in this chapter as well.

Chapter 2

Trapping of Photocarriers

2.1 Introduction

This chapter presents the results of steady-state photoconductivity, simultaneous thermoluminescence (TL) and thermally stimulated conductivity (TSC), optical absorption and dark conductivity measurements which were performed on undoped, Ga-doped and Al-doped BGO. These measurements are useful in characterizing the defect structure of insulating materials and provide us with a semi-quantitative picture of the carrier kinetics. The TSC and TL measurements, in particular, allow us to obtain an estimate of the number of defect states present as well as their activation energies (for charge carrier trapping) and associated frequency factors. In conjunction with photoconductivity measurements we can estimate trap concentrations as well.

The electrical measurements required that the samples be fitted with electrodes. For most of the measurements gold electrodes were evaporated on to the sample surfaces. The front electrode was made semi-transparent so that the sample could be illuminated through the electrode and the back electrode was made thick. The sample was then mounted on the copper block of an Oxford Instruments dynamic flow cryostat as shown in Fig. 2.1. A thin piece of mica was laid on the copper block to provide electrical insulation and on top of the mica was placed a piece of indium. A thin gold wire was pressed into the surface of the indium and then the sample with

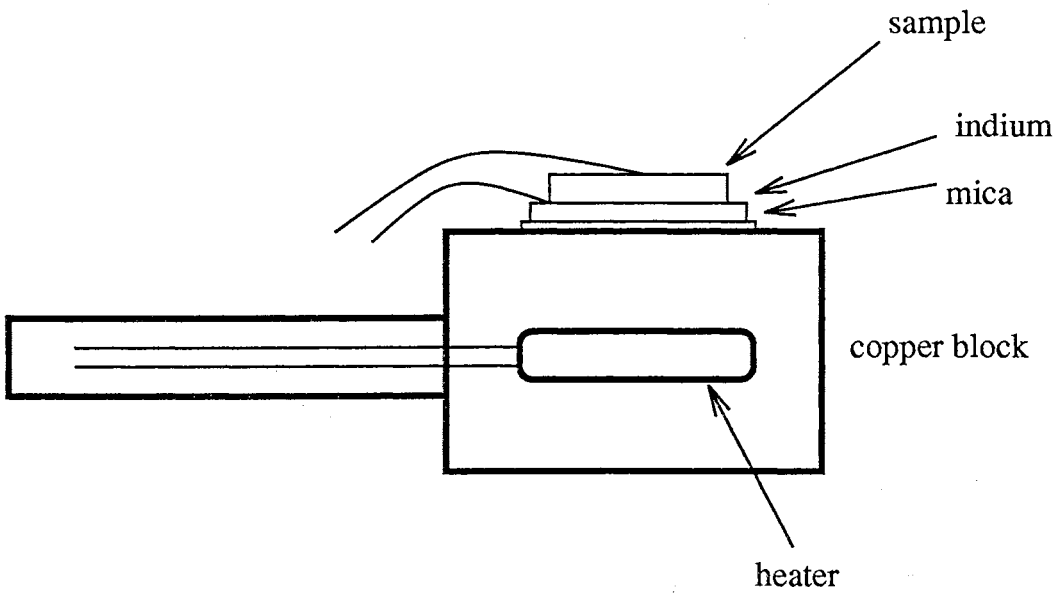

Figure 2.1: Diagram of the sample mount.

gold electrodes was laid on top. Another thin gold wire was used to provide electrical contact to the semi-transparent top electrode and then a delrin cover was placed on top of the whole assembly and screwed in place. Electrical contact to the gold wires was made by soldering them to wires which were fed through the sample holder.

The experimental apparatus used for the TSC, TL, photoconductivity and dark conductivity measurements is shown in Fig. 2.2. The samples were mounted in an Oxford Instruments CF1204 dynamic flow cryostat and cooled with liquid nitrogen. An Oxford ITC4 temperature controller was used to control the temperature and provide a linear heating profile for the TSC and TL measurements. The output of a 100 W Xenon lamp was passed through an Oriel monochromator to select the excitation wavelength. The TL emission was measured using a PMT sensitive in the blue part of the spectrum and a Keithley 617 electrometer with a resolution of 0.1 fA was used to measure the currents. The voltage source of the 617 was used to bias the samples. A PC was used to control the experiments and to store the measured data.

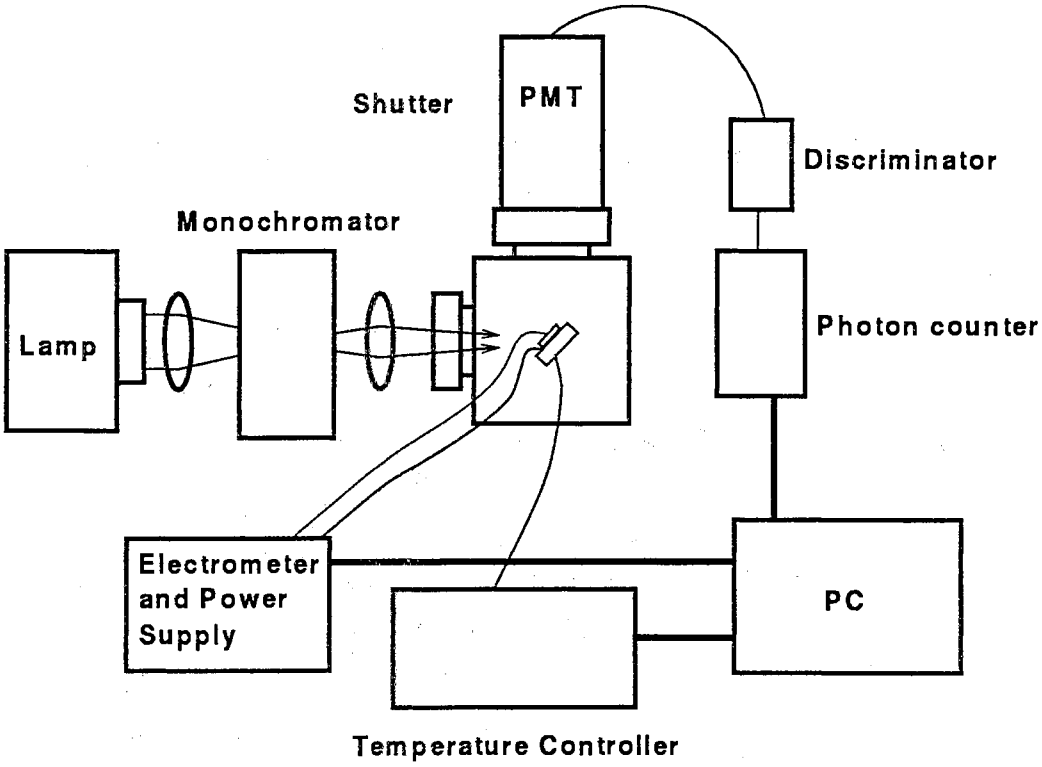

Figure 2.2: Diagram of the experimental setup used for TSC, TL, photoconductivity and dark conductivity measurements.

2.1.1 Optical Absorption

Optical absorption spectra were measured over the wavelength range from 300 nm to 1200 nm, at both 77 K and room temperature, using a CARY 5 UV-Vis-NIR spectrophotometer. The wavelength resolution was 2 nm. Data taken at room temperature for 4 samples, undoped, 2% Ga-doped and 6% Ga-doped BGO and hydrothermal BSO, are shown in Fig. 2.3. A hydrothermal BSO sample was used because hydrothermal BGO was not available at the time the measurements were made. These data are similar to those measured previously [30-33]. The optical absorption spectra for the undoped BGO sample shows a shoulder next to the band edge. The shoulder is a characteristic feature of Czochralski-grown BGO and BSO [20,22,24-26,28,35,36]. The shoulder, which causes the yellow coloration of undoped BGO, is due to a level residing about 2.7 eV below the conduction band edge and is referred to as a "deep donor" in the literature since it donates electrons to the conduction band under appropriate optical excitation. As gallium is added to the melt the strength of the absorption shoulder decreases. Similar behavior is seen when the crystals are doped with aluminum [20,25,26,29]. Aluminum and gallium are believed to act as acceptors and compensate the deep donors causing the absorption shoulder. For high concentrations ($\sim$4–6% in the melt) of gallium or aluminum the shoulder is essentially gone. Fig. 2.3 also shows that the hydrothermal sample exhibits no absorption shoulder making samples grown by this method transparent. This has been observed by others [22] and it is believed that the hydrothermal sample shows the true band edge.

Fig. 2.4 shows the additional absorption in undoped BGO induced by optical excitation at low temperature. Curve 1 shows the absorption spectrum of the unilluminated sample while curve 2 shows the spectrum after illumination with 3.0 eV light for 5 hours at 80 K. The inset shows the difference of the two curves, i.e. the

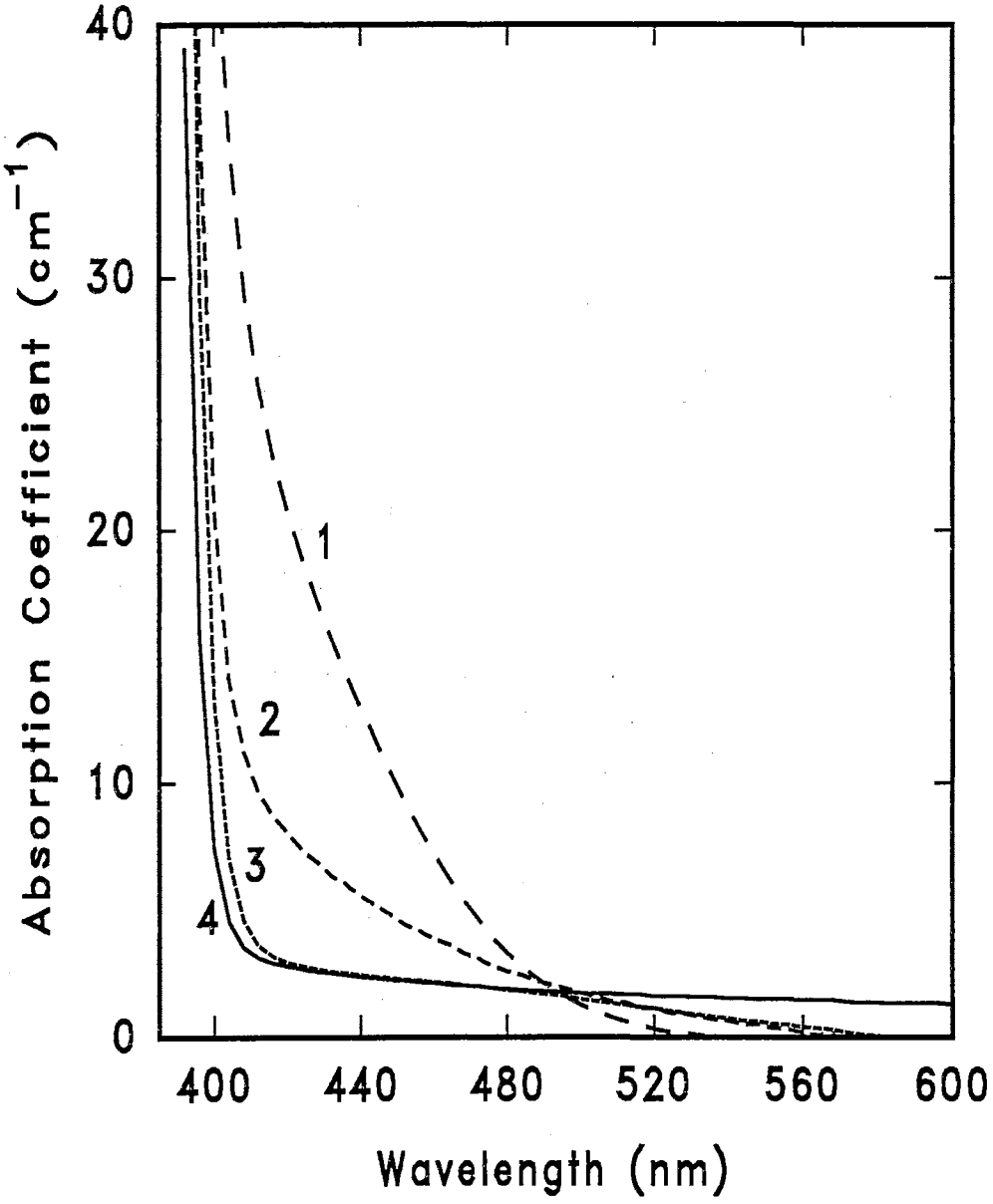

Figure 2.3: Optical absorption spectra at room temperature for (1) undoped BGO, (2) 2% Ga-doped BGO, (3) 6% Ga-doped BGO and (4) hydrothermal BSO.

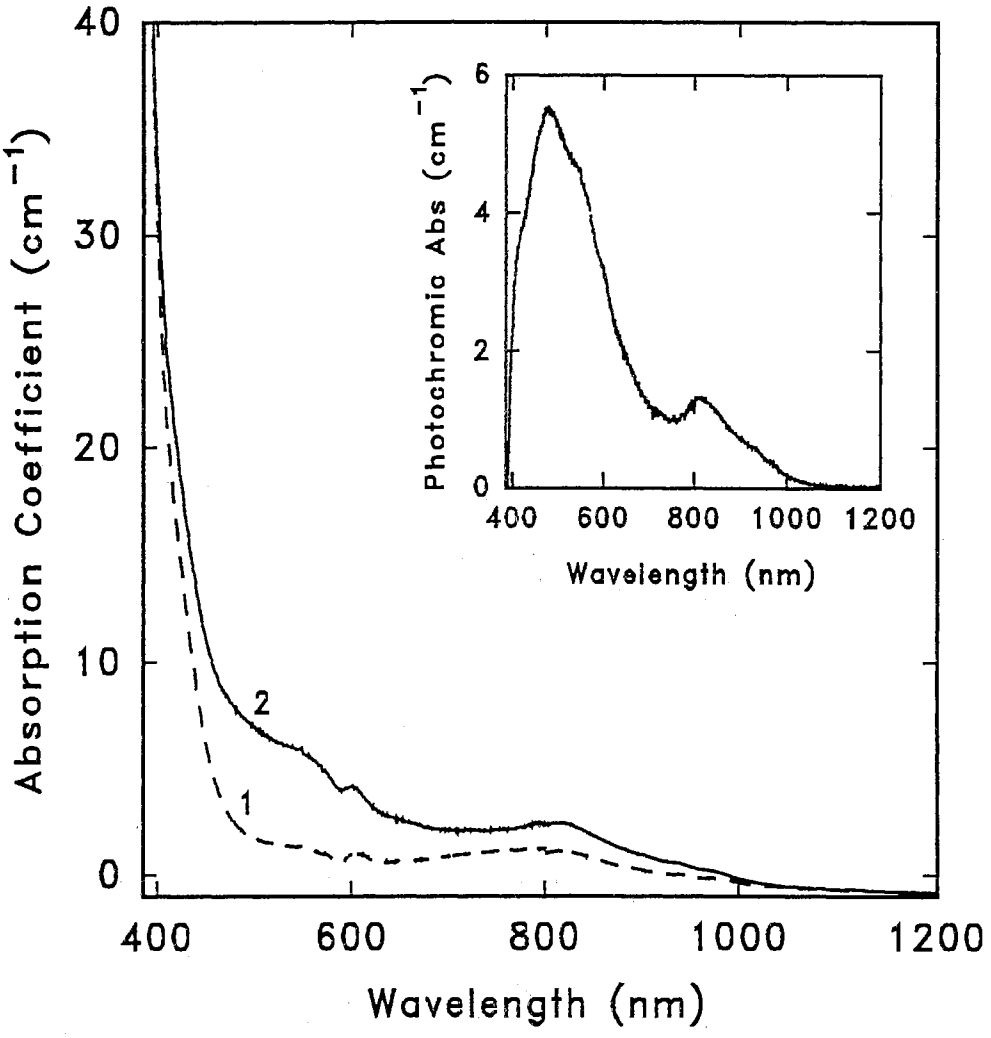

Figure 2.4: Optical absorption of undoped BGO before illumination (curve 1) and after illumination (curve 2) with 3.0 eV light for 5 hours. The inset shows the difference between curve 2 and curve 1.

photochromic absorption produced by the illumination. Similar spectra have been observed before in undoped BGO and BSO and in BGO doped with various elements [26,28,29]. The thermal stability of these photochromic absorption bands is shown in Fig. 2.5. These data were measured by heating to the indicated temperature after the illumination and then cooling back to 80 K where the absorption spectrum was recorded. The figure shows that the decay of the photochromic absorption at both wavelengths is similar. There is a small decay between 80 K and 160 K, but the

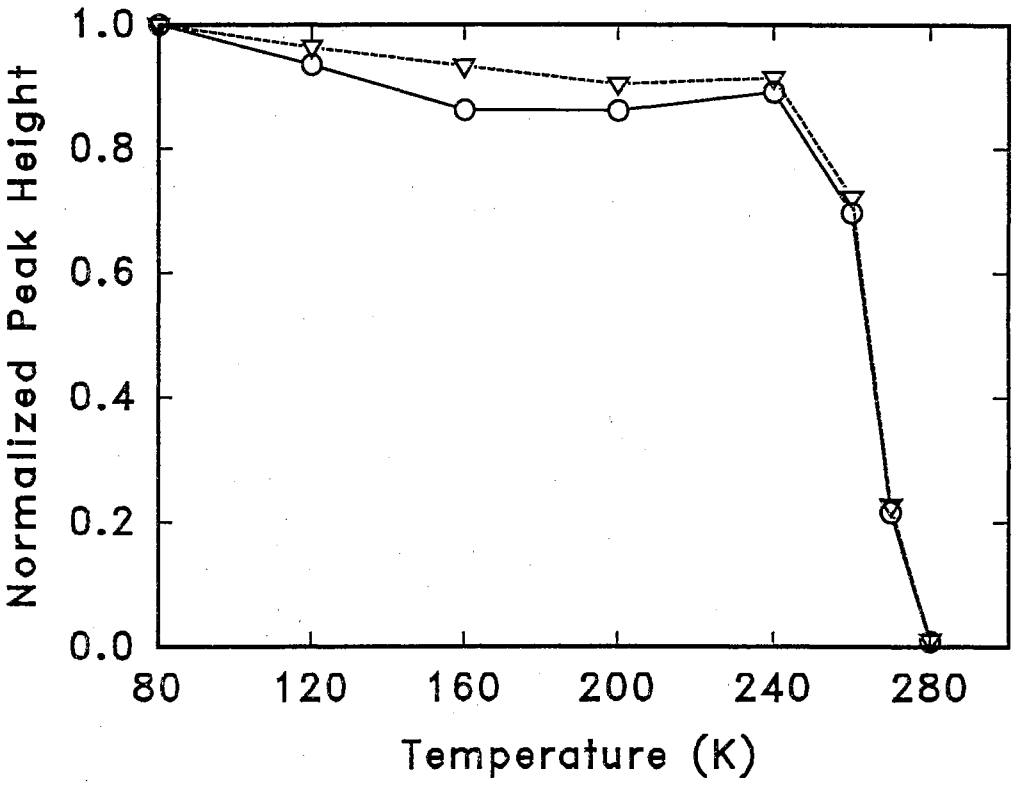

Figure 2.5: Temperature dependence of the photochromic bands at ▽ 801 and at ◯ 488 nm.

majority of the decay occurs between 240 K and 280 K.

2.1.2 Photoconductivity

Photoconductivity spectra were measured using a Xenon lamp filtered by an Oriel monochromator. The experiments were performed at 80 K with a wavelength resolution of 4 nm and a small applied bias of about 10–20 v. Both negative and positive applied biases were used. The monochromator was scanned from 1000 nm to 300 nm in 4 nm steps and a 25 s pause was used at each wavelength to allow the current to settle. After this delay 5 current readings were taken over a 10 s interval and averaged to obtain the recorded value. After scanning from 1000 nm to 300 nm the monochromator was scanned back from 300 nm to 1000 nm as a second photoconductivity spectrum was recorded.

Fig. 2.6(a) shows the photoconductivity spectra for undoped BGO and Fig. 2.6(b) shows equivalent spectra for 2% Ga-doped BGO. In (a) the curves labelled 1 and 3 were taken with an applied bias of +10 v (illuminated electrode positive) while curves 2 and 4 were taken with applied biases of -10 v. In (b) the situation is the same except that 12 v biases were used. Curves 1 and 2 were taken by scanning from long wavelength to short wavelength and curves 3 and 4 were taken by scanning immediately back from short to long wavelength. In the initial scan the current levels are very small until a wavelength matching the deep donor level is reached at $\sim$460 nm. The current level reaches a maximum at $\sim$410 nm in undoped BGO and at $\sim$385 nm for the 2% Ga-doped sample. The current drops for higher energies due to the very strong absorption of the band-edge light near the surface of the sample. When scanning the monochromator from short to long wavelength the currents are larger for all wavelengths, but is especially noticeable at longer wavelengths in the visible and IR. Our interpretation of this is that the initial scan, from long to short

wavelength, excites electrons from the deep donor to the conduction band which are then trapped in states closer to the conduction band edge, so that during the scan from short to long wavelength the lower energy light excites carriers from these trapping states. The data indicate a continuous distribution of states corresponding to wavelengths matching the deep donor level (~2.7 eV) up to 1000 nm (1.2 eV).

For the scans done from long to short wavelength the data for both samples show larger currents for the negative applied bias, i.e. with the front face at a lower potential than the back face, so electrons generated at the front surface by the incident light will be pushed through the bulk of the sample. The larger currents for the negative biases support the belief that the photoconductivity is predominantly n-type [24]. The difference is smaller for the scans done from short to long wavelength because the carriers are generated throughout the bulk of the sample since light far from the band edge is energetic enough to excite carriers out of the traps to the delocalized bands.

Fig. 2.7 shows the temperature dependence of the photoconductivity in undoped and 2% Ga-doped BGO at three wavelengths. The wavelengths were chosen to correspond with the photoconductivity peak near the band edge, the peak just above 600 nm and in the IR at 904 nm. This experiment was performed by heating a sample which had been preilluminated to produce additional photoconductivity bands, like those shown in curves 3 and 4 in Fig. 2.6, to the temperature indicated and then cooling back to 80 K where the photoconductivity spectrum was recorded. Both samples show similar behavior. There is an initial annealing stage from 80 K to ~160 K and a final anneal begins at about 260 K. The 260 K decay agrees well with the temperature dependence of the photochromic absorption as shown by Fig. 2.5.

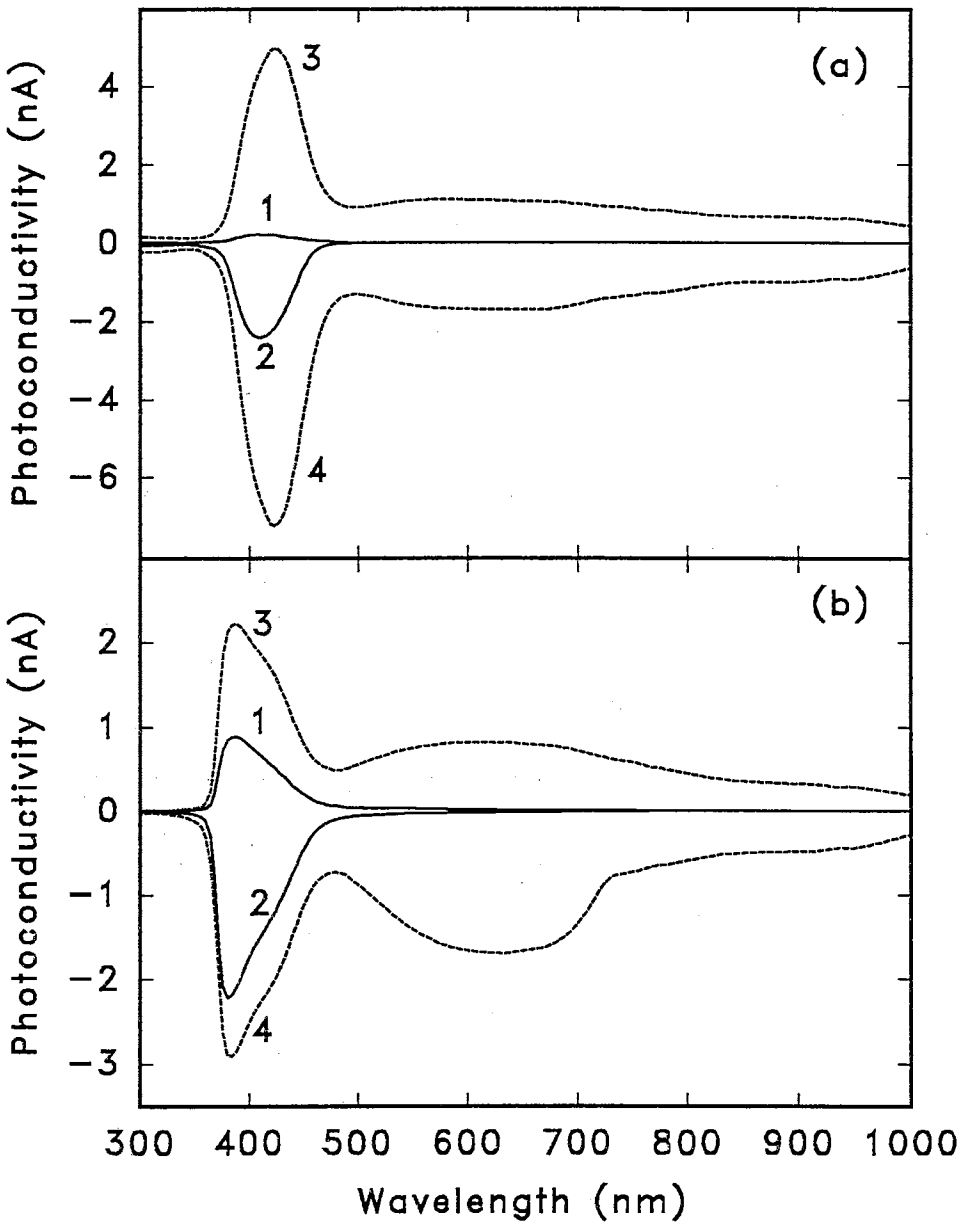

Figure 2.6: Photoconductivity spectra for (a) undoped BGO and (b) 2% Ga-doped BGO. Curves 1 and 3 in (a) were measured with a bias of +10 v and curves 2 and 4 in (a) were measured with an applied bias of -10 v. In (b) curves 1 and 3 were measured with applied biases of +12 v and curves 2 and 4 were measured with -12 v biases. Curves 1 and 2 in both (a) and (b) were scanned from long to short wavelength and curves 3 and 4 were scanned from short to long wavelength.

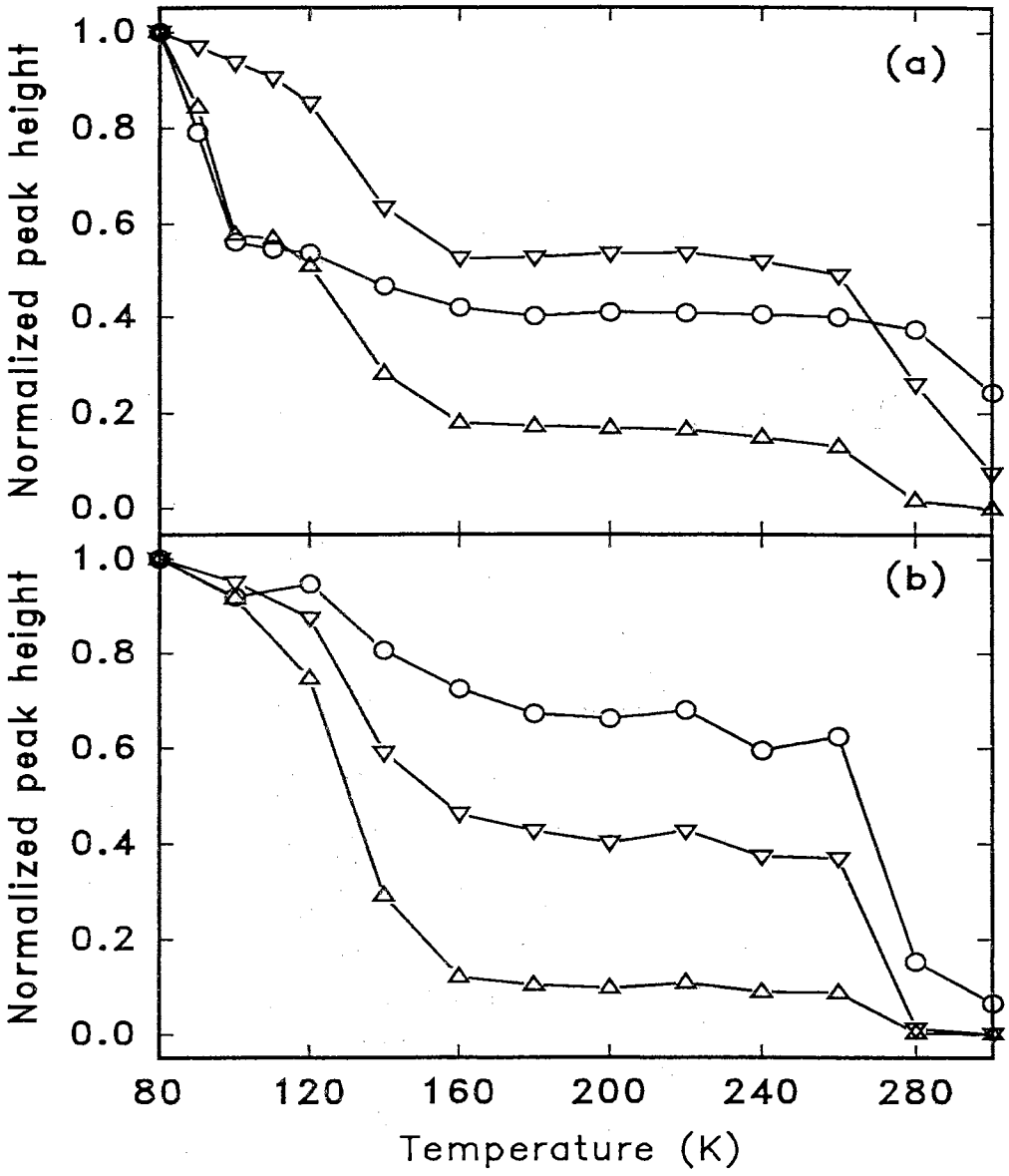

Figure 2.7: Temperature dependence of the photoconductivity signals seen in (a) 2% Ga-doped BGO and (b) undoped BGO. In (a) the photoconductivity signal is taken as the peak heights at ○382, ▽600 and △904 nm. In (b) the wavelengths are ○418 ▽ 604 and △904 nm.

2.1.3 Dark conductivity

The dark conductivity was measured by heating the as-received samples in the dark with a small applied bias. Fig. 2.8(a) shows the results of dark conductivity measurements performed on undoped, 2%, 4% and 6% Ga-doped BGO. The data in the figure show that the addition of gallium increases the conductivity. The conductivity of the 2% Ga-doped sample was similar to that of the undoped crystal, but the conductivity increases sharply with increasing Ga concentration for the higher doping levels. We determined the activation energies associated with the dark conductivity from the slope of Arrhenius plots like that shown in Fig. 2.8(b). The activation energies obtained for the different samples are listed in Table 2.1. These values are similar to those obtained by others [20].

Table 2.1: Activation energies from dark conductivity measurements.

Sample	Energy (eV)
Undoped BGO	1.41
2% Ga-doped BGO	0.86
3% Ga-doped BGO	0.82
4% Ga-doped BGO	0.86
6% Ga-doped BGO	0.54

We attempted to determine the sign of the charge carriers by performing a Seebeck measurement. By heating the samples from one side a temperature gradient can be created across the sample and free carriers in the warm region will diffuse to the cooler region. Monitoring the polarity of the induced voltage identifies the carriers as either electrons or holes. In all cases we found that the free carriers were holes. Others have identified the dark conductivity as p-type as well [19,20]. This is in contrast to the

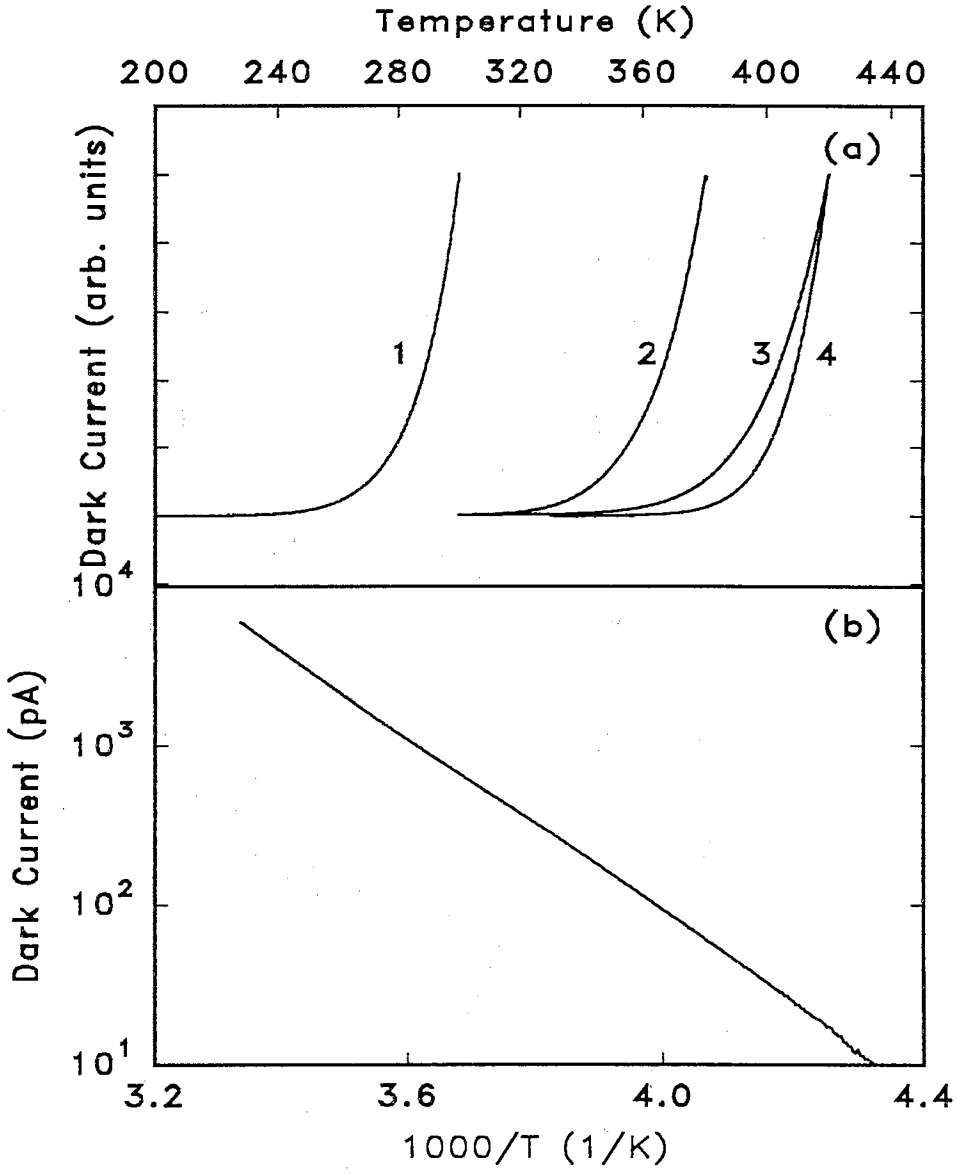

Figure 2.8: (a) Dark conductivity vs. temperature for (1) 6% Ga-doped BGO, (2) 4% Ga-doped BGO, (3) 2% Ga-doped BGO and (4) undoped BGO. (b) An Arrhenius plot for the 6% Ga-doped sample.

belief that the photoconductivity is n-type. Our interpretation of this is that warming the samples excites holes out of empty deep donor levels to the valence band. As the gallium concentration is increased the Fermi Level moves down in the band-gap and the occupation of the deep donors decreases so that empty donor levels exist closer to the valence band resulting in lower activation energies for the dark conductivity. Our data indicate that the donor level consists of at least 3 states lying ~1.41, ~0.86 and ~0.54 eV from the valence band.

2.1.4 TSC and TL

Fig. 2.9(a) shows the TSC signals measured in undoped BGO using a +10 v bias and two different illumination wavelengths. These spectra are similar to those measured by other authors [32,34,37,38]. Curve 1 was measured after illumination at 412 nm (3 eV) and curve 2 was obtained after illuminating at 476 nm (2.6 eV). The illumination times were normalized so that the same number of photons struck the surface of the sample in each experiment. The spectra obtained with a bias of -10 v were essentially identical. Both of the illumination wavelengths are sub-band-gap, but do excite electrons out of the deep donor level into the conduction band. Therefore, we believe that the peaks in the spectrum are due to electron traps. Fig. 2.9(b) shows the TL signal measured simultaneously with the TSC after the 412 nm illumination. For the 476 nm illumination no TL was measured indicating that the empty deep donor states do not act as radiative recombination centers during TL.

Fig. 2.10 shows the TSC and TL measured on undoped BGO after illumination with light of wavelength of (a) 368 nm and (b) 350 nm. Both of these wavelengths are sufficiently energetic to cause band-to-band transitions. The TSC signals observed after illumination at these wavelengths are much weaker than was seen after illumination with sub-band-gap light. This is most likely due to the very strong absorption of

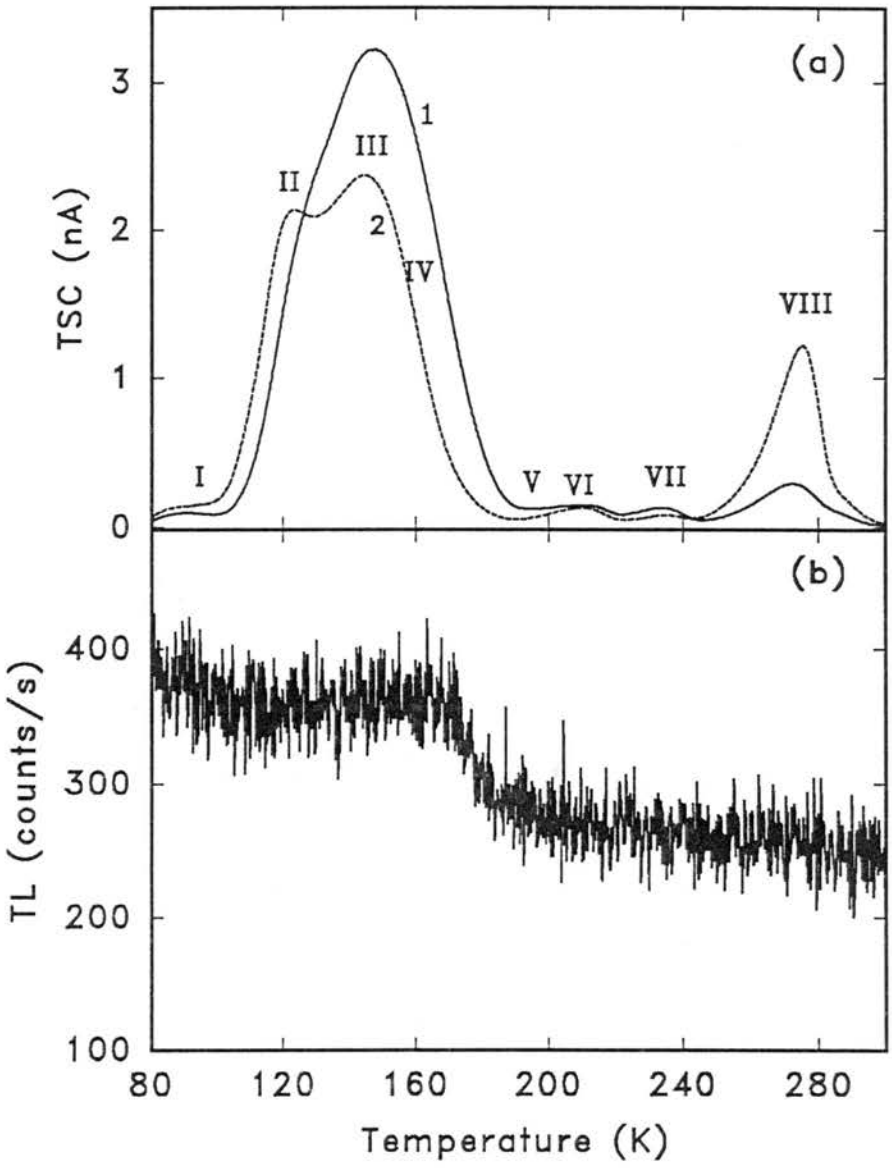

Figure 2.9: (a) TSC and (b) TL from undoped BGO. Curve 1 is after illumination at 412 nm for 7700 s and curve 2 is after illumination at 476 nm for 3600 s. Both illuminations were performed at 80 K and a bias of +10 v was applied during illumination and heating. No TL was observed after 476 nm illumination

the 368 and 350 nm light which results in much less filling of the bulk traps. However, the TL is much stronger in this case. This is understandable since TL requires that free holes are generated to fill radiative recombination centers. Using sub-band-gap light results in the filling of electron traps, but not in the filling of the radiative recombination centers by holes, so the TL signal is very weak.

It can be seen from any of the TSC spectra that there are many overlapping peaks indicating that there are a large number of trapping states. The dominant TSC peak is the peak centered at ~150 K. The TSC measured after illumination at 476 nm indicates that this peak is a composite peak made up of more than one component. There are also many smaller overlapping peaks at higher temperatures. Table 2.2 gives the approximate positions of the peaks which are present in the TSC and TL spectra. The labels on the peaks in the figures correspond to the labels in the table.

The TSC peaks below 180 K also have associated with them TL signals. Fig. 2.10(b) shows that there are at least 3 TL peaks over the range from 80 K to 180 K. Above 180 K no TL is observed. This is most easily explained by assuming that all of the radiative recombination centers have been used up by this temperature.

Since we think we are exciting only electrons with sub-band-gap light a comparison of the TSC spectra in Fig. 2.9 and Fig. 2.10 can identify which peaks are due to electron traps and which are due to hole traps. This identification is shown in Table 2.2.

We tried to measure the emission spectrum of the TL, but found that the signal was too weak to detect after being filtered by a spectrometer. However, using interference filters we were able to obtain rough estimates of the TL emission wavelengths. These wavelengths are given in Table 2.2.

Fig. 2.11 shows the TSC and TL measured in 2% Ga-doped BGO. Again, illuminations were performed at 80 K with wavelengths of 412 and 476 nm and the applied

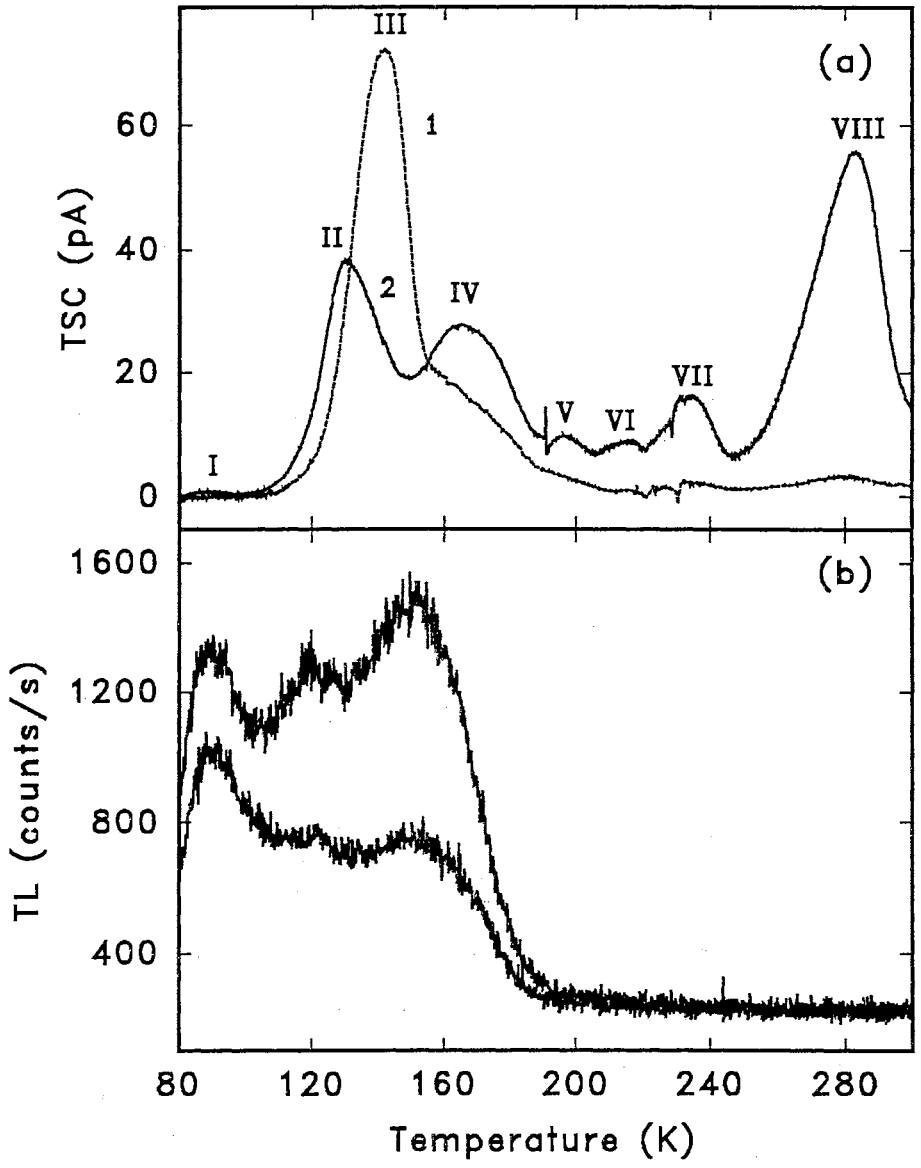

Figure 2.10: (a) TSC and (b) TL from undoped BGO. Curve 1 is after illumination at 368 nm for 19400 s and curve 2 is after illumination at 350 nm for 24800 s. Both illuminations were performed at 80 K and a bias of +10 v was applied during illumination and heating.

Table 2.2: TSC and TL peak parameters for undoped BGO.

TSC peak	Temperature (K)	TL?	TL emission (nm)	e/h
Ia	85	Y	?	?
I	90	Y	400	e
II	120	Y	590	e
III	150	Y	500	e
IV	~170	Y	500	h
V	193	N		h
VI	210	N		e
VII	230	N		e
VIII	275	N		e

bias was +12 v. Fig. 2.12 shows the TSC and TL signals after illumination with 350 and 368 nm light. Qualitatively, the spectra are very similar to those observed in undoped BGO, but the peaks are smaller. This may be due to a lower concentration of trapping states or it may be due to the presence of fewer occupied donor states during the illumination cycle resulting in fewer electrons excited into the conduction band and fewer filled traps. The dominant peak in the TSC spectra is less broad than for the undoped sample and is located at a slightly lower temperature of ~120 K. Again, there are many smaller overlapping peaks at higher temperature. The TSC signal is much stronger for the 412 nm excitation than for the 350 and 368 nm illuminations, but the 476 nm illumination produced much weaker TSC, in contrast to what was observed in undoped BGO. We believe that the introduction of gallium produced acceptors which compensated some of the donor levels from which we excite electrons with 412 and 476 nm illumination in undoped BGO. This results in a lower

Fermi Level and, consequently, the filling of the donor levels by electrons is decreased enough that the 476 nm light is not sufficiently energetic to excite electrons to the conduction band. As in undoped BGO, the TL is very weak or non-existent after illumination with sub-band-gap light, but is present after band-edge excitation as shown by Fig. 2.12(b).

Fig. 2.13 shows the TSC spectrum of Fe-doped BGO. The TSC of the Fe-doped sample is very similar to that of the undoped specimen. Again, there is a broad peak at about 150 K with a series of smaller peaks at higher temperatures.

We tried to measure TSC spectra in samples doped with greater than 2% Ga in the melt, but found that the electrodes were blocking. This is probably due to the decrease in the Fermi Level. We did, however, succeed in measuring TL. TL spectra for several samples with varying concentrations of Ga are shown in Fig. 2.14. No systematic variations in the TL signal were seen as a function of gallium concentration.

2.2 Discussion

2.2.1 Optical Absorption

The defect responsible for the absorption shoulder (the deep donor level) in the undoped crystals has been the subject of much debate. It is widely accepted that the defect must be a native defect rather than an impurity because the absorption band is nearly identical in crystals grown in different labs and the estimated concentration of the absorption centers is so high that the purity of the starting materials forbids it being an impurity. It was argued by Oberschmid [25] that since the absorption shoulder is very similar in BGO and BSO, differing only in the relative strength of the band, but not the shape, that it is most likely due to the same defect in both

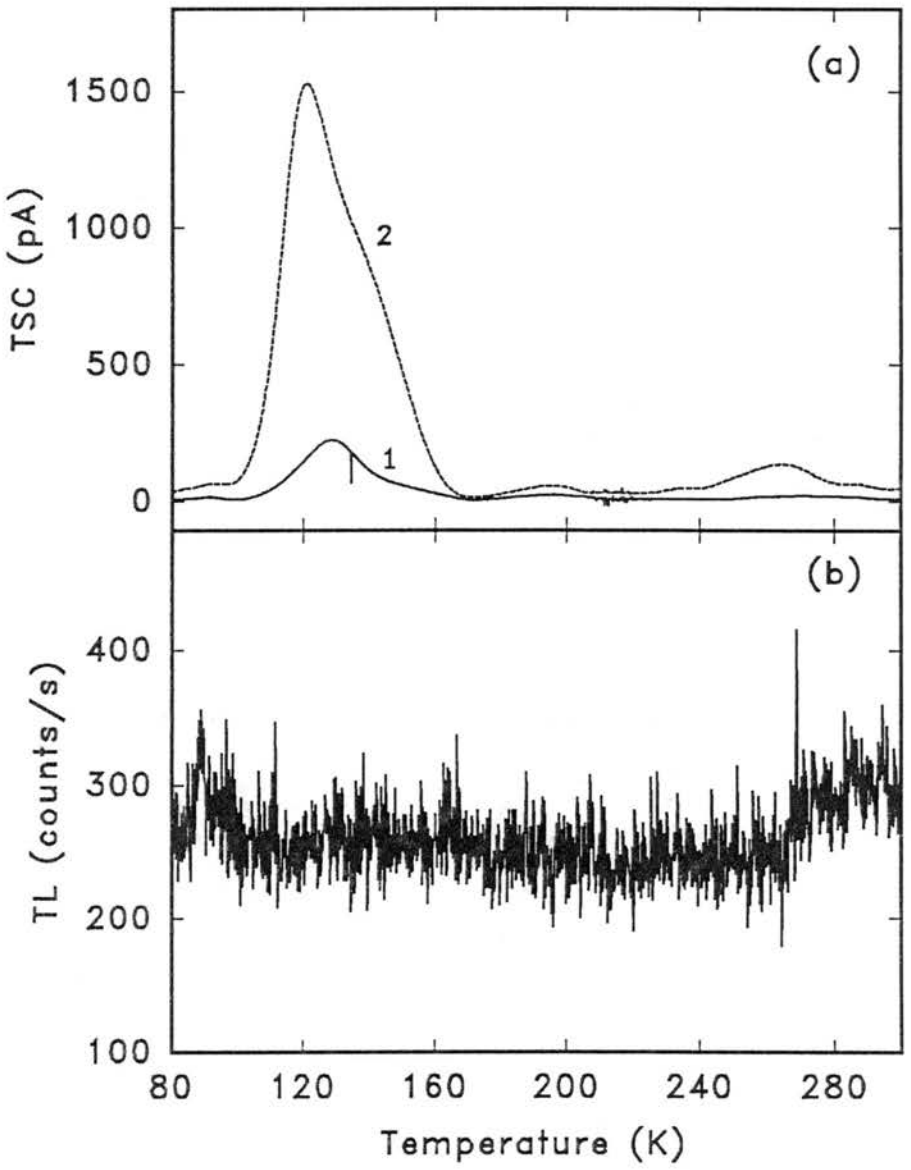

Figure 2.11: (a) TSC and (b) TL from 2% Ga-doped BGO. Curve 1 is after illumination at 476 nm for 3600 s and curve 2 is after illumination at 412 nm for 7700 s. The TL is shown for the 412 nm illumination; 476 nm gave no TL signal. Both illuminations were performed at 80 K and a bias of +10 v was applied during illumination and heating.

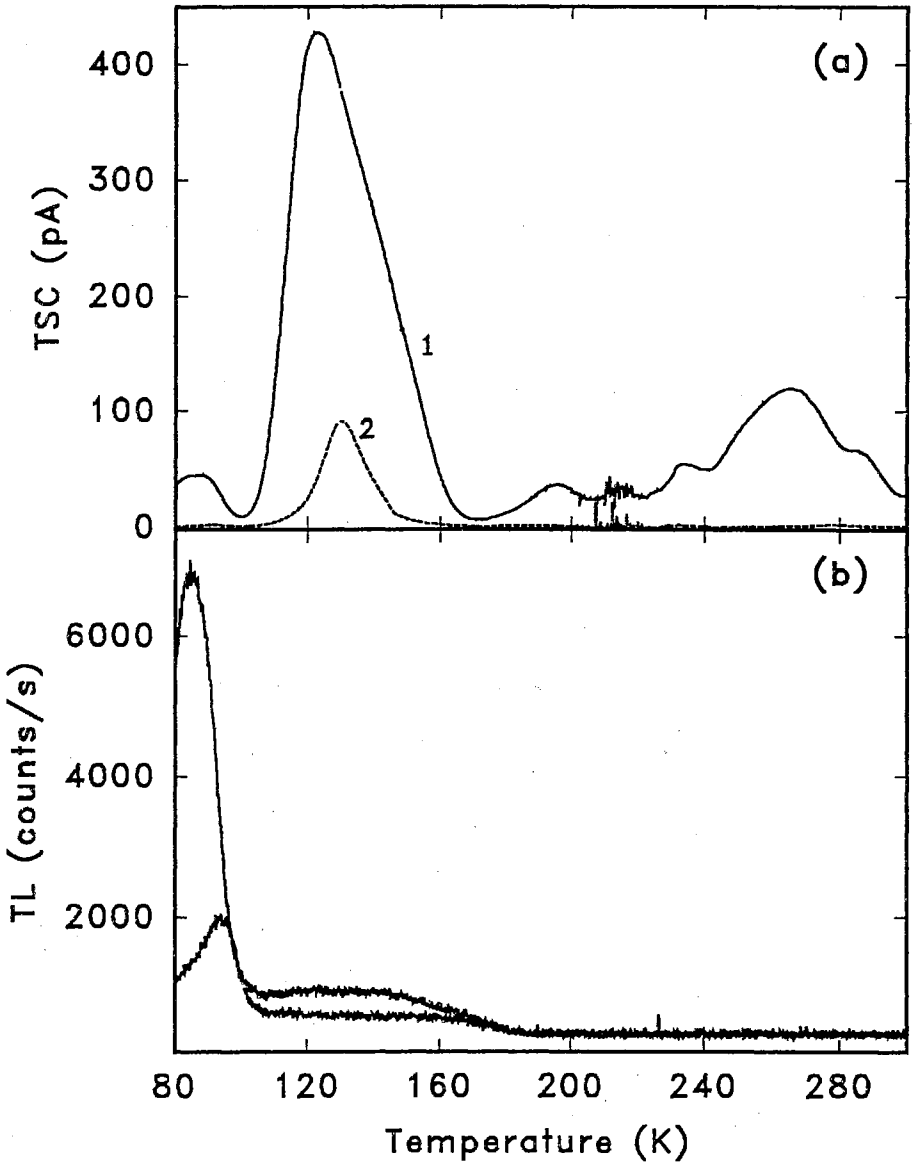

Figure 2.12: (a) TSC and (b) TL from 2% Ga-doped BGO. Curve 1 is after illumination at 368 nm for 19400 s and curve 2 is after illumination at 350 nm for 24800 s. Both illuminations were performed at 80 K and a bias of +12 v was applied during illumination and heating.

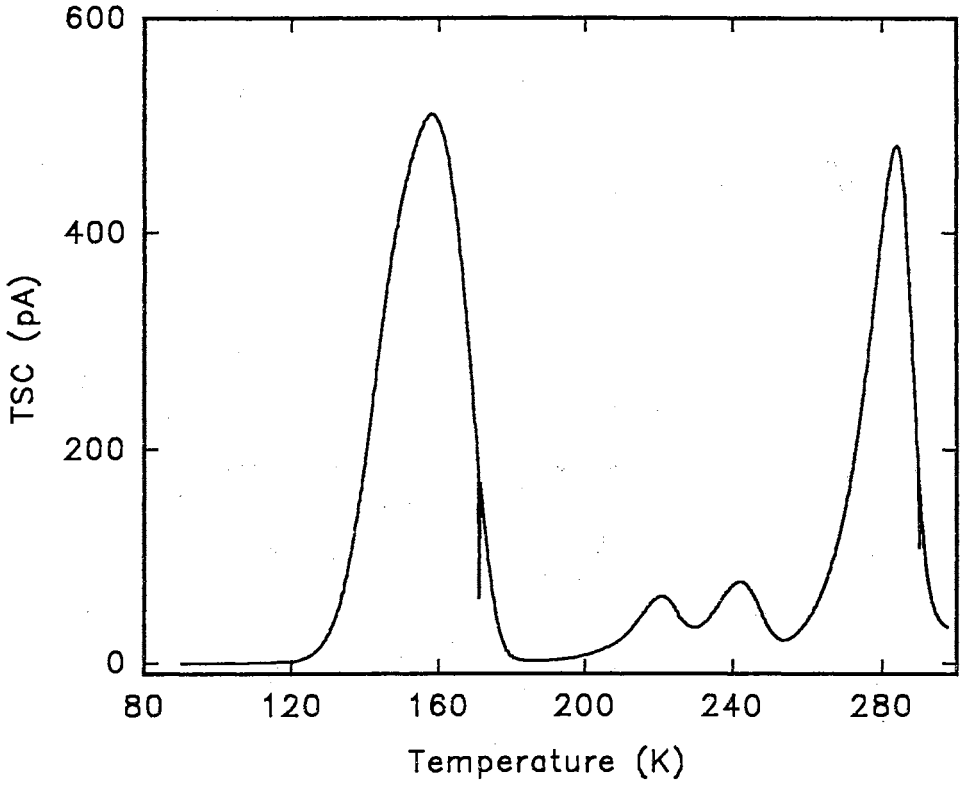

Figure 2.13: TSC measured in 0.3% Fe-doped BGO after a 5 minute white light illumination. The applied bias was -10 v.

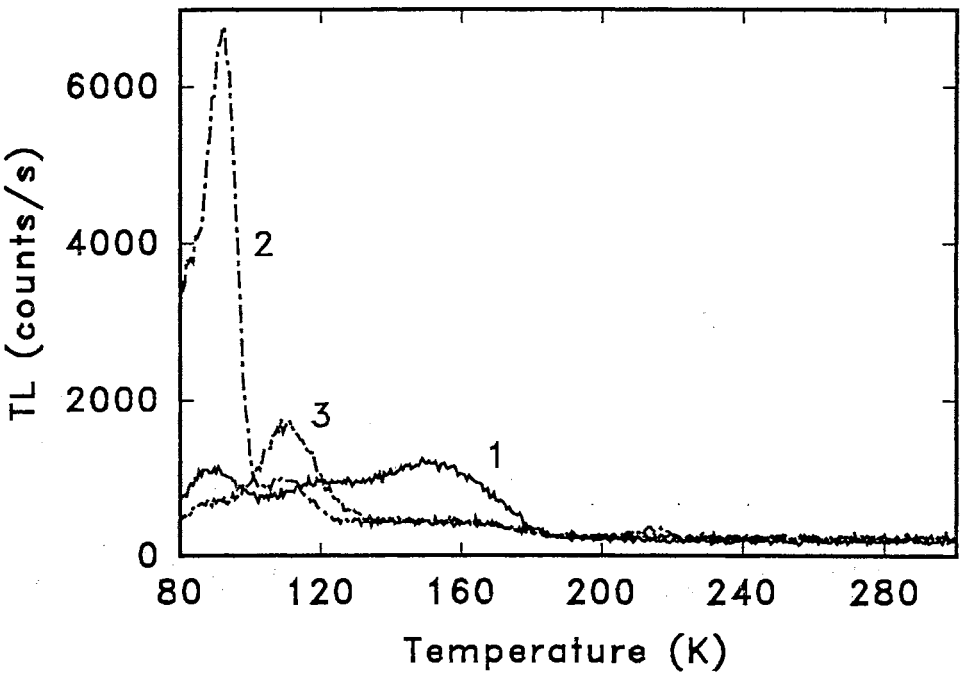

Figure 2.14: TL measured after 368 nm illumination for 19400 s at 80 K in (1) undoped BGO, (2) 3% Ga-doped BGO and (3) 6% Ga-doped BGO.

materials. This requirement is met by assuming that the center is associated with the M site (M = Si,Ge) in the oxygen tetrahedron, either a vacancy or occupation by an incorrect atom. This first possibility was suggested by Hou et al. [24]. Based on thermodynamic considerations Oberschmid, however, argued that a more likely candidate is anti-site bismuth, Bi_M. Experimental support for the Bi_M center as the origin of the absorption shoulder was gained from the results of optically detected magnetic resonance (ODMR) measurements performed in conjunction with measurements of the magnetic circular dichroism of absorption (MCD) [39]. A description of the technique is given in reference [40]. These techniques make it possible to measure the MCD spectrum for a specific defect. Reyher et al. determined that all $Bi_{12}MO_{20}$ crystals share a similar MCD spectrum which is related to an intrinsic defect rather than to an impurity. By performing ODMR measurements it was determined that the MCD spectrum was caused by the Bi_M center.

There are two possible mechanisms for maintaining charge neutrality. One can either assume equal amounts of Bi^{3+} and Bi^{5+} or assume that the defect is Bi^{3+} with an associated hole, h^+, trapped in the oxygen tetrahedron. This last mechanism was thought most likely by Oberschmid, due in part to the results of ultrasonic attenuation measurements. Ultrasonic attenuation measurements performed on BSO [84] showed that there is an ultrasonic attenuation center with tetrahedral symmetry and an activation energy of 0.28 meV for BSO and 0.42 meV for BGO. These values are reasonable for holes jumping between different oxygens in the tetrahedron.

The bleaching of the crystal by doping with Al or Ga can be explained by assuming that at least some of the Al or Ga atoms occupy M sites. On these sites they would act like electron acceptors. The holes are captured by the $Bi^{3+} + h^+$ centers changing them to Bi^{5+}. This explains the transition from undoped to heavily doped behavior as seen in the optical absorption. The absorption data show a gradual decrease of the shoulder with increasing gallium doping as the anti-site Bi is converted to Bi^{5+}. This is consistent, also, with the values for the activation energies obtained from the dark conductivity measurements. From the dark conductivity we found that as the Ga content increases the activation energy for the dark conductivity decreases. We believe that the dark currents are caused by thermal excitation of holes from empty donor states to the valence band. As the Ga content is increased the Fermi Level decreases and fewer donor levels are filled, so empty donor states are closer to the valence band resulting in a lower value for the thermal activation energy.

A detailed study of the photochromic absorption bands was reported in references [26], [28] and [29]. In the work of Martin, Foldvari and Hunt [26] several photochromic bands were found in undoped, Fe-doped and Al-doped BGO. The photochromic bands in undoped and Fe-doped BGO are centered at 1.5, 2.2, 2.7 and 3.1 eV. The presence of Fe appears to make the photochromic bands weaker. It was found, also, that Fe

decreases the strength of gratings written in BGO [41]. The data in Fig. 2.4 appear to show the bands at 1.5, 2.2 and 2.7 eV, but the 3.1 eV band is less certain. This was noted by Martin et al. as well, since the strong absorption in this region makes the difference between the two curves more uncertain. The 1.5 and 2.2 eV bands are smaller in Fe-doped BGO than in undoped BGO, but the ratios of their heights are the same in both materials. This prompted the authors to suggest that they are related to the same center. They found that both the 1.5 and 2.2 eV bands bleach much more efficiently when exposed to green light at 2.28 eV than when exposed to 1.51 eV light. This suggests that the 1.5 eV band is due to an internal transition and the 2.28 eV band involves an excitation to the delocalized band. The major anneal stage of the bands in undoped BGO occurs above 200 K, but the infrared bands show a partial anneal stage at ~120 K [26]. The bands in the Fe-doped samples anneal at lower temperature, between about 120 K and 200 K agreeing with the recovery of the Fe^{3+} ESR spectrum after UV illumination as reported by Jani and Halliburton [46].

The role of iron is not entirely clear. No new bands which can be attributed to iron are present in the absorption spectra, but iron does weaken the bands and introduces a lower temperature anneal stage. In addition, several groups have measured ESR signals of $Bi_{12}SiO_{20}$ and $Bi_{12}GeO_{20}$ and have found a signal corresponding to Fe^{3+} on a tetrahedral site [42-45]. The only site of tetrahedral symmetry in BSO (BGO) is the Si (Ge) site. Since the recovery of the Fe^{3+} ESR signal occurs over the same temperature range as the annealing of absorption bands in Fe-doped material Jani and Halliburton [46] attributed the absorption center to Fe^{3+}.

In Al-doped BGO the photochromic absorption spectrum consists of a broad visible band centered at ~2.45 eV and infrared bands at about 1.0 and 1.38 eV. The spectrum for Ga-doped BGO is similar except that the 1.0 eV band appears at ~1.1 eV [26,29]. In both Al- and Ga-doped material illumination with either infrared or visible

light bleaches the bands. The decay of the photochromic bands in Al-doped and Ga-doped BGO as reported by Martin et al. are similar to the decay in undoped samples in that the decay occurs in 2 steps. The infrared bands and a large portion of the visible bands decay between 80 and 120 K in Al-doped BGO and between 100 and 120 K in Ga-doped BGO. The remaining visible bands anneal at higher temperature and are gone by about 230 K. Fig. 2.7 shows that the thermal decay of the additional photoconductivity induced by illumination is similar, although the decay stages occur at slightly higher temperatures.

Martin et al. [26] suggest that the origin of the broad visible band may be similar to a center seen in quartz which consists of a hole trapped at the Al and has been denoted $[AlO_4]^0$ [47]. In quartz this center has been shown to be the origin of a broad absorption band at 2.5 eV which is very close to the broad 2.45 eV photochromic band seen in Al-doped BGO and BSO. Under band-edge illumination the electron is excited to the conduction band leaving a hole behind at the Al. The broad absorption band in this energy region in Ga-doped BGO could have a similar origin.

2.2.2 TSC and TL

The TSC and TL spectra show many peaks indicating that there are many defect states in the forbidden band. Unfortunately, identification of the defects responsible for the TSC and TL spectra is difficult, but comparison with the work of others may be useful. Petre et al. [30] studied trapping levels using TSC with and without applied biases and obtained spectra similar to those presented here. The authors suggest that since the TSC spectra of BGO and BSO are very similar many of the peaks likely have a common origin in both materials. Defects related to Bi, rather than to Ge or Si, meet this requirement.

Takamori performed a detailed analysis of TSC signals in $Bi_{12}GeO_{20}$ and $Bi_{12}SiO_{20}$

and identified three TSC peaks as being due to holes [37]. A double excitation technique where TSC spectra were recorded after UV illuminations at 80 K with an additional UV illumination at 200 K was used in this determination. All three peaks identified as being due to holes are at temperatures between 200 and 300 K, however, so they don't agree with our identification of peaks IV and V in Figs. 2.9 and 2.10 as being due to holes. One of the peaks Takamori assigned as a hole peak appears to be the same as our TSC peak at ~280 K. Unfortunately TSC experiments don't provide an unambiguous determination of carrier sign.

Some similarities between TSC spectra found in different samples can be seen. The peaks labelled II, III and VIII here have been reported by many different groups [22,30-34,37,38]. This may indicate that these peaks are due to an intrinsic defect or possibly to iron which is present as an impurity in all BGO and BSO crystals. There tends to be more variation in the other peaks which appear between peaks III and VIII in temperature, so they may be due to uncontrolled impurities. The largest peaks in the spectra are almost always these common peaks II, III and VIII, however. It may be that all of the smaller peaks are present in all the different samples, but in varying sizes, so that if a nearby peak is large its smaller neighbor is not visible.

There is a lot of variation in the details of TL in BGO and BSO as well. Lauer measured TSC and TL in undoped BGO and found that all TL peaks had the same emission [34]. We found that this is not the case in our samples, however, as shown in Table 2.2. In addition, we found that there were no systematic variations in the TL spectra as a function of Ga concentration. The variations may indicate that many of the TSC and TL peaks are caused by uncontrolled impurities introduced during growth.

We analyzed the TSC spectra to obtain values of frequency factors and activation energies for the traps responsible for the peaks in the spectrum, but since the analysis

is very detailed it will be presented by itself in Chapter 4.

2.3 Summary

The work presented here indicates that $Bi_{12}GeO_{20}$ and $Bi_{12}SiO_{20}$ are highly defective materials with complex absorption, photoconductivity and TSC spectra. Czochralski-grown samples exhibit a characteristic absorption shoulder which is probably due to an anti-site Bi defect. Illumination with sub-band-edge light induces additional absorption and photoconductivity bands as well as TSC signals, but not TL. The induced absorption consists of several bands, consistent with the photoconductivity spectra and the dark conductivity results.

Chapter 3

TL and TSC theory

3.1 Introduction

TSC and TL are two particularly useful methods for studying deep levels within a semiconductor's or insulator's band gap due to their sensitivity and to the wide variety of methods which have been developed to extract trapping parameters such as frequency factors and activation energies. These methods include initial rise [48], Hoogenstraaten's method [49], Chen's peak shape method [50], curve fitting and many others [51].

An illustration of the TSC and TL process is shown in Fig. 3.1. A TSC or TL measurement is performed by first illuminating the sample at a suitably low temperature with light energetic enough to excite free charge carriers into the delocalized bands. The free carriers drift and diffuse until they either recombine or become trapped at trapping sites, so that upon heating the trapped carriers are thermally detrapped at some temperature resulting in an increase in sample conductivity (TSC). TL is observed when the thermally detrapped carriers recombine radiatively. The TL and TSC intensity depend on the concentration of filled traps.

There are a number of models used to describe TL and TSC, the simplest of which is shown in Fig. 3.2. This simple model assumes a material with only one trap and one recombination center. Real materials are more complicated, often having

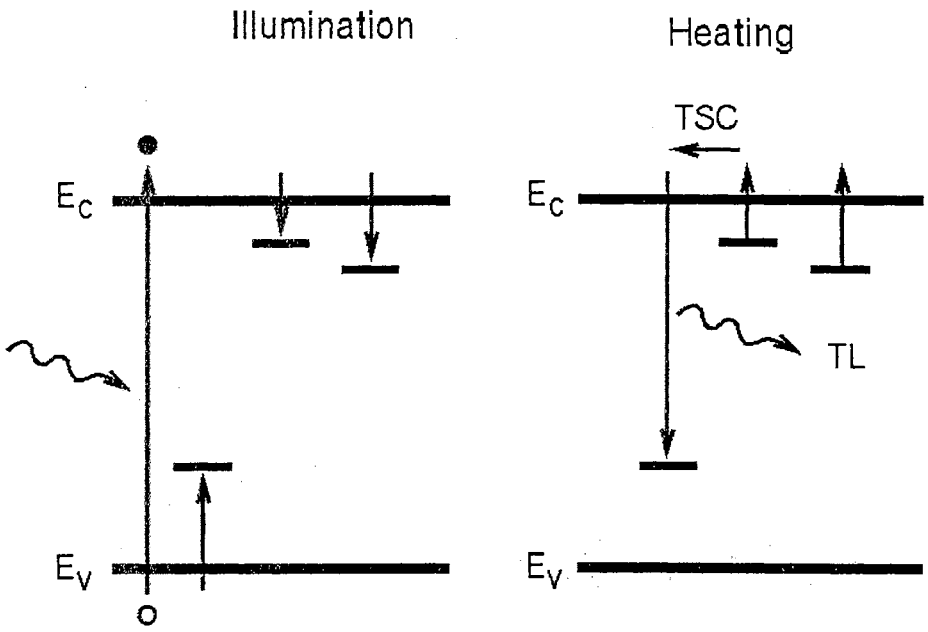

Figure 3.1: Illustration of the TL and TSC process.

multiple traps for both holes and electrons, but nevertheless the simple model provides important insight into the TL and TSC processes. During illumination free electrons are excited from the valence band to the conduction band leaving free holes behind. The free electrons can be trapped or may recombine with free holes or with holes trapped at the recombination center. Trapped electrons have a probability, $\gamma_t = s^{-1}\exp(-E_t/k_bT)$, of being thermally excited out of the trap back into the conduction band where they may be retrapped or recombine. Here E_t is the activation energy of the trap, s is the frequency factor, k_b is Boltzmann's constant and T is temperature. In most measurements the sample temperature is low enough to make the probability of thermal emission insignificant during the illumination cycle.

The differential equations describing the flow of charge during illumination are

$$\frac{dn_c}{dt} = f - n_c(N_t - n_t)A_t + \gamma_t n_t - n_c n_v A - n_c n_h A_r, \tag{3.1}$$

$$\frac{dn_t}{dt} = -\gamma_t n_t + n_c(N_t - n_t)A_t, \tag{3.2}$$

$$\frac{dn_v}{dt} = f - n_c n_v A - n_v(N_h - n_h)A_h, \tag{3.3}$$

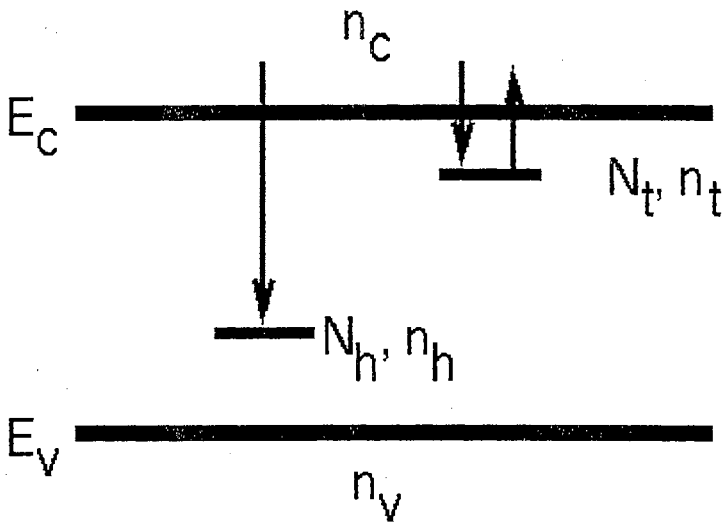

Figure 3.2: Simple model to describe TL and TSC.

$$\frac{dn_h}{dt} = -n_c n_h A_r + n_v(N_h - n_h)A_h. \tag{3.4}$$

The concentrations are defined as follows: n_c — conduction band, n_v — valence band, n_t — trapped carrier, n_h — holes at recombination center, N_t — total trap, and N_h — total concentration of recombination centers. The transition coefficients are: A_t — trapping of free electrons, A_h — capture of free holes at the recombination center, A_r — recombination of free electrons with holes at the recombination center and A — recombination of free electrons with free holes. The transition coefficients are equal to the product of the thermal velocity of the carriers and the capture cross-section of the center. f is the generation rate of free carriers (dependent on the light intensity). One last equation can be written to express the requirement of charge neutrality, namely

$$n_c + n_t = n_v + n_h. \tag{3.5}$$

The first term in Eq. (3.1) accounts for generation of free electrons by the illumination and the second for capture of free electrons by the traps. The third term accounts for thermal detrapping from the trap to the conduction band. Recombination of free

electrons with free holes and of free electrons with holes at the recombination center are accounted for by the fourth and fifth terms, respectively. Eq. (3.2) contains no new terms and the first 2 terms of Eq. (3.3) have been described as well. The last term in Eq. (3.3) accounts for capture of free holes at the recombination site. The equations describing the heating cycle are the same except $f = 0$ and γ_t is no longer a constant since the temperature is changing. We wish to derive an expression for the TL intensity during heating. In this model the recombination center, N_h, is the only radiative recombination pathway, so the TL intensity is proportional to the rate at which the concentration of filled recombination centers decreases, i.e.

$$I_{TL} = -\frac{dn_h}{dt}. \tag{3.6}$$

If we assume that the holes at the recombination center are not thermally ejected to the valence band during the heating cycle then we can reduce the number of differential equations to three since the valence band will play no part. In this case the valence band concentration will be zero during the entire measurement, so eliminating Eq. (3.3) and setting $n_v = 0$ in the other equations leaves us with

$$\frac{dn_t}{dt} = -\gamma_t n_t + n_c(N_t - n_t)A_t \tag{3.7}$$

$$\frac{dn_h}{dt} = -n_c n_h A_r. \tag{3.8}$$

$$\frac{dn_c}{dt} = \frac{dn_h}{dt} - \frac{dn_t}{dt} \tag{3.9}$$

Unfortunately an analytical solution to these equations is not possible as they stand, so we must resort to approximations. A common assumption is that of "quasiequilibrium" which is expressed as,

$$\frac{dn_c}{dt} \ll \frac{dn_t}{dt}, \tag{3.10}$$

$$n_c \ll n_t. \tag{3.11}$$

These two expressions require that the conduction band concentration be slowly varying and small compared to the trapped carrier concentration. It should be noted that

expressions for TSC and TL have been derived without the quasi-equilibrium approximation [52]. Applying the first approximation to Eq. (3.9) yields

$$\frac{dn_h}{dt} \approx -\frac{dn_t}{dt}. \tag{3.12}$$

Substituting Eqs. (3.7) and (3.8) into Eq. (3.12) and solving for n_c gives,

$$n_c = \frac{\gamma_t n_t}{n_h A_r + (N_t - n_t) A_t}. \tag{3.13}$$

Now substituting this result into Eq. (3.8) leads to

$$I_{TL} = -\frac{dn_h}{dt} = s n_t \exp\left(\frac{-E_t}{k_b T}\right) \frac{n_h A_r}{n_h A_r + (N_t - n_t) A_t}. \tag{3.14}$$

An analytical solution is still not possible so it is necessary to make another approximation. One assumption that is often valid is that recombination dominates over retrapping. This assumption can be written as

$$n_h A_r \gg (N_t - n_t) A_t. \tag{3.15}$$

Under this approximation Eq. (3.14) becomes

$$I_{TL} = \frac{dn_t}{dt} = s n_t \exp\left(\frac{-E_t}{k_b T}\right). \tag{3.16}$$

Eq. (3.16) can be integrated. Normally a linear heating rate, β, is used so $T = T_0 + \beta t$ where T_0 is the starting temperature. Performing the integration gives

$$n_t = n_{t0} \exp\left[-\frac{s}{\beta} \int_{T_0}^{T} \exp\left(\frac{-E_t}{k_b \theta}\right) d\theta\right] \tag{3.17}$$

where n_{t0} is the initial trapped carrier concentration. Substituting Eq. (3.17) back into Eq. (3.16) we find

$$I_{TL}(T) = n_{t0} s \exp\left(\frac{-E_t}{k_b T}\right) \exp\left[-\frac{s}{\beta} \int_{T_0}^{T} \exp\left(-\frac{E_t}{k_b \theta}\right) d\theta\right]. \tag{3.18}$$

This is the Randall and Wilkins expression [53]. It is a first-order expression because the trapped carrier concentration appears to the first power in the prefactor. For TSC the equivalent expression is

$$I_{TSC}(T) = Ae\mu\varepsilon\tau n_0 s \exp\left(-\frac{E_t}{k_b T}\right) \exp\left[-\frac{s}{\beta}\int_{T_0}^{T} \exp\left(-\frac{E_t}{k_b \theta}\right) d\theta\right]. \tag{3.19}$$

Here A is the electrode area, e is the electronic charge, μ is the mobility, ε is the applied electric field and τ is the free carrier lifetime. The Randall-Wilkins expression for TL produces asymmetric peaks like that shown in Fig. 3.3. The asymmetry of the peak is a characteristic feature of first-order kinetics, whereas second-order kinetics produces peaks which are more symmetrical. The peak position of first-order peaks depends on the activation energy and frequency factor.

The first-order expression in Eq. (3.18) was derived for the case of no retrapping of detrapped carriers. If the retrapping of thermally freed carriers is important a second-order peak results. A second-order expression can be derived from Eq. (3.14) by making the following assumptions: 1) $n_t \approx n_h$, 2) $(N_t - n_t)A_t \gg n_h A_r$ and 3) $N_t \gg n_t$. Applying these assumptions to Eq. (3.14) gives the second-order expression

$$I_{TL} = \frac{dn_t}{dt} = {n_t}^2 \left(\frac{sA_r}{N_t A_t}\right) \exp\left(\frac{-E_t}{k_b T}\right). \tag{3.20}$$

For a second-order peak the TL and TSC intensity is proportional to n_0^2 rather than n_0 as for a first-order peak. First-order TL and TSC peaks grow with n_0, but do not change shape or position as n_0 is varied. The position and shape of non-first-order peaks, however, do depend on n_0. Monitoring the position of a TL or TSC peak as a function of initial filled trap concentration, then, is one method of determining the order of kinetics associated with the given peak.

The simple model provides us with a good basis for understanding TSC and TL kinetics, but real materials are much more complicated. A material described by the simple model would have only one TL peak and the emission would be at a single

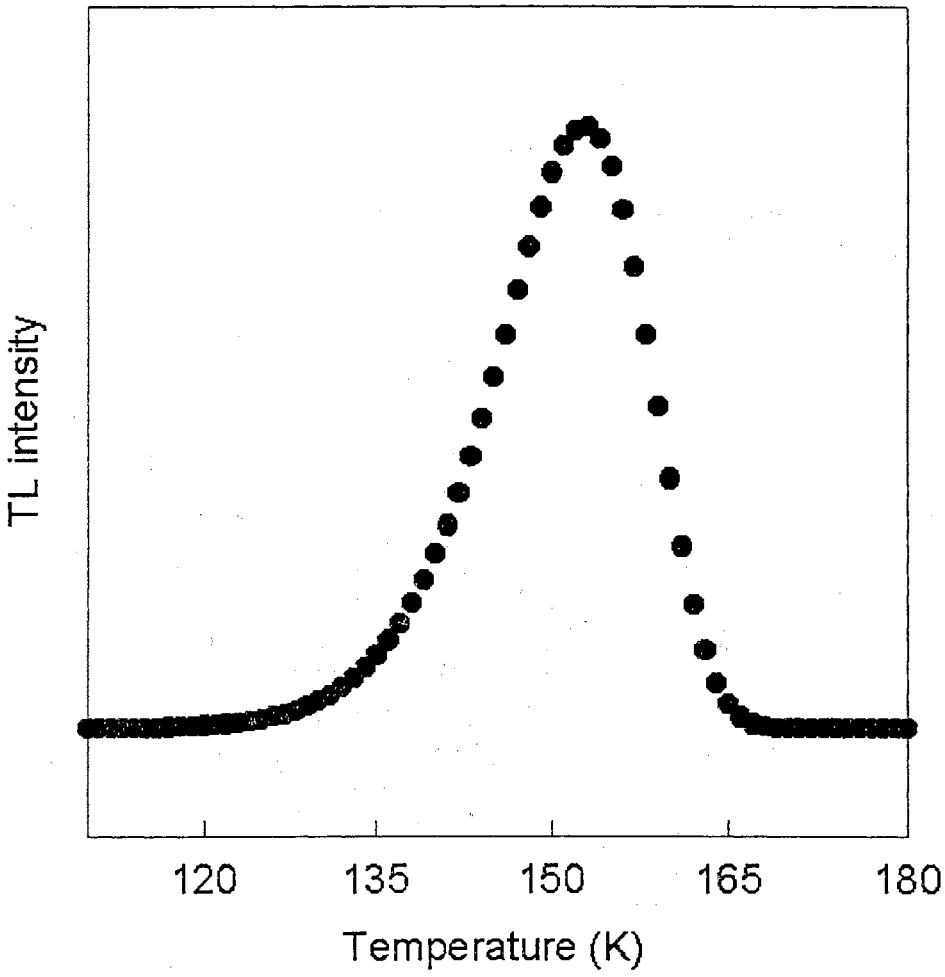

Figure 3.3: A first-order TL peak generated using Eq. (3.18)

wavelength. Normally, a number of peaks are observed and emissions at several wavelengths or over a range of wavelengths are common. One extension to the simple model is the addition of a thermally disconnected trap. A thermally disconnected trap is one in which the trap depth is so great that any carriers trapped at the level are unable to be detrapped at the temperatures reached during the measurement. Chen, et al. [54], found that the kinetics tended towards first-order when the number of carriers trapped in thermally disconnected traps was much greater than the number of trapped carriers at the non-thermally disconnected trap. When the number of carriers in the shallow trap was much greater than the number in the thermally disconnected trap the kinetics were second-order.

It is important to understand the correlation between TSC and TL peaks as both TSC and TL measurements can be performed simultaneously. From Eq. (3.14) we know that $I(t) = -dn_h/dt$, so we have

$$I(t) = n_c n_h A_r. \tag{3.21}$$

Differentiating Eq. (3.21) with respect to time gives

$$\frac{dI}{dt} = \frac{dn_c}{dt} n_h A_r + n_c \frac{dn_h}{dt} A_r = \frac{dn_c}{dt} n_h A_r - n_c^2 n_h A_r^2. \tag{3.22}$$

The second equality follows from Eq. (3.8). At the maximum of a TL peak we must have $dI/dt = 0$, and Eq. (3.22) shows that this can only be true if $dn_c/dt > 0$, or in other words, we have not yet reached the maximum of the TSC peak. Therefore we should expect that the maximum of a TL peak will occur at a temperature lower than the corresponding TSC peak. Sometimes, however, this is not the case. If the concentration of filled recombination centers, n_h, is very large compared to the trapped electron concentration then their numbers won't be reduced very much during the measurement. In this case $dn_h/dt \approx 0$ and the second term in Eq. (3.22) is zero and the TSC peak will no longer occur after the TL peak.

An implicit assumption in this development so far is that the trap responsible for the TSC and/or TL has a discrete frequency factor and activation energy. It has been suggested by some authors [55-57] that this may not be the case, so expressions describing TL and TSC from traps with Gaussian, exponential or rectangular energy distributions have been derived. In the case of a distribution of activation energies Eq. (3.18) needs to be modified to include an integral over the energy distribution. It becomes [51]

$$I_{TL}(T) = \int_{E_{min}}^{E_{max}} n(E') s \exp\left(-\frac{E'}{k_b T}\right) \exp\left[-(s/\beta)\int_{T_0}^{T} \exp\left(-\frac{E'}{k_b \theta}\right) d\theta\right] dE' \quad (3.23)$$

where $n(E')$ describes the distribution. For a uniform distribution with low energy and high energy limits of E_1 and E_2, respectively

$$n(E) = \frac{n_0}{\Delta E} \quad (3.24)$$

where $\Delta E = E_2 - E_1$. For an exponential distribution from 0 to E_{max}

$$n(E) = n_e \exp\left(\frac{E - E_{max}}{k_b T_c}\right) \quad (3.25)$$

where T_c is a characteristic temperature describing the distribution. For a Gaussian distribution of energy states $n(E)$ has the form

$$n(E) = n_m \exp\left[\left(\frac{E - E_0}{\sigma_E}\right)^2\right] \quad (3.26)$$

where n_m is the concentration of states at the center of the distribution, E_0, and σ_E is the standard deviation of the energy states contained in the distribution.

The assumption of a Gaussian or exponential distribution results in an expression that contains an integral, but an analytical expression has been found for the case that the distribution of energy states is uniform. This may be important if the expression is going to be used for curve fitting as numerical evaluation of integrals is computationally expensive. By substituting Eq. (3.24) into Eq. (3.23) we get

$$I_{TL}(T) = \frac{n_0 s}{\Delta E}\int_{E_1}^{E_2} \exp\left(\frac{-E'}{k_b T}\right) \exp\left[-(s/\beta)\int_{T_0}^{T} \exp\left(\frac{-E'}{k_b \theta}\right) d\theta\right] dE'. \quad (3.27)$$

Hornyak and Chen [57] approximated the integral over temperature using

$$\int^{T} \exp\left(\frac{-E}{k_b\theta}\right) d\theta \simeq T \exp\left(-E/k_bT\right) \sum_{n=1} \left(k_bT/E\right)^n \left(-1\right)^{n-1} n!. \tag{3.28}$$

The infinite series can be truncated after the first two terms and for sufficiently narrow distributions E can be replaced by the value of E at the center of the distribution, E_0, everywhere except in the exponential resulting in

$$\int^{T} \exp\left(\frac{-E}{k_b\theta}\right) d\theta \approx \frac{-sk_bT^2}{\beta E_0} \exp\left(\frac{-E}{k_bT}\right)\left(1 - \frac{2k_bT}{E_0}\right). \tag{3.29}$$

After substituting Eq. (3.29) into Eq. (3.27) the integral over E can be performed. The result is

$$I_{TSC}(T) = \frac{n_0 s k_b T}{\gamma \Delta E}\left[\exp\left(-\gamma \exp\left(\frac{-E_2}{k_bT}\right)\right) - \exp\left(-\gamma \exp\left(\frac{-E_1}{k_bT}\right)\right)\right] \tag{3.30}$$

where

$$\gamma = \frac{sk_bT^2}{\beta E_0}\left(1 - \frac{2k_bT}{E_0} + \frac{6k_bT^2}{E_0^2} - \cdots\right). \tag{3.31}$$

Hornyak and Chen found that due to the approximations used in deriving this expression it is valid only for $\Delta E \leq 0.1$ eV. A theoretical TSC peak generated using this expression is shown in Fig. 3.4. The TSC peak resulting from a trap characterized by a distribution of activation energies is substantially broadened on the high temperature side. It's interesting to note the similarities in shape between this theoretical peak and some of the TSC peaks measured during the TSC experiments reported in Chapter 4, especially for the Ga-doped sample as illustrated in Fig. 4.11(a) on page 74.

3.2 Methods of Analysis

The motivation for developing a model to describe TL and TSC is to find a method for extracting trapping parameters, such as frequency factors and activation energies,

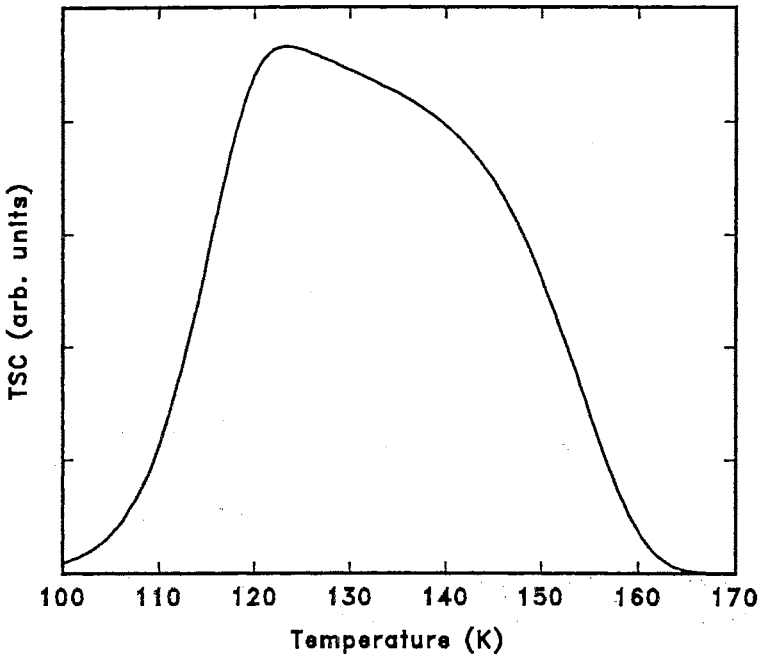

Figure 3.4: Theoretical peak generated using Eq. (3.31).

from the data. A large number of methods have been developed and used, but most, if not all, of the methods can be applied successfully only if certain conditions are met. Overlapping peaks cause problems for methods which rely on peak position or shape because the maximum of a composite set of peaks may be shifted from its true value and the rising and descending portions of the peak may be distorted as well. Thermal cleaning techniques can sometimes be used to help isolate individual peaks.

One commonly used method of analysis is the initial rise technique [48]. From Eq. (3.16) the early portion of a TSC or TL peak is seen to be exponentially dependent on temperature such that

$$TL/TSC \simeq const \times \exp\left(\frac{-E_t}{k_b T}\right). \tag{3.32}$$

The activation energy E_t is found by making a plot of $\ln I$ vs. 1/T. Such a plot should produce a straight line with a slope of $-E_t/k_b$. There is a limitation in that the prefactor can only be assumed to be a constant over a limited temperature interval, so only the part of the peak corresponding to less than 10% or 15% of the maximum

peak intensity should be used in the plot.

A complication with this method is that it requires a very "clean" low temperature side of the peak. Any peak overlap in this region will render this simple method useless, but unfortunately peak overlap is very common. In the case of peak overlap various thermal cleaning methods may be useful [51].

Another method is Chen's peak shape method [50]. Chen's method uses the peak symmetry to provide three estimates for the activation energy of the trap responsible for the peak. Chen uses the three temperatures T_m, T_1 and T_2 defined as follows: T_m — temperature at which the peak maximum occurs, T_1 — temperature at half the peak maximum on the rising portion of the peak and T_2 — temperature at half the peak maximum on the descending portion of the peak. Chen defines the three parameters $\delta = T_2 - T_m$, $\tau = T_m - T_1$ and $\omega = T_2 - T_1$. Then the activation energy is determined using

$$E_\gamma = c_\gamma \frac{kT_m^2}{\gamma} - b_\gamma 2kT_m \tag{3.33}$$

where γ takes on the values ω, τ or δ. The values of the constants c_γ and b_γ were calculated by Chen and are given in reference [50]. Chen calculated these constants for general order kinetics, so the method is not limited to first-order peaks.

Hoogenstraaten's method of variable heating rates is another method for determining frequency factors and activation energies [49]. This method takes advantage of the shift in peak position for different heating rates as shown by Eq. (3.17). To apply this method several TL or TSC measurements are performed using identical illumination cycles, but different heating rates. A plot of $\ln(T_m^2/\beta)$ vs. $1/T_m$ should have a slope of E_t/k_b and a y-intercept of $\ln(E_t/sk_b)$. This method has the disadvantage that peak overlap can cause shifts in the peak position so that the true peak position is unknown.

Another method of analysis is peak fitting. Peak fitting involves adjusting an

expression that describes the peak shape by varying parameters so that the resulting shape matches that of the experimentally measured peak. The Levenberg-Marquardt routine is a commonly used and reliable least-squares fitting method. Fitting has the advantage that entire spectra can be fit even in the case that there are many overlapping peaks. It may also be possible to find peaks which are not visible in the spectra. In order to do peak fitting a functional form for the peak has to be assumed. In theory an expression like Eq. (3.18) could be used to do the fitting, but this may be impractical since the integral has to be evaluated numerically on every iteration. Keating, however, approximated the integral using an asymptotic series and arrived at a closed-form expression [58], written here in the TSC equation as

$$I_{TSC}(T) = Ae\mu\varepsilon\tau n_0 s \exp\left(\frac{-E_t}{k_b T}\right) \exp\left[-\frac{k_b s T^2}{\beta E_t}\left(1 + \frac{(b-4)k_b T}{E_t}\right) \exp\left(\frac{-E_t}{k_b T}\right)\right]. \tag{3.34}$$

The frequency factor in this development is assumed to be proportional to T^{2-b} where $0 \leq b \leq 4$. This expression doesn't contain an integral, so it can be evaluated quickly by a computer. In this expression the fitting parameters become E_t, s, b and $K = Ae\mu\varepsilon\tau n_0$.

As mentioned earlier it may be difficult to extract meaningful parameters from TSC or TL data because of peak overlap. When two or more peaks overlap the peak maxima may be shifted from their true values and both the rising and descending portions may be distorted. For the case of severe overlap or if one peak is much larger than its neighbor it may not even be possible to see more than one maximum. These methods of analysis may also have trouble even when it is not obvious that there is more than one peak present. If a peak is hidden under a larger peak treating the composite like a single peak may result in parameters which are invalid. Due to the difficulties of analyzing overlapping peaks "thermal cleaning" techniques have been devised whereby a heating cycle is used to remove the lower temperature peak

or peaks in a composite peak. After the initial thermal cleaning cycle the sample is immediately cooled back down and the TSC or TL reading is performed normally.

One of these methods is the T_m-T_{stop} method which was developed by McKeever [59]. It has the advantage that it not only separates overlapping peaks, but it can also find hidden peaks and give information as to the number of peaks making up the composite. The T_m-T_{stop} method involves deconvoluting overlapping peaks using a series of thermal cleaning cycles to successively higher temperatures, T_{stop}. The values of T_{stop} are chosen to correspond to the temperature range over which the composite peak occurs and the temperature increment between successive cycles should be chosen to be small ($\sim$3–5 K) if fine resolution is desired. After performing the measurements the temperature at which the first TSC/TL peak maximum occurs, T_m, is plotted vs. T_{stop}. This graph should look like a staircase with each step being due to a separate peak in the spectrum. The staircase pattern is expected because the TSC peak maximum should move from one component peak to an adjacent peak after the first peak is sufficiently reduced in size by the thermal cleaning cycle. It is possible that the peaks are so close together that this method will be unable to separate them. In this case a plot of T_m vs. T_{stop} will produce a straight line of slope approximately equal to 1. This method has the disadvantage that it takes a long time because many measurements have to be performed, each with a thermal cleaning cycle and subsequent cool down. If the composite peak is very broad a wide range of T_{stop} values have to be used as well. Also, only prominent peaks will show up in the T_m vs. T_{stop} plots. Peaks which are completely hidden by their neighbors may not be big enough to show up.

Another method involving thermal cleaning cycles is the method of Gobrecht and Hofman called the 'fractional glow technique' [60]. This technique involves performing a series of heating and cooling cycles to successively higher temperatures during which

the TL signal is recorded during both heating and cooling. A plot of $\ln I$ vs. $1/T$ is made and the activation energies are obtained from the slope as in the initial rise method. If the temperature increment between cycles is small the slope obtained from the heating portion should be close to that obtained during the cooling phase and the average can be taken to calculate the activation energy. This method deals with one problem with the initial rise technique, namely that the number of trapped carriers needs to be approximately constant. If a small temperature increment is chosen this condition is satisfied. The two primary problems with this method are that enormous amounts of data are collected which have to then be analyzed and for good results the temperature needs to be controlled very precisely. This can be difficult when undergoing a transition from heating to cooling or vice versa.

The determination of accurate values of trapping parameters from TL and TSC data can be a difficult undertaking due to the problems with separating individual peaks in the spectra. The best analysis would probably involve performing thermal cleaning cycles before measurements of the spectra and then using several methods to determine parameters such as activation energies and frequency factors. It would also be advantageous to do several identical measurements and fit all the resulting data. This would help to give an estimation of the size of the experimental errors involved in the measurement of the spectra.

Chapter 4

TL and TSC Analysis

In Chapter 2 the results of TSC measurements performed on undoped and 2% Ga-doped BGO were presented, but the analysis was deferred until this chapter. The proper analysis of TSC spectra is important because of the role played by the traps in other measurements and applications. For example, measurements of mobility in BGO and BSO using the time-of-flight technique are strongly affected by the presence of traps and it will be shown in Chapter 5 that the dominant peak in the TSC spectra of undoped BGO, which is centered at about 150 K, is caused by the same trap that limits the drift mobility at temperatures between 200 K and 300 K.

4.1 Results

4.1.1 General Description of the TSC Curves

TSC curves from an undoped BGO sample and a 2% Ga-doped BGO sample are shown in Fig. 4.1. The TSC displayed by both samples is similar, consisting of a series of large peaks below 160 K and a number of smaller overlapping peaks at higher temperatures. The large peaks below 160 K in both types of sample will be referred to as the "low temperature peaks" and the peaks above 160 K will be called the "high temperature peaks." The TSC observed in the undoped sample for

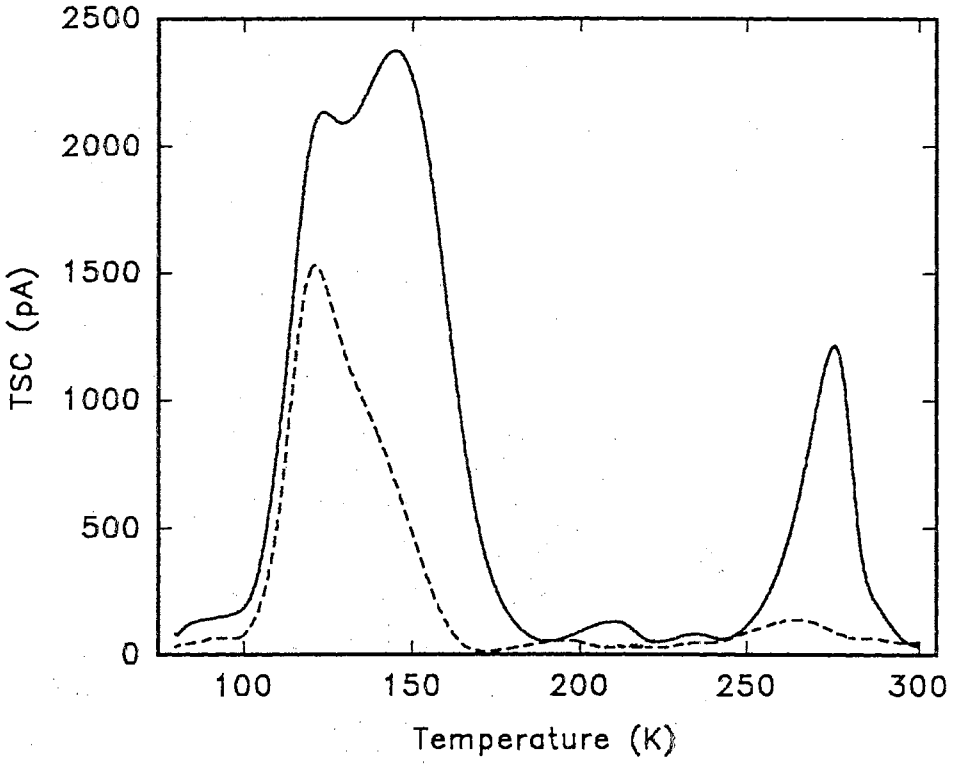

Figure 4.1: TSC spectra produced by 412 nm excitation of undoped BGO (solid line) and Ga-doped BGO (dotted line).

different illumination times at 412 nm is shown in Fig. 4.2. The positions of the two peaks at about 210 K and 230 K stay the same independent of the illumination time verifying that the traps responsible for these peaks are first-order, i.e. the thermally freed carriers are not retrapped. A shift in the peak position is seen in the peak at about 280 K, but we believe this peak is a composite consisting of at least two components and the shift in peak position is the result of the changing relative sizes of the individual components. Therefore it is believed that this peak is also a first-order peak.

The broad peak below 160 K in undoped BGO is seen to consist of two components. Only the high temperature component appears for short illuminations, but as the illumination time is increased a shoulder appears on the low temperature side of the peak. For long illumination times the lower temperature component appears as a 2nd peak almost equal in height to the higher temperature peak component. The different growth rates of the two peaks can be explained by assuming that the trap responsible for the higher temperature component has a larger capture cross-section than does the lower temperature component. The trap with the smaller capture cross-section will not begin to fill appreciably until the trap with the larger capture cross-section is populated to the point that the trapping probabilities for each trap are comparable. Although these peaks shift slightly to lower temperatures as the illumination time (and therefore n_0) increases our analysis, to be described later, indicates that these too are first-order peaks. The apparent shift is again a consequence of peak overlap.

Fig. 4.3(a) shows the TSC signal for different illumination times at 412 nm in Ga-doped BGO. Again the peaks appear to be first-order. There is a slight shift of the peak at $\sim$210 K to lower temperatures as the illumination time is increased, but this is likely due to the increase in size of the peak at $\sim$190 K. Fig. 4.3(b) is a plot of the

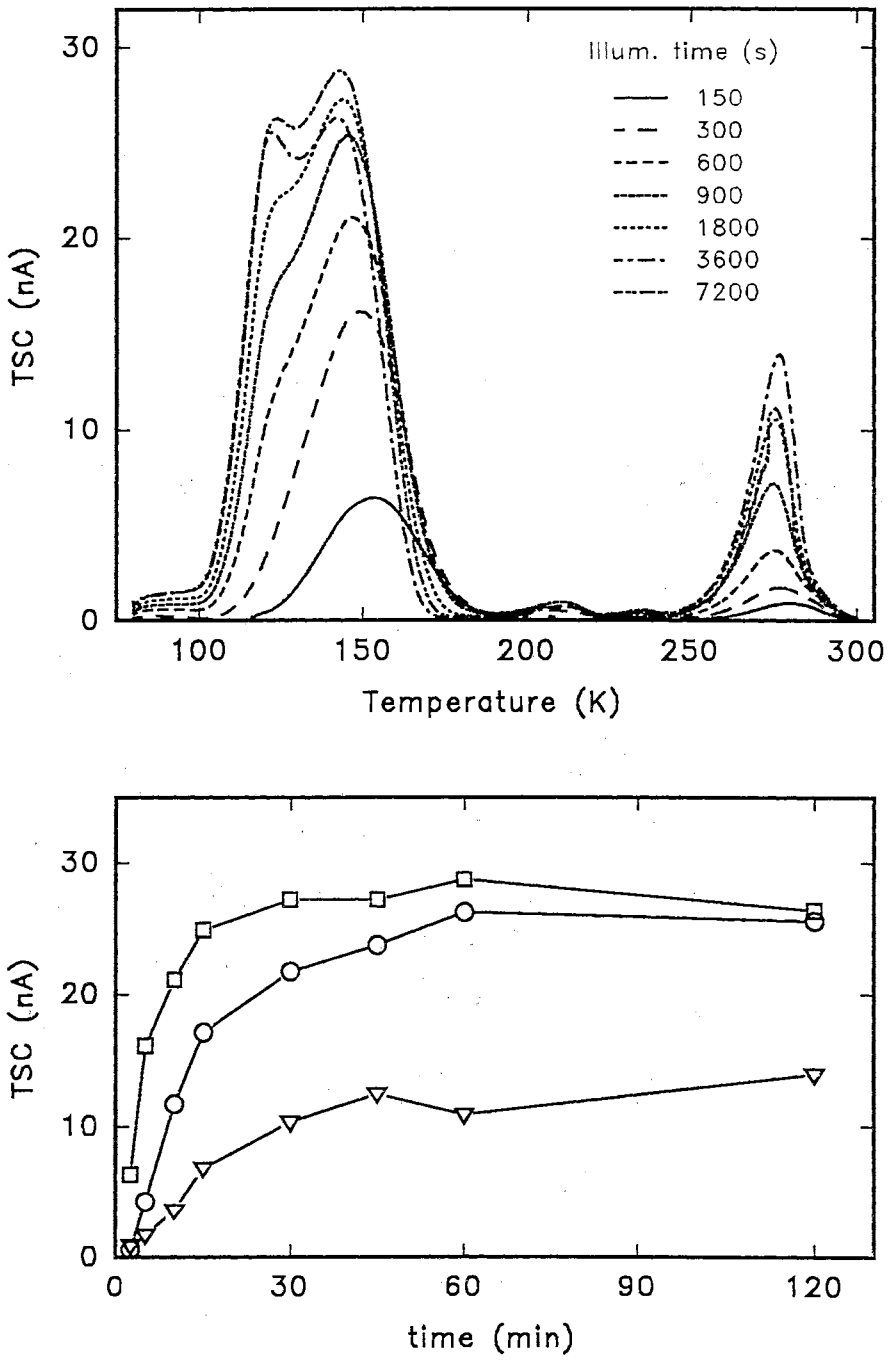

Figure 4.2: (a) TSC spectra for undoped BGO for varying illumination times at 412 nm. (b) Growth of the TSC peaks shown in (a) with illumination time. The peak positions are: ∘120 K, △ 142 K and □280 K.

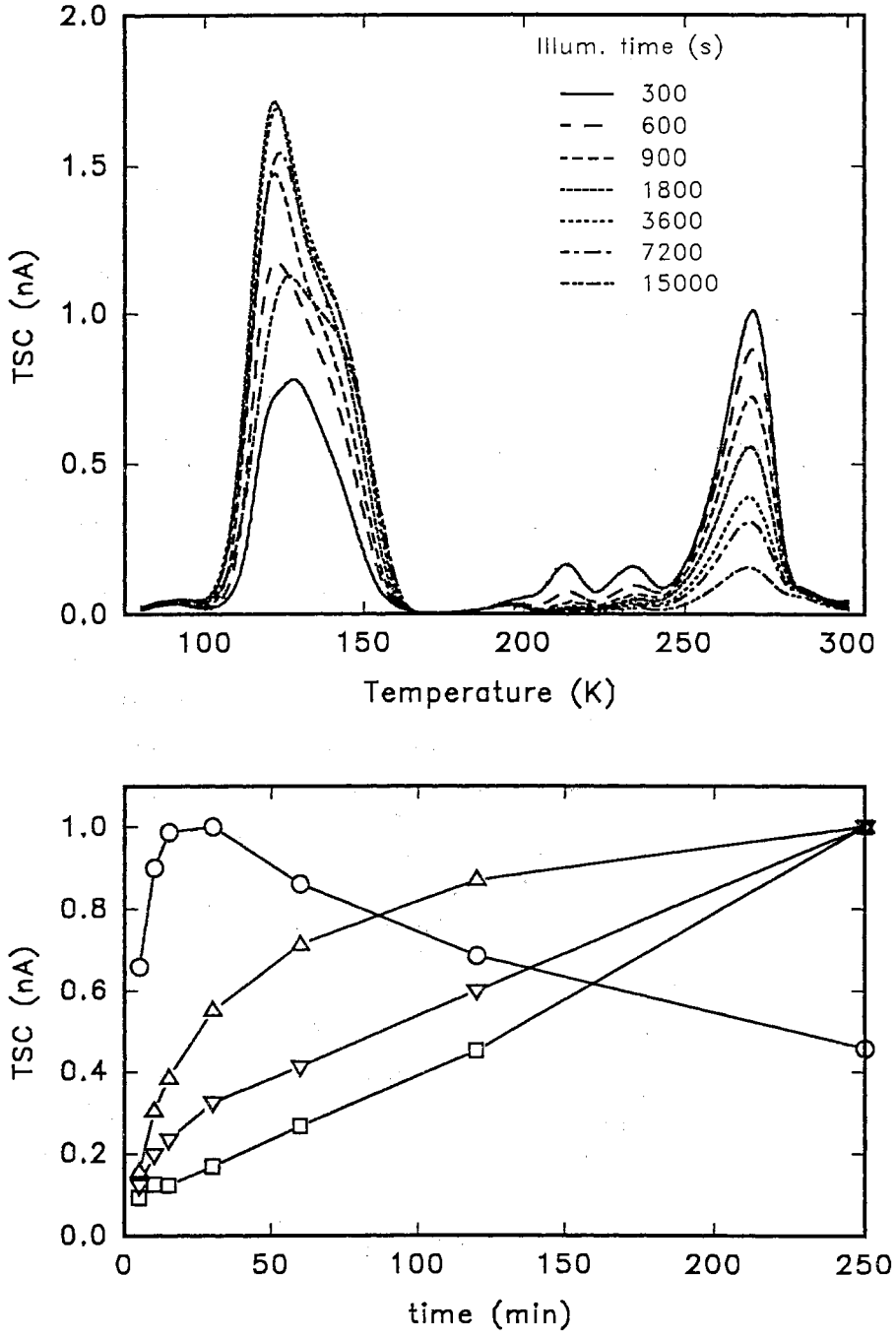

Figure 4.3: (a) TSC spectra of Ga-doped BGO for varying illumination times at 412 nm. (b) Growth of the TSC peaks shown in (a) with illumination time. The peak positions are: ○120 K, □213 K, △230 K, and ▽275 K.

height of the peak maximum versus illumination time for the peaks centered at about 120 K, 210 K, 230 K and 275 K. The three higher temperature peaks increase in size as the illumination time is increased, as expected, but the 120 K peak increases in size for a short time only and then gradually decreases. Fig. 4.2(b) shows that this type of behavior is not observed in the 120 K peak in the undoped BGO sample. The decrease in the size of the peak in the Ga-doped sample as the illumination time is increased is most likely a consequence of two effects. Firstly, the optical excitation may be exciting trapped electrons from the 120 K trap into the conduction band where they are free to recombine or be retrapped at other trapping sites. Secondly, the donor level is most likely being depleted of electrons. If this was not the case we would expect that the trap occupancy, and therefore the peak height, would asymptotically approach a maximum as the rate of trap filling became equal to the rate of trap emptying. This is the behavior that is likely being observed in the undoped BGO sample. The presence of the maximum in Fig. 4.3(b) indicates that the rate of trap filling is decreasing. The assumption that the deep donor level is being depleted is reasonable since gallium acts as an acceptor in BGO. As explained in Chapter 2, the addition of gallium causes a decrease in the Fermi Level. For sufficiently high gallium concentrations the Fermi Level is decreased to such an extent that some of the deep donor levels no longer contain electrons. Additional support for these conclusions comes from studying the areas under the TSC peaks of Fig. 4.3(a). We found that as the illumination time increased the total area contained under the TSC peaks from 80 K to 300 K decreases. Since the area under a TSC peak is proportional to the total number of carriers trapped the decrease in area corresponds to a decrease in the number of trapped carriers. The decrease in the number of trapped carriers is caused by optical excitation of carriers out of the traps responsible for the peaks seen in the TSC spectrum from 80 K to 300 K and then retrapping into traps which are thermally

unstable above 300 K. Electrons occupying traps above 300 K are effectively "lost" for the duration of the measurement since the samples were heated only to 300 K. Since these electrons are not being replaced in the traps between 80 K and 300 K we conclude that the donor level is being depleted.

The peak below 160 K in the Ga-doped sample is different than the corresponding peak in the undoped BGO sample in that only the lower temperature component is present. The shoulder on the high temperature side is shown by our analysis (to be described) to be part of the same peak rather than a separate 2nd component. This unusual peak shape is due to the activation energy of the trap responsible for the peak being distributed around a central value rather than being single valued. As shown in Chapter 3, a trap that is characterized by a distribution of activation energies exhibits TSC and TL peaks that are substantially broadened, especially on the high temperature side.

4.1.2 Analysis

As explained in the previous chapter many techniques have been developed for the analysis of TSC and TL data to yield values for trapping parameters. The methods we used are Hoogenstraaten's method of variable heating rates [49], the initial rise technique [48], Chen's peak shape method [50] and curve fitting. Since our data show many overlapping peaks additional experiments were performed in which a preheating cycle was used to "thermally clean" lower temperature portions of the peak structure. The thermal cleaning process allows the higher temperature components of the peak structure to be seen more clearly by eliminating, or at least reducing in size, the lower temperature components of a composite peak. During the thermal cleaning cycle the sample was heated to a temperature which was high enough to thermally empty the trap or traps responsible for the low temperature components of the peak

structure without substantially affecting the occupancy of the trap responsible for the component peak of interest. The sample was then cooled to the initial starting temperature and a standard TSC or TL measurement was performed. This method allowed us to more clearly identify the number of peaks present and to apply several methods of analysis to the resulting data. It should be noted that no formal analysis was performed on the TSC signal seen in the range from 80 K to about 100 K. No peak is clearly identifiable in this temperature range, and the TSC existing here is probably a composite peak caused by several traps becoming thermally unstable over this region. In addition, there is most likely substantial overlap with the large peak adjacent to it adding another complication to the analysis of this region.

High Temperature Peaks

The analysis of the peaks above 160 K is difficult due to the many overlapping peaks present throughout this temperature range. Also, the high temperature tail of the large peak below 160 K may be hiding or distorting smaller peaks in the temperature range from 160 K to 180 K. To more clearly see the high temperature peak structure a thermal cleaning cycle was used to eliminate the large peaks below 160 K. Fig. 4.4 shows TSC data taken on both the undoped and 2% Ga-doped samples after preheating cycles were performed to the indicated temperature (T_{stop}). A slow heating rate of 3 K/min was used to avoid thermal gradients across the sample. A higher value for the stop temperature of the preheating cycle was used for the undoped sample than for the Ga-doped sample because the large peak extends to a higher temperature in the undoped sample than in the Ga-doped sample. The preheating cycle for the Ga-doped sample included a 300 second delay at 155 K before cooling back to 80 K. This delay further reduced the size of the large peak below 160 K while having a minimal effect on the peaks above this temperature. These data show more clearly

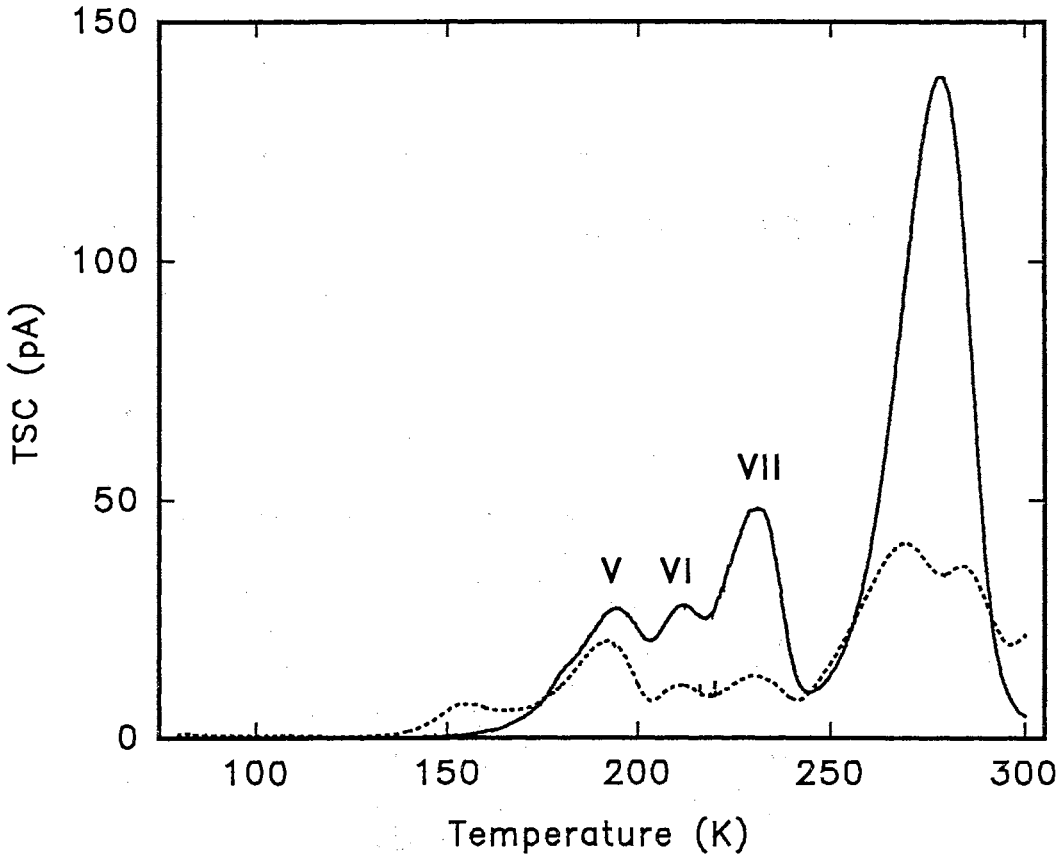

Figure 4.4: TSC spectra for undoped BGO (solid line) after a preheating cycle to 191 K and for Ga-doped BGO (dotted line) after a preheating cycle to 155 K.

the peak structure of the high temperature peaks. The data reflect a complex trap distribution.

The peak at ~155 K seen in the data for the Ga-doped sample is the remnant of the large, low temperature peak, as is the low temperature shoulder seen on the 1st peak in the data for the undoped sample. The next three peaks at approximate temperatures of 190 K, 210 K and 230 K, and which were labelled peaks V, VI and VII, respectively Chapter 3, are seen in both samples. There could also be one or more peaks hidden beneath peaks V, VI and VII. In the undoped sample only one more peak is clearly visible, at a temperature of ~280 K, although it appears that there may be a small peak at ~250 K also. In the Ga-doped sample the peak structure from 240 K to 280 K shows two overlapping peaks at ~270 K and ~280 K with quite possibly a third, also at ~250 K. Due to the many overlapping peaks throughout this temperature range the extraction of meaningful trapping parameters proved to be difficult. Additional thermal cleaning cycles to further isolate a single peak were of limited use because there is substantial overlap of each of these peaks on the high temperature side. Only peaks overlapping on the low temperature side of the peak of interest can be eliminated, or at least reduced in size. Since there is so much overlap between the peaks, the peak position and peak shape methods of analysis were considered to be unreliable, and therefore curve fitting was used to analyze the peaks in the temperature range from 180 K to 300 K. Eq. (3.34) was used as the curve fitting expression. The curve fitting package was Peakfit^{TM} (by Jandel) which utilizes a Marquardt-Levenberg algorithm to minimize the difference between the fitting expression and the experimental data. Eq. (3.34) can be used to analyze TSC data by absorbing all the parameters in the prefactor into an overall scaling factor, K.[e.g.[61]]. This, of course, requires the assumption that in this temperature range, $\mu\tau$ is constant. The fits to the high temperature peaks in the undoped BGO

sample and the Ga-doped BGO sample are shown in Figs. 4.5(a) and 4.5(b) and the parameters obtained from the fits are given in Table I.

The 280 K peak seen in the undoped sample appears to be a single peak with a limited amount of overlap on the low temperature side. A thermal cleaning cycle to 260 K was performed to eliminate the low temperature overlap. The resulting data is shown in Fig. 4.6. Halperin and Braner [62] defined the geometrical factor $\mu_g = \delta/\omega$ where $\delta = T_2 - T_m$ and $\omega = T_2 - T_1$. T_m is the temperature at which the TSC (or TL) peak maximum occurs and T_1 and T_2 are the low and high temperatures at which the signal is one half its maximum value, respectively. They showed that for a first-order peak $\mu_g = 0.42$ and for a second order peak $\mu_g = 0.52$. For the peak shown in Fig. 4.6 $\mu_g = 0.411$, which is very close to the value expected for a first-order peak. Since these data appear to show a single peak many additional methods of analysis can be used to determine trapping parameters.

One method used was Chen's peak shape method as described in Chapter 3 [50]. Using this method the three resulting activation energies for the 280 K peak in undoped BGO are $E_\omega = 0.99$ eV, $E_\tau = 0.95$ eV and $E_\delta = 1.03$ eV.

A second method of analysis is the initial-rise technique. It must be remembered that an approximation is made in that the preexponential factor is a constant only if the trap concentration remains approximately constant, so no data past the first 10% or 15% of the peak height should be used in the calculation. An initial rise plot from the data of Fig. 4.6 is shown in Fig. 4.7. Unfortunately, a straight line was not obtained. A possible reason for this is that the low temperature component may not have been completely eliminated during the preheating cycle. Nevertheless, an activation energy of 0.60 eV was calculated from the line shown in the figure.

The method of curve fitting using Eq. (3.34) was also tried. The three parameters used for fitting were the scaling factor K, activation energy E_t and frequency factor s.

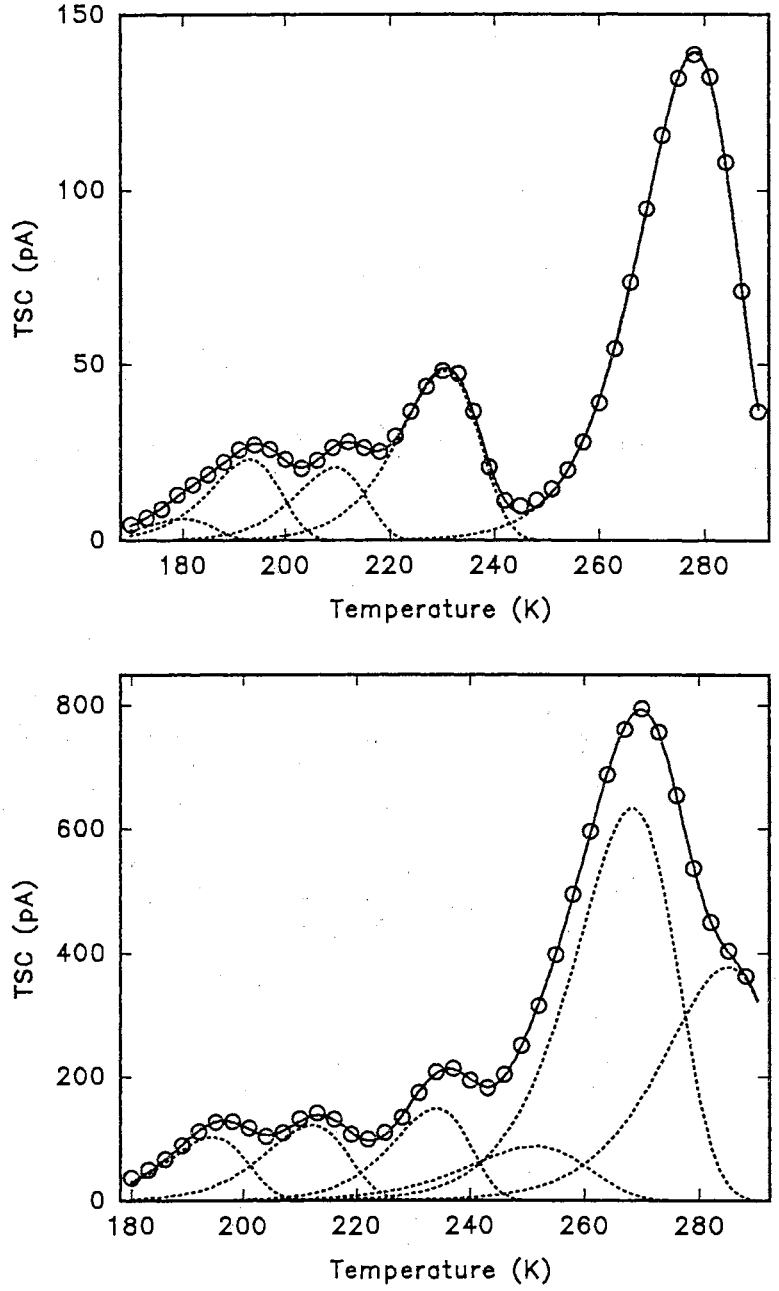

Figure 4.5: Fits to the high temperature peak in (a) undoped BGO and (b) Ga-doped BGO. ○ — experimental data; dashed lines — individual fitted components; full line — sum of dashed lines.

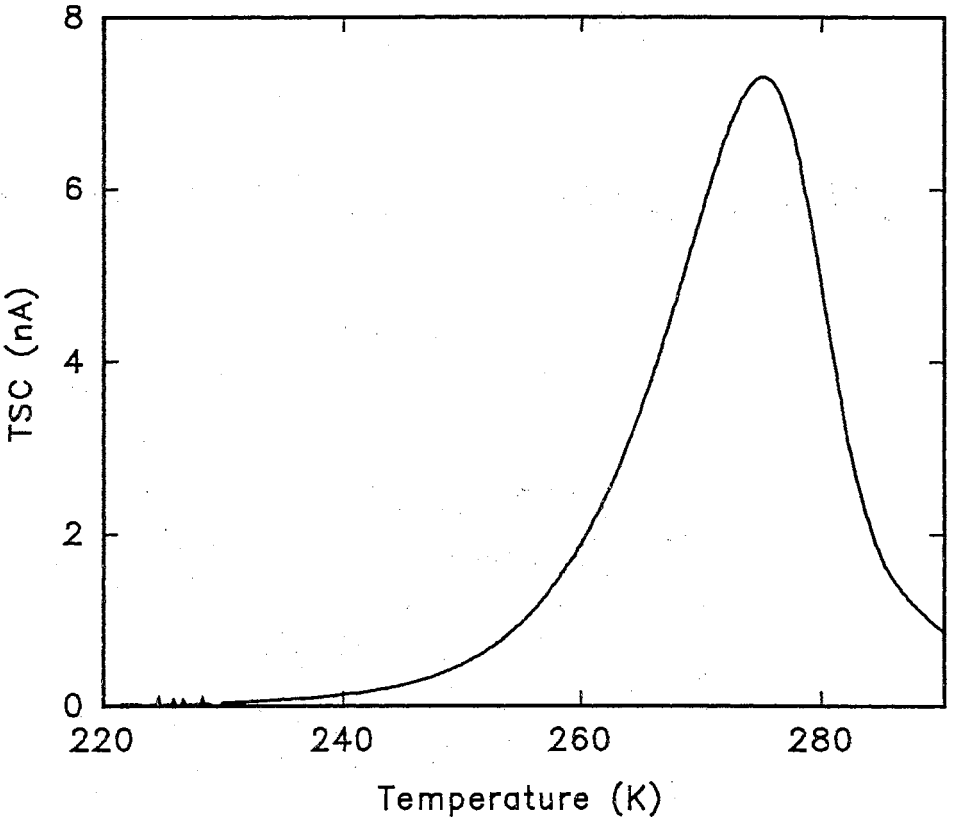

Figure 4.6: TSC spectra for undoped BGO measured after a preheating cycle to 260 K.

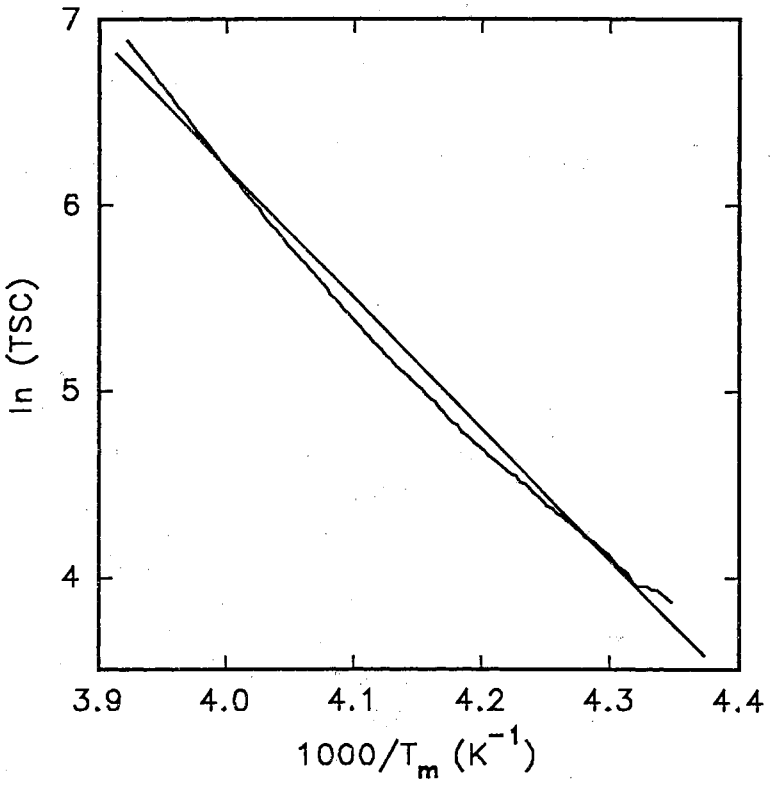

Figure 4.7: Initial rise plot for the data of Fig. 4.6. From the dashed line approximating the slope an activation energy of 0.60 eV was obtained.

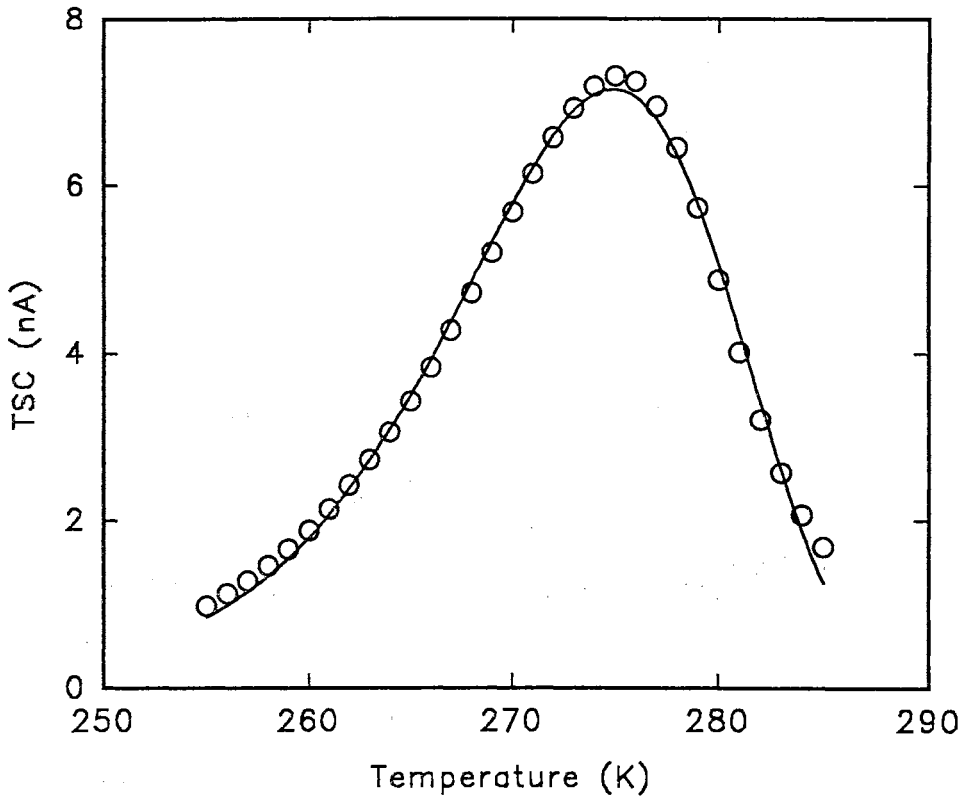

Figure 4.8: Fit to the data shown in Fig. 4.6 for undoped BGO. The resulting activation energy and frequency factor are 0.94 eV and $2.1 \times 10^{15} s^{-1}$, respectively.

The frequency factor was assumed to be temperature independent (i.e. b was set equal to 2). The fit is shown in Fig. 4.8. Deviations between the fit and the data may again be due to a portion of the low temperature component remaining, but the resulting activation energy is $E_t = 0.94$ eV and the frequency factor is $s = 2.1 \times 10^{15} s^{-1}$. It should be noted that the parameters obtained in the fit shown in Fig. 4.8 show a lot of variation from the parameters obtained for the 280 K peak in the fit shown in Fig. 4.5(a).

One last method used to find the frequency factor and activation energy was that of Hoogenstraaten. To apply this method several identical TSC experiments were performed using a 1 hour illumination at 412 nm with a -20 v bias applied to the sample during illumination and heating, but the heating rate was varied in

each experiment. No thermal cleaning cycles were performed in these experiments because the low temperature overlap with the 280 K peak is not significant enough to affect the peak position strongly. The heating rates used were 2, 3, 4, 5, 6, 8 and 10 K/min. The TSC curves are shown in Fig. 4.9(a) and a plot of $\ln(T_m^2/\beta)$ versus $1000/T_m$ is shown in Fig. 4.9(b). The slope of this line is E_t/k_b and the y-intercept is $\ln(E_t/sk_b)$. The resulting activation energy is 0.93 eV and the frequency factor obtained is $1.3 \times 10^{15} s^{-1}$.

Low Temperature Peak

Curve fitting the large peak below 160 K to the standard first- or second-order TSC expressions was unsuccessful. Even when using as many as six first-order peaks a poor fit was obtained. Using second-order peaks gave worse results. For this reason an attempt was made at deconvoluting the peak using the T_m-T_{stop} method described in Chapter 3.

Fig. 4.10(a) shows the results of the T_m-T_{stop} experiment performed on undoped BGO and Fig. 4.11(a) shows the results for Ga-doped BGO. The experiments were performed by illuminating with 412 nm light at 80 K for 1000 seconds and then heating at a rate of 3 K/min. The illumination time was short enough that the slowly growing component on the low temperature side of the large composite peak in the undoped BGO sample was kept small. To be noted is that no hidden peak structure was revealed by the gradual thermal cleaning of the peaks in either sample. Plots of T_m vs. T_{stop} are shown in Figs. 4.10(b) and 4.11(b). In these results there are no horizontal regions in the temperature range of the large TSC peak, but rather there is a gradual shift in peak position as the value of T_{stop} increases. This is indicative of either a composite peak that is made up of many closely spaced components, or of a peak that is characterized by a distribution of activation energies rather than a single,

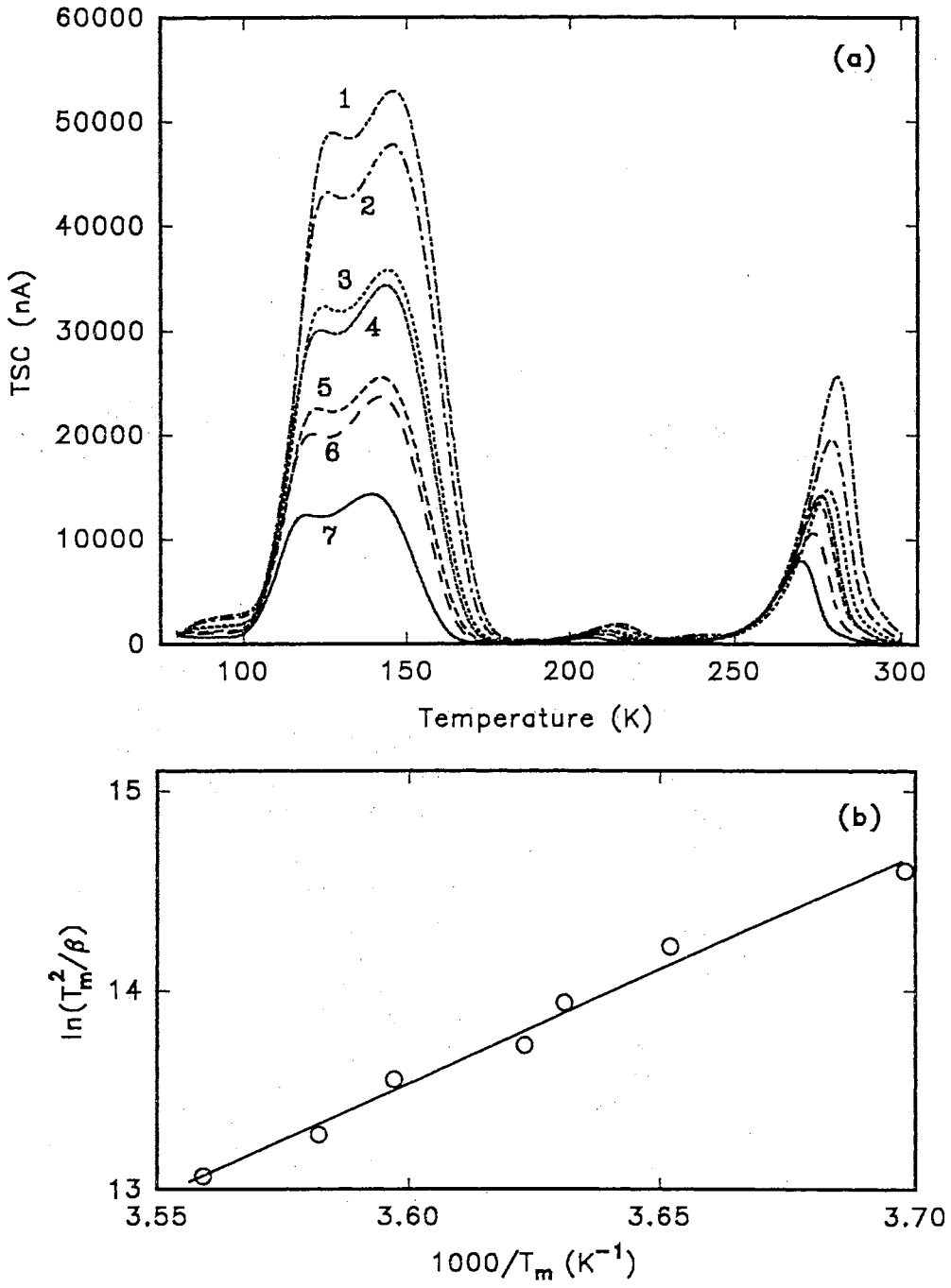

Figure 4.9: TSC spectra for undoped BGO measured with different heating rates. The TSC signal increases with the heating rate.

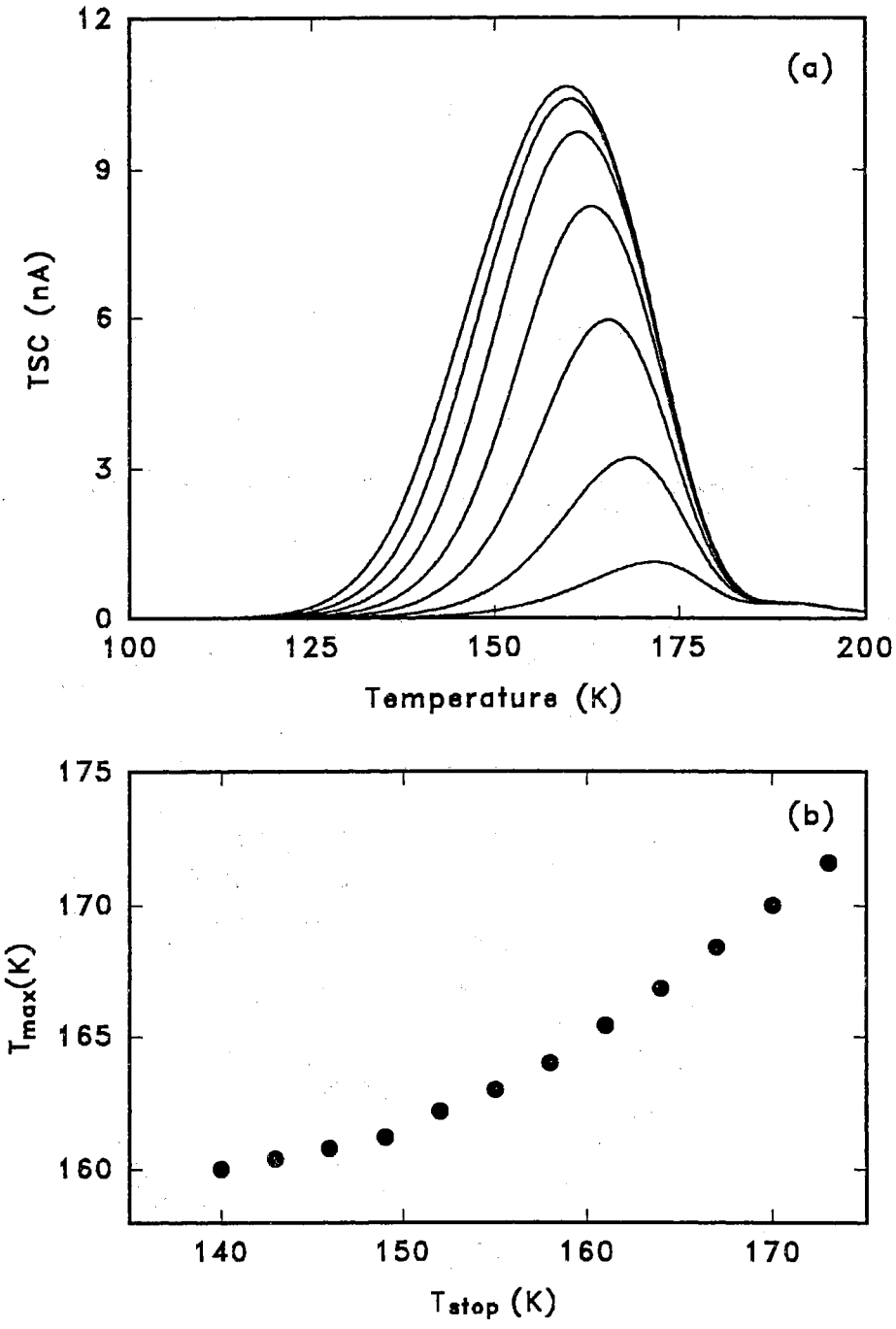

Figure 4.10: (a) Results of the T_m-T_{stop} experiment on undoped BGO. The T_{stop} values are 137, 143, 149, 155, 161, 167 and 173 K. (b) Plot of the position of the TSC maximum (T_m) vs. T_{stop}.

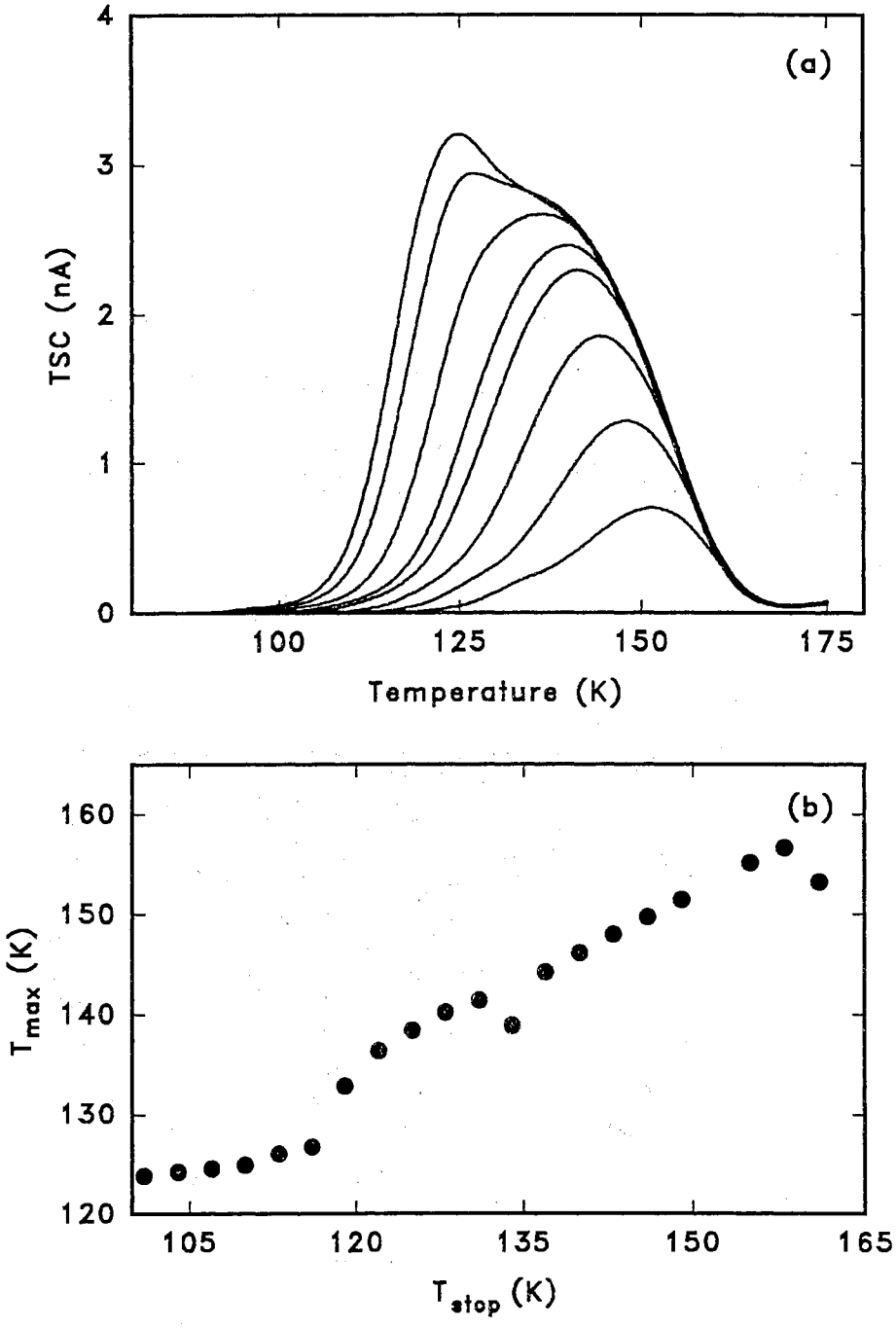

Figure 4.11: (a) Results of the T_m-T_{stop} experiment on Ga-doped BGO. The T_{stop} values are 110, 116, 122, 128, 131, 137, 143 and 149 K. (b) Plot of the position of the TSC maximum (T_m) vs. T_{stop}.

well-defined activation energy. Since an attempt to fit the data using multiple peaks was unsuccessful we proceeded with the assumption that the peak was caused by a trap with a distribution of energy states. The shape of the distribution is unknown, but the assumption of a rectangular distribution results in Eq. (3.30) which can be quickly evaluated using a computer, so we assumed a rectangular distribution.

Our preliminary attempts at fitting using this expression produced much better results, but some improvement was still needed because four peaks were required in fitting the data for the undoped sample. Four traps thermally unstable over the same temperature range, each with a distribution of activation energies, seemed to be an unlikely possibility, so it was decided to try to crudely account for the likely circumstance that the distribution shape was not rectangular. To do this the distribution was broken into three segments with each segment having its own amplitude. The three segments were constrained to be adjacent to each other in energy and they all shared the same width and frequency factor. The modified fitting expression is

$$
\begin{aligned}
I_{TSC}(T) \;=\; & \frac{skT}{\Delta E/3}\left[\frac{K_1}{\gamma_1}\left(\exp\left(-\gamma_1\exp\left(\frac{-E_0+\frac{1}{2}\frac{\Delta E}{3}}{kT}\right)\right)-\exp\left(-\gamma_1\exp\left(\frac{-E_0+\frac{3}{2}\frac{\Delta E}{3}}{kT}\right)\right)\right)\right. \\
& \frac{K_2}{\gamma_2}\left(\exp\left(-\gamma_2\exp\left(\frac{-E_0-\frac{1}{2}\frac{\Delta E}{3}}{kT}\right)\right)-\exp\left(-\gamma_2\exp\left(\frac{-E_0+\frac{1}{2}\frac{\Delta E}{3}}{kT}\right)\right)\right)+ \\
& \left.\frac{K_3}{\gamma_3}\left(\exp\left(-\gamma_3\exp\left(\frac{-E_0-\frac{3}{2}\frac{\Delta E}{3}}{kT}\right)\right)-\exp\left(-\gamma_3\exp\left(\frac{-E_0-\frac{1}{2}\frac{\Delta E}{3}}{kT}\right)\right)\right)\right]
\end{aligned}
$$

where

$$\gamma_1 \;=\; \frac{skT^2}{\beta\left(E_0-\Delta E/3\right)}\left(1-\frac{2kT}{E_0-\Delta E/3}\right), \tag{4.1}$$

$$\gamma_2 \;=\; \frac{skT^2}{\beta E_0}\left(1-\frac{2kT}{E_0}\right), \tag{4.2}$$

$$\gamma_3 \;=\; \frac{skT^2}{\beta\left(E_0+\Delta E/3\right)}\left(1-\frac{2kT}{E_0+\Delta E/3}\right). \tag{4.3}$$

In these expressions ΔE is the width of the entire distribution, so that $\Delta E/3$ is the width of each segment. The fitting parameters now become K_1, K_2, K_3, s, E_0 and ΔE where E_0 is the center of the central segment. The results of fitting using

this expression were much more impressive than any of the earlier results. Only one peak was needed to fit the data from Ga-doped BGO. Some example fits to the T_m-T_{stop} data files are shown in Figs. 4.12(a)-(c). Any small deviations between the fit and the experimental data can be understood in terms of the approximation made to the actual distribution shape. The fits obtained to the data for the undoped BGO sample required two peaks, but this was expected since the measurements to investigate the growth of the peaks with illumination time showed that there was both a fast and a slow growing component. Several example fits to data taken on the undoped BGO sample are shown in Fig. 4.13. The parameters obtained from these fits are summarized in Tables II and III.

Data for the growth of the TSC signal with illumination time for the undoped BGO sample was also fitted since in some of the data sets two peaks are clearly visible, although there is still substantial overlap. These data show an effect similar to the thermal cleaning performed in a T_m-T_{stop} experiment in that the relative size of the low temperature to the high temperature peak can be varied experimentally. Instead of using heating cycles to affect the trap occupancies, however, the illumination length controls trap populations. In these fits the activation energies and the width of the distributions should remain the same for each data set since the sample is not being preheated and therefore the low energy side of the distribution is not being preferentially emptied The main effect that should be observed in the fits to the data sets taken with longer illumination times is that both peaks should increase in size and the size of the low temperature component should increase relative to the high temperature component. Several of these fits are shown in Fig. 4.14 and the parameters obtained for this series of fits are given in Table IV.

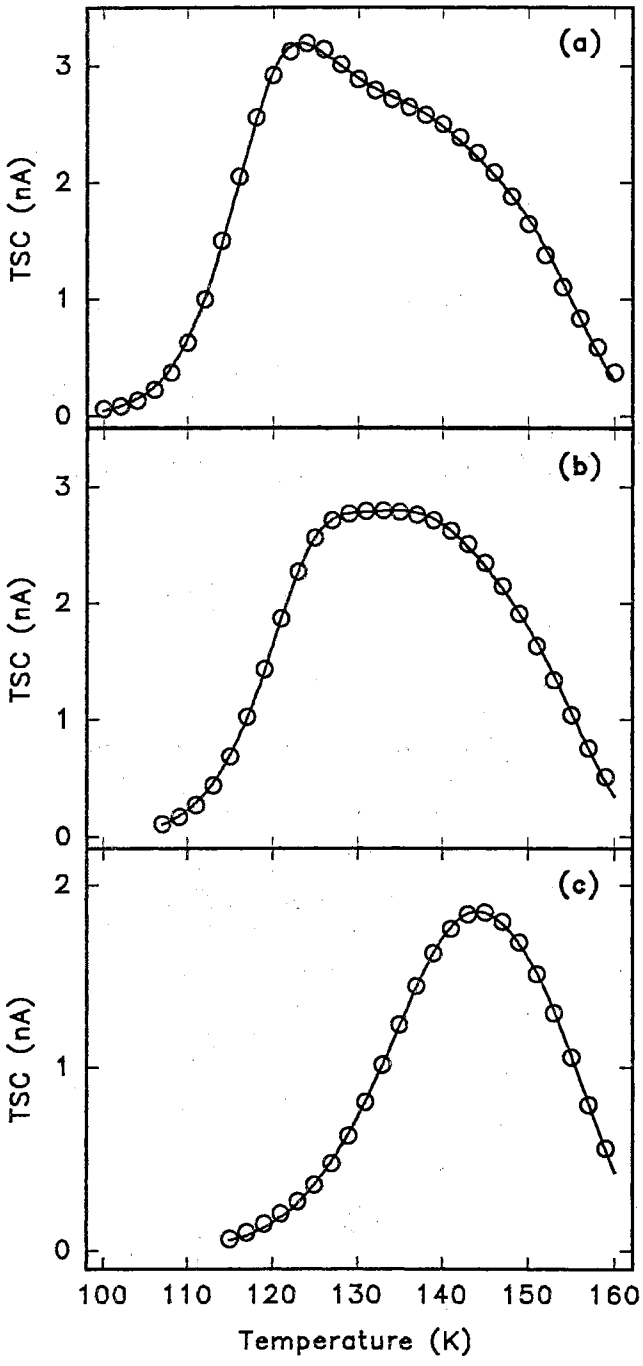

Figure 4.12: Fits to T_m-T_{stop} data of Ga-doped BGO. The T_{stop} values are: (a) 104 K, (b) 119 K and (c) 137 K.

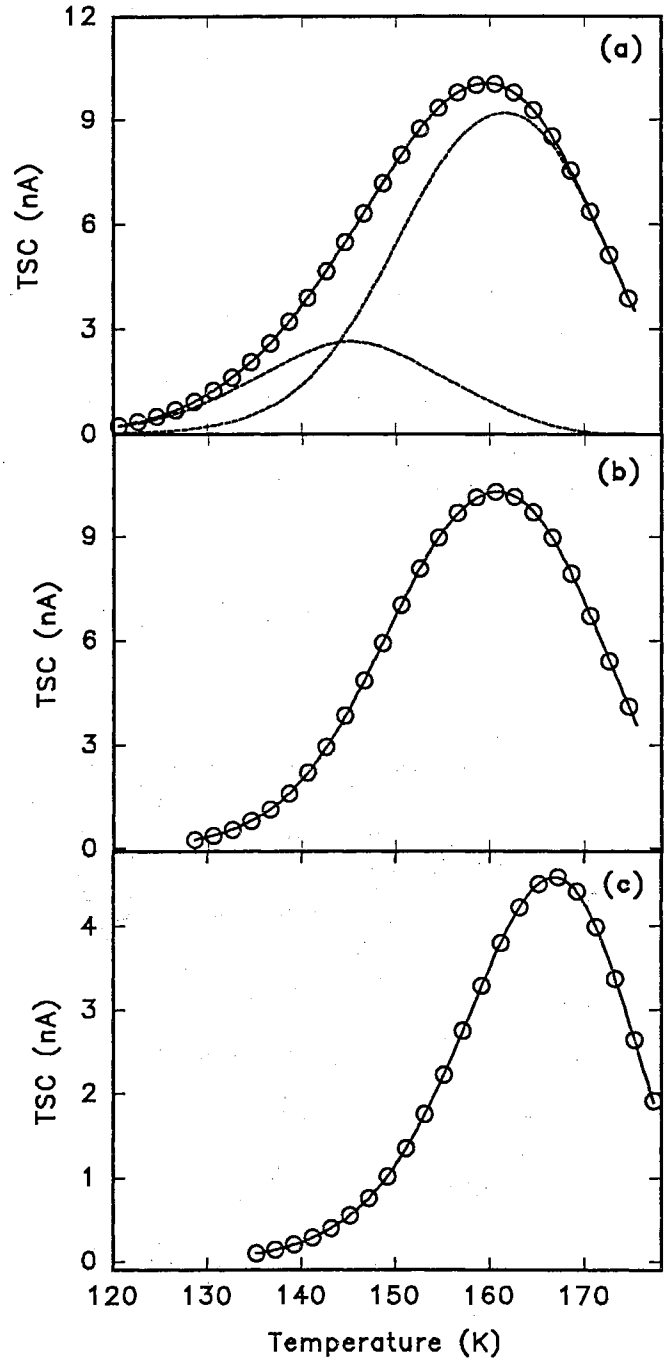

Figure 4.13: Fits to T_m-T_{stop} data of undoped BGO. The T_{stop} values are: (a) 122 K, (b) 146 K and (c) 164 K.

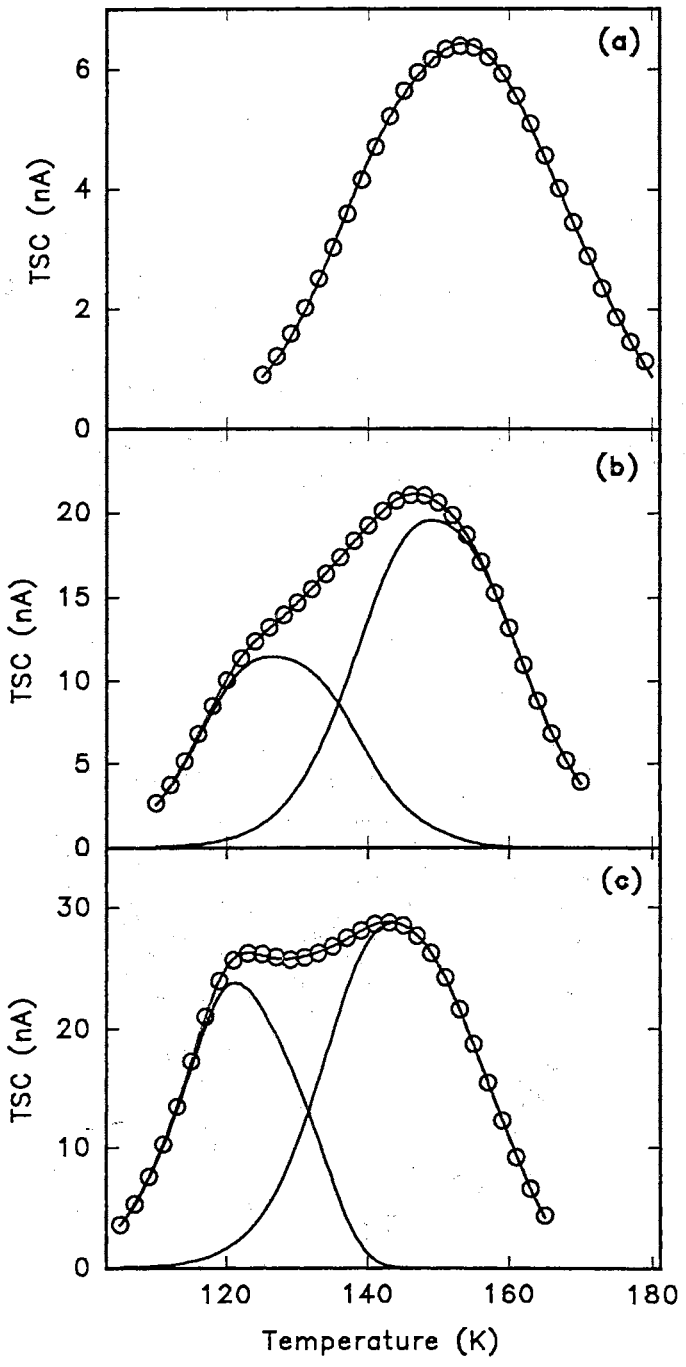

Figure 4.14: Fits to TSC data taken on undoped BGO with variable illumination lengths. The illumination lengths are: (a) 150 s, (b) 600 s and (c) 3600 s.

Isothermal Decay

To gain additional support for our contention that the low temperature peaks arise from a trap that is distributed in activation energy, the decay of the TSC signal as a function of time was measured at a constant temperature. Hornyak and Chen [57] showed that the decay of phosphorescence from a trap with a distribution of energy levels obeys a 1/t time dependence for a sufficiently wide distribution. They found that the important parameter in the determination of the time dependence was $y = kT/\Delta E$. For $y \geq 2.5$ the population of the trap decays nearly exponentially and for $y \leq 0.13$ the trap population decays with a 1/t dependence. For y between these two values the behavior is intermediate between exponential and 1/t. Monitoring the decay of the level at constant temperature then provides a rough measure as to the width of the energy distribution. We performed TSC decay measurements by cooling to 80 K and illuminating in the same way as for a TSC measurement. The sample was then heated and stabilized at a temperature corresponding to the large TSC peak and the decay of the conductivity was monitored for 1500 seconds. Fig. 4.15 shows the results of TSC decay measurements performed on 2% Ga-doped BGO at temperatures of 120 K and 140 K. The straight line shows the expected behavior if a 1/t decay is occurring. The decay we observed shows neither a 1/t or exponential dependence. According to the work of Hornyak and Chen the minimum distribution width that will display a decay with a 1/t time dependence at 140 K is $\Delta E \approx 0.09$ eV and the maximum distribution width that will decay exponentially is $\Delta E \approx 0.005$ eV. The distribution widths obtained from the results of curve fitting all fall within this range, so the decay of the TSC signal should follow neither an exponential nor 1/t dependence, consistent with what was observed.

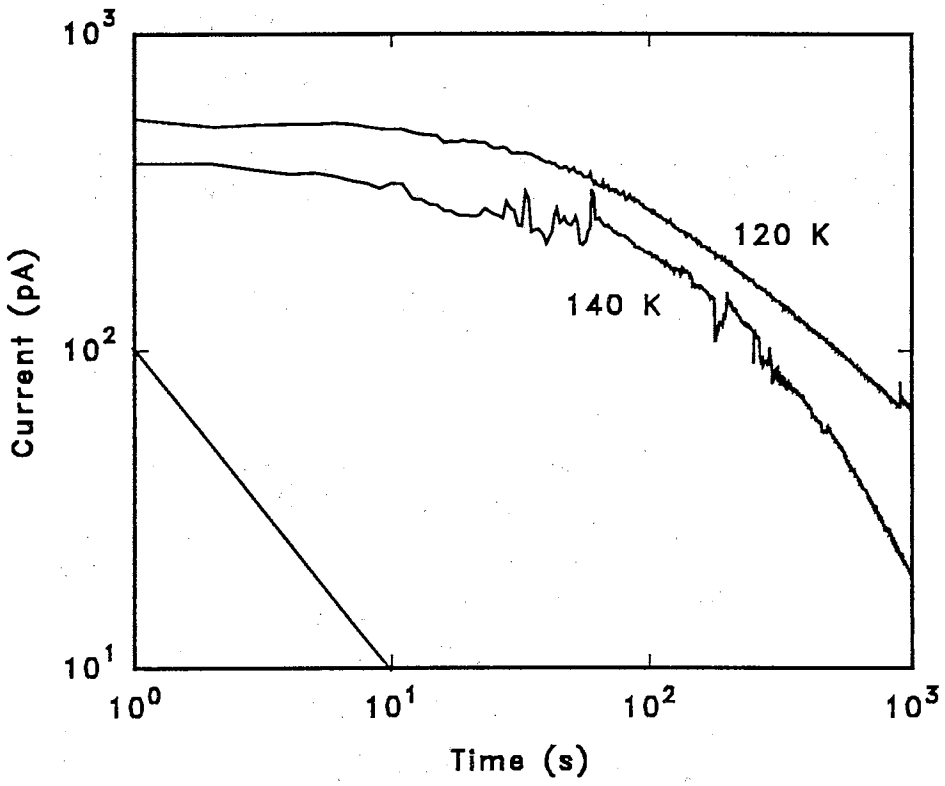

Figure 4.15: TSC decay of Ga-doped BGO at 120 K and 140 K. The dashed line illustrates a 1/t time dependence.

4.1.3 Calculation of Trap Concentrations

Trap concentrations were calculated using a method developed by Bube [63]. Following Bube the trap concentration, N_t, is given by

$$N_t = \frac{1}{eVG^*} \int J_{TSC} dt. \tag{4.4}$$

In this expression e is the electronic charge, V is the sample volume, J_{TSC} is the thermally stimulated current density, t is time and G^* is a scaling factor that approximates the gain. G^* accounts for the number of electrons measured in the external circuit per incident photon. G^* can be estimated by measuring the incident photon flux needed to produce a steady state current equal to the TSC maximum current at the temperature of the TSC maximum. G^* is then given by $G^* = J_{max}/qF$ where J_{max} is the maximum TSC current and F is the incident photon flux with dimensions of number of photons/unit time.

In our measurements we found, for example, that the TSC maximum current was $\sim$ 29 nA at a temperature of 143.4 K. The incident power needed to produce this steady state current at 143.4 K was 1.6 μW which corresponds to a photon flux of 3.3×10^{12} photons/s. Using this photon flux and from knowledge of the electrode area of 2.7 mm^2 the scaling factor G* was found to be 2.0×10^4 m^{-2}. The procedure then was to numerically integrate the TSC data to find the value of the integral for each peak and then use equation (4.4) to determine the trap concentrations. The calculated trap concentrations are shown in Table V for undoped BGO.

It was not possible to calculate trap concentrations for Ga-doped BGO because there were not enough electrons available at the donor level to saturate the traps, and thus the maximum TSC current could not be determined. Light of energy greater than the band gap could not be used because it was strongly absorbed at the surface and only the surface traps were filled.

4.2 Discussion of Results

The parameters obtained from the fits to the high temperature peaks shown in Figs. 4.5 (a) and 4.5 (b) in both types of sample are shown in Table I. The first peak in the TSC spectrum for the undoped BGO sample is centered at ~180 K and is most likely the remnant of one of the large low temperature peaks. It was pointed out earlier that the peaks at ~190 K, ~210 K and ~230 K are present in both samples. From the table it can be seen that the parameters for the 190 K peak (actually centered at 193 K and 194 K in undoped BGO and Ga-doped BGO, respectively) show good agreement between both fits. The frequency factors are 6.1×10^9 s^{-1} and 5.0×10^9 s^{-1} in undoped BGO and Ga-doped BGO, respectively, and the corresponding activation energies are 0.46 eV and 0.45 eV. The parameters obtained for the ~210 K peak show an order of magnitude variation in the frequency factor and 0.04 eV variation in the activation energy. In the undoped sample a frequency factor and activation energy of 2.3×10^{11} s^{-1} and 0.56 eV was obtained while in the Ga-doped sample the values are 2.0×10^{10} s^{-1} and 0.52 eV. The most variation between the two samples, however, is seen in the parameter values obtained for the 230 K peak. The fitting for undoped BGO gave $s = 5.2 \times 10^{10}$ s^{-1} and $E = 0.59$ eV and for Ga-doped BGO $s = 6.2 \times 10^{12}$ s^{-1} and $E = 0.68$ eV. It is interesting to note that the best agreement is obtained for the peak at lower temperatures and the agreement gets progressively worse towards higher temperature. This may be a consequence of the smaller amount of low temperature overlap of the 190 K peak as compared to the 210 K and 230 K peaks. The parameters obtained for the peak centered at 278 K and 285 K in undoped BGO and Ga-doped BGO, respectively, also show good agreement. Frequency factors of 5.4×10^{10} s^{-1} and 2.5×10^{10} s^{-1} and activation energies of 0.72 eV and 0.71 eV resulted for the undoped and Ga-doped samples.

The fit shows some deviation from the data around 245 K, so it is thought that

one more peak may be present, but since the peak appears to be so small and all other portions of the data set are fit well it was left out of the analysis. The analysis of the 280 K peak in undoped BGO described earlier also indicated that there may be a small peak in this temperature range. In the fit to the data for the Ga-doped sample a small peak in this temperature range was included as it was found that a good fit was impossible without it. The only remaining high temperature peak is centered at 268 K in the data for the Ga-doped sample and this appears to have no counterpart in the undoped sample. Parameters for this peak are given in Table 1.

From the results of fitting to the individual T_m-T_{stop} data the large low temperature peak in the Ga-doped sample is believed to originate from a single trapping level with activation energies distributed in a band of width ~0.085 eV centered around a value of 0.29 eV. The activation energies obtained vary from 0.29 eV for T_{stop} = 104 K, 110 K and 119 K, to 0.27 eV for T_{stop} = 137 K. To compensate for the decrease in the activation energy as T_{stop} increases the frequency factor also decreases by about an order of magnitude. The distribution width gets narrower from a value of 0.088 eV for T_{stop} = 104 K, to 0.060 eV for T_{stop} = 128 K and T_{stop} = 137 K. The narrowing of the distribution as T_{stop} increases is consistent with expectations. As T_{stop} is increased the lower energy side of the distribution is thermally depopulated to a greater extent than the high energy side which effectively decreases the distribution width and skews the population of the various energy levels towards the upper energy states. For this reason there should be an increase in the heights of the second and third segments relative to the first, as well as an increase in the height of the third segment relative to the second segment as T_{stop} increases. The ratios of the amplitudes of the segments are given in Table II. The ratios are defined in a way such that all three ratios should increase as T_{stop} increases. This is shown to be the case.

We were unable to obtain good fits to the data for T_{stop} values of 143 K and

higher due to the shoulder which begins to appear on the low temperature side of the peak. We believe that this shoulder, rather than being a separate peak, is a consequence of the density of states of the charge distribution. If the density of states has a minimum near the central energy, then for certain occupations of those states the TSC signal may exhibit a minimum or at least a concave upward region near the center of the peak. Thermally cleaning the peak may change the distribution shape as the electrons occupying the lower energy states of the distribution are more likely to be thermally excited from their traps and may even be retrapped into higher energy states of the distribution. These changes in distribution shape as T_{stop} is changed can lead to complex peak shapes such as those seen for values of $T_{stop} > 143$ K.

The results of the fitting to the T_m-T_{stop} data files for the undoped BGO sample are not as convincing as those for the Ga-doped BGO sample, since the presence of two peaks, instead of just one as for the Ga-doped sample, adds an extra complication. A problem with fitting two peaks to the data is that the measured TSC peak is so broad and featureless that the two peaks used in fitting may be able to take on a wide range of parameter values each of which may result in a good fit. Fitting with one peak was tried, but good fits were obtained only for the data files in which $T_{stop} > 140$ K as seen in Fig. 4.13. For TSC data measured after thermally cleaning to a temperature below 140 K two peaks were needed to accurately fit the data. Table III shows the parameters obtained in these fits. The relative amplitudes of each segment are shown by assigning the amplitude of the central segment the value 1.

The parameters obtained in the fits to the variable illumination data show more consistency than the parameters obtained from fitting the T_m-T_{stop} data. The low temperature component shows an order of magnitude of variation in the frequency factor, ranging from 1.5×10^7 to 5.5×10^8 s^{-1}, but the activation energy never varies more than 0.01 eV from a value of 0.25 eV. Also, the distribution width obtained in

each fit is 0.063 $\pm$ 0.03 eV. The high temperature component has a frequency factor ranging from 4.6×10^7 to 9.9×10^7 s^{-1} and an activation energy of 0.29 $\pm$ 0.01 eV. The width of the energy distribution shows more variation than was seen in the low temperature component, but is centered around a value of 0.06 eV.

4.3 Summary

The TSC signal in both undoped BGO and 2% Ga-doped BGO reveals a complex distribution of trapping centers. The analysis of the TSC signal shows that all peaks are first-order and that the low temperature peaks in undoped BGO and 2% Ga-doped BGO arise from trapping states that are characterized by a distribution of activation energies rather than single valued activation energies. The low temperature peak in undoped BGO is a composite consisting of two components centered at $\sim$0.24 eV and $\sim$0.29 eV with distribution widths of $\sim$0.065 eV. In 2% Ga-doped BGO the low temperature peak arises from a single trapping center at $\sim$0.29 eV with a distribution width of $\sim$0.085 eV. The TSC decay data support the contention that the centers responsible for the low temperature peaks have distribution widths $\Delta E < 0.09$ eV. Trapping parameters (activation energies, frequency factors and concentrations) for peaks present at higher temperature have been determined as well.

Chapter 5

Time-of-Flight Measurements

5.1 Introduction

The mobility is an important parameter of a photorefractive material since it determines the maximum speed at which a device made from the material can operate. Several measurements of mobility have been made in the sillenites [24,64,65], but the resulting values are spread over approximately 6 orders of magnitude. Values have been found from $\sim 5 \times 10^{-6}$ to ~ 3 cm^2/Vcm. This wide spread is probably due in part to impurity variations in crystals which were grown in different laboratories, but differing measuring techniques also play a role. Also, some researchers have found that the mobility can vary by 3 or 4 orders of magnitude in the same sample depending on the degree of filling of the traps [66].

The temperature dependence of the mobility can give important information about the defect states and the nature of charge transport in the material. Since a mobility measurement occurs over the same time scale as writing a grating both processes will be affected by the same trap species, so mobility measurements give pertinent information about those traps which most affect a great many photorefractive applications.

To measure mobility we performed time-of-flight (TOF) measurements on undoped and 0.3% Fe-doped BGO and undoped BSO grown by the Czochralski tech-

nique. This method has been used with success by other researchers to measure mobilities in amorphous materials [67-73], semiconductors [74,75] and insulators such as BGO and BSO [64]. We made our measurements between 200 K and 300 K. At temperatures below $\sim$ 200 K the signal became too weak to measure.

5.2 Theory

5.2.1 Background

A time-of-flight measurement is performed as follows. A thin sheet of free electrons and holes is generated near the top surface of the sample by a short, strongly absorbed pulse of light, typically from a pulsed laser or a flashlamp. By applying a voltage to the sample either electrons or holes are driven into the bulk of the material depending on the polarity of the applied voltage. As the carriers drift through the sample some may recombine while others may be trapped. Those carriers that are trapped in shallow levels can be thermally emitted back into the delocalized band and continue their drift through the sample. When the carriers reach the far electrode they recombine with carriers of the opposite sign at the contact. The charge induced in the external circuit by the movement of charge in the sample is given by Ramo's theorem [76],

$$\Delta Q = \frac{q\Delta d}{L} \tag{5.1}$$

where ΔQ is the charge induced in the external circuit, q is the charge moving through the sample, Δd is the distance the charge q moves and L is the sample thickness. The validity of this expression has been established experimentally in a number of materials. In the absence of any spreading mechanisms an infinitesimally thin sheet of carriers injected into the sample at $t = 0$ will produce a current transient like that

shown in Fig. 5.1. The mobility can be calculated using

$$\mu = \frac{L^2}{V t_T} \tag{5.2}$$

where V is the applied voltage and t_T is the transit time.

This idealized transient is not seen in practice for a number of reasons including the finite RC response time of the circuit, the finite length of the light pulse, variations in the electric field due to non-uniform space charge and due to the presence of the carrier packet itself, variations of the mobility with position in the crystal, variations in the defect structure and density in the crystal, trapping in the bulk, and recombination immediately after the laser pulse when there is a high concentration of free electrons and holes located in the same region of the sample near the surface. In order to get good results we must have $RC \ll t_T$ and the length of the light pulse must also be much shorter than the transit time. Also a large number of carriers must remain free of deep traps. It is often possible to vary the experimental parameters, so that these conditions are met. For example, the applied bias and sample thickness can be chosen to make the transit time short enough that not all the carriers are trapped in deep traps during the measurement. This also helps to limit the amount of recombination which can occur immediately after the pulse. The effect of recombination is to cause an immediate decay in the current after the initial rise. Trapping also causes a decay in the signal for $t < t_T$, but, in addition, it can cause the transient to exhibit a tail for $t > t_T$ if the traps are shallow enough to be thermally unstable on the time scale of the measurement. Variations in the field due to the presence of the drifting carriers can be minimized by using a laser pulse of low intensity.

We are interested in both the microscopic and drift mobilities. The microscopic mobility, μ_0, is the intrinsic mobility of the free carriers. In the case that trapping does take place, the carriers' mobility is still equal to the microscopic mobility between trapping events. The mobility we measure in a TOF experiment, however, is the drift

mobility which is the net mobility modified by trapping.

One method to account for the effect of trapping on the mobility was suggested by Bube [77]. Define a drift mobility, μ_d, such that the conductivity actually observed (caused by the total excited carrier concentration n_c+n_t where n_c is the concentration of carriers in the conduction band and n_t is the trapped carrier concentration) is equal to the conductivity which would be observed if we had only n_c free carriers traveling through the sample with the mobility μ_0. Namely,

$$(n_c + n_t)\mu_d = n_c\mu_0. \tag{5.3}$$

Solving for μ_d gives

$$\mu_d = \frac{n_c}{n_c + n_t}\mu_0. \tag{5.4}$$

If the injected carrier concentration is small enough that the concentrations are not displaced much from their thermal equilibrium values then the trapped and free carrier concentrations must obey

$$\frac{n_t}{n_c} = \frac{N_t}{N_c}\exp\left(\frac{E_t}{k_bT}\right) \tag{5.5}$$

where N_t is the trap concentration, N_c is the effective density of states in the conduction band, E_t is the activation energy of the trap, k_b is Boltzmann's constant and T is temperature. Substituting this expression into Eq. (5.4) gives

$$\mu_d = \mu_0\left[1 + \frac{N_t}{N_c}\exp\left(\frac{E_t}{k_bT}\right)\right]^{-1}. \tag{5.6}$$

Eq. (5.6) shows that at high temperature where detrapping is very fast and $n_t \approx 0$, $\mu_d \approx \mu_0$ as expected. At low temperature the second term in the denominator dominates and we get

$$\mu_d \approx \mu_0\frac{N_c}{N_t}\exp\left(-\frac{E_t}{k_bT}\right). \tag{5.7}$$

5.2.2 Transient shape

The shape of the transient depends on the nature of the carrier transport. Two types of transport are possible: 1) drift of carriers through one of the delocalized bands, possibly interacting with traps, and 2) hopping transport where carriers move through the sample by hopping from site to site. Hopping transport has been seen in amorphous materials such as a-As_2Se_3 [67] and a-Si [68]. These two mechanisms result in differently shaped transients and different behavior of the carriers as a function of applied voltage and sample thickness.

According to Scher and Montroll [67] carrier transport in amorphous materials is characterized by the "universality" of the current transients when normalized to the transit time. It was found that the shape of the current transients in many amorphous materials is independent of applied voltage and sample thickness. This "universality" of the current pulses led Scher and Montroll to conclude that an unusual statistical process was taking place. They assumed that the solid consists of a lattice of identical cells and that each cell contains a number of randomly distributed sites which carriers can occupy. A carrier moves by hopping from site to site in a cell, eventually leaving one cell and entering an adjacent cell. The sites are assumed to have a broad distribution of hopping times from times much shorter than the transit time to times at least comparable to the transit time. They find that the distribution of release times for the different sites results in an increasing number of the carriers being delayed by a long hop as the packet travels through the sample, so that only a minority of the carriers reach the far contact without experiencing a long hop. This causes the packet of carriers to spread to a width comparable to the sample thickness, so that the majority of carriers are still near the front surface when the fastest carriers reach the far electrode. Scher and Montroll account for the disorder of the material through a disorder parameter, α. They found that for $t < t_T$ the transient decays

according to $t^{-(1-\alpha)}$ and for $t > t_T$ the decay follows $t^{-(1+\alpha)}$. On a log-log plot the two regions are readily visible. The transit time is obtained by the intersection of these two slopes. A prediction made by the model is that the mobility is a decreasing function of time. This is due to the accumulation of carriers at sites with long hopping times as the packet travels through the sample. Since the mobility is a decreasing function of time the transit time does not depend linearly on sample thickness or inverse applied voltage. The pulses exhibit the feature of "universality" because the ratio of the packet width, σ, to the mean carrier position is independent of time.

As explained by Scher and Montroll, if the carriers drift through a delocalized band interacting with a trapping level characterized by a single release time the carrier packet becomes Gaussian after the carriers have undergone a sufficient number of trapping and detrapping events. This prediction follows from the central limit theorem of probability. In contrast to the transport in amorphous materials where the velocity of the center of the packet is a decreasing function of time the center of a Gaussian packet moves at a constant velocity since no carriers are held up in traps with a long release time. In this case the transit time is inversely proportional to the applied voltage. Also, these transients do not exhibit the feature of universality since the ratio of the packet width to the position of the packet center decreases with time as $t^{-1/2}$.

A computational method for analyzing TOF transients was presented by Scott et al. [78]. Using this method both the average drift mobility and the width of the carrier packet can be extracted from the current transient. Scott defined $s(t)$ to be the current where t is the time since the laser pulse. Let $s_0(t)$ be the current which would be observed in an infinitely thick sample. The functional form of $s_0(t)$ must account for recombination immediately after the laser pulse, trapping, detrapping and other dispersive processes. To account for the sample surface (i.e. the rear surface) we need

to subtract from s_0 a term which describes the probability of a carrier arriving at the far electrode at any given time, namely,

$$s(t) = s_0(t)\left[1 - \int_0^t p_t(t')dt'\right]. \tag{5.8}$$

$p_t(t)$ is the distribution of arrival times and is related to the distribution of effective velocities, p_v, by

$$p_v(L/t) = \frac{t^2}{L} p_t(t). \tag{5.9}$$

This can be shown by equating the probability that a carrier arrives at the far contact in a time between t and $t + dt$ to the probability that a carrier travels with a velocity between v and $v + dv$ where $v = L/t$.

After determining p_v the average drift mobility, $\bar{\mu}_d$, can be calculated using

$$\bar{\mu}_d = \frac{\bar{v}}{E} = \frac{1}{E}\int_{-\infty}^{\infty} v p_v(v) dv \tag{5.10}$$

where E is the applied field. The task, now, is to find forms for $s_0(t)$ and $p_t(t)$ which account for the physical processes and thereby describe the data. Scott et al. chose the Scher and Montroll [67] form for $s_0(t)$ for the analysis of current transients measured in amorphous materials.

$$s_0(t) = At^{-(1-\alpha)} \quad 0 < \alpha < 1 \tag{5.11}$$

We found that this function did not fit our data well, however. For reasons that will be explained later we chose a stretched exponential function instead.

For $p_v(L/t)$ Scott et al. chose a Gaussian distribution. By differentiating their data they were able to find that the actual distribution of velocities was indeed Gaussian. A Gaussian distribution can arise if the carriers undergo multiple trapping and detrapping events during their transit through the sample. Using these expressions good fits were obtained to current transients measured in several materials [78].

The temperature dependence of the width of the Gaussian velocity distribution can be estimated in the following way. The transit time for an electron is $t_T = L^2/\mu_0 V + \sum_i t_i$ where μ_0 is the microscopic mobility, V is the applied voltage and t_i is the time spent trapped during the ith trapping event. The first term accounts for the time spent in the conduction band from the time of generation near the illuminated electrode until it reaches the back contact and the second term accounts for the time spent in traps. Another way to write the second term is nt_{av} where n is the number of times the carrier is trapped and t_{av} is the average time the carrier spends in each trap. n and t_{av} will vary among the different carriers in the packet. It will be shown later that the microscopic mobility is much greater than the drift mobility in our samples, so most of the time the electrons spend in transit must be spent in traps. Since the majority of the transit time is spent trapped we believe that the dispersion of the carrier packet as it drifts through the sample is due primarily to the variation in the number of trapping events and in the trap release times for the different carriers. Of these two the trap release times should have the stronger temperature dependence. The average number of trapping events depends on parameters such as the capture cross-section of the traps and the number of traps present, but the concentration of traps is independent of temperature and the capture cross-section can be expected to have a weaker temperature dependence than the exponential dependence of the detrapping time, so the temperature dependence of the width of the velocity distribution should be primarily due to the detrapping of carriers. The distribution of trap release times is

$$p_r = \frac{1}{\tau} \exp\left(\frac{-t}{\tau}\right) \tag{5.12}$$

where p_r is the probability per unit time of a carrier being detrapped and $\tau = s^{-1} \exp(E_t/k_b T)$. The dispersion in the detrapping times can be estimated by calcu-

lating the standard deviation, σ. For the distribution given by Eq. (5.12)

$$\sigma = \tau = s^{-1} \exp\left(\frac{E_t}{k_b T}\right). \tag{5.13}$$

Therefore, we should expect an approximately exponential dependence of the width of the velocity distribution on temperature.

5.3 Experimental Details

Our measurements were performed on BGO and BSO crystals grown by the Czochralski method in the Oklahoma State University Crystal Growth Lab. Measurements were performed on both undoped crystals and crystals doped with iron. Electrical contact was made by evaporating gold or aluminum electrodes onto the surface of the samples. The back electrode was thick, but the front electrode was made semi-transparent, so that the laser could excite the sample through the electrode. By measuring the absorption spectrum of the thin electrode with a Cary 5 spectrophotometer we determined that the thin electrode has a transmission of approximately 50% at the wavelengths of interest. The samples were mounted in an Oxford Instruments CF1204 dynamic flow cryostat.

The experimental setup is shown in Fig. 5.2. The current transients were recorded by measuring the voltage across a resistor (typically $\sim$ 50 kΩ) placed in series with the sample and using the 1 MΩ input on a LeCroy Model 9400A oscilloscope. An Oxford Instruments ITC4 temperature controller was used to control the temperature. The light pulses were provided by a Molectron Model UV14 nitrogen laser which generates 10 ns pulses at 337 nm. Light of this wavelength is energetic enough to cause band-to-band transitions in BGO and BSO and therefore is strongly absorbed near the surface of the sample. All data shown in this paper have been obtained with Al electrodes.

The experiments were performed by first cooling the sample to a temperature

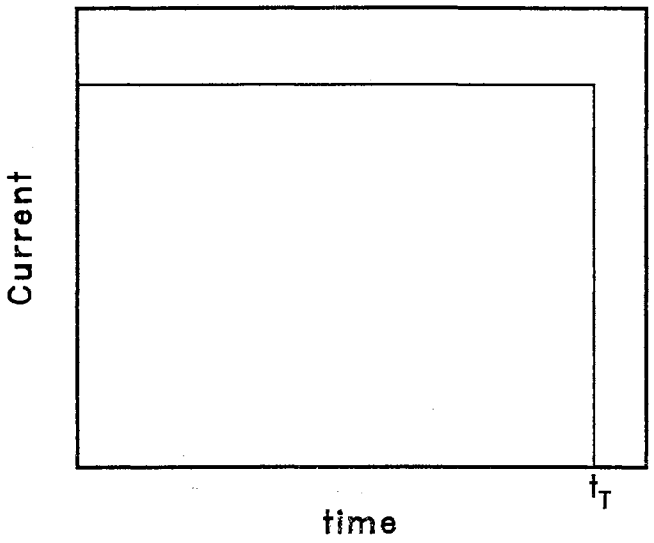

Figure 5.1: Ideal TOF transient obtained in the absence of trapping and recombination.

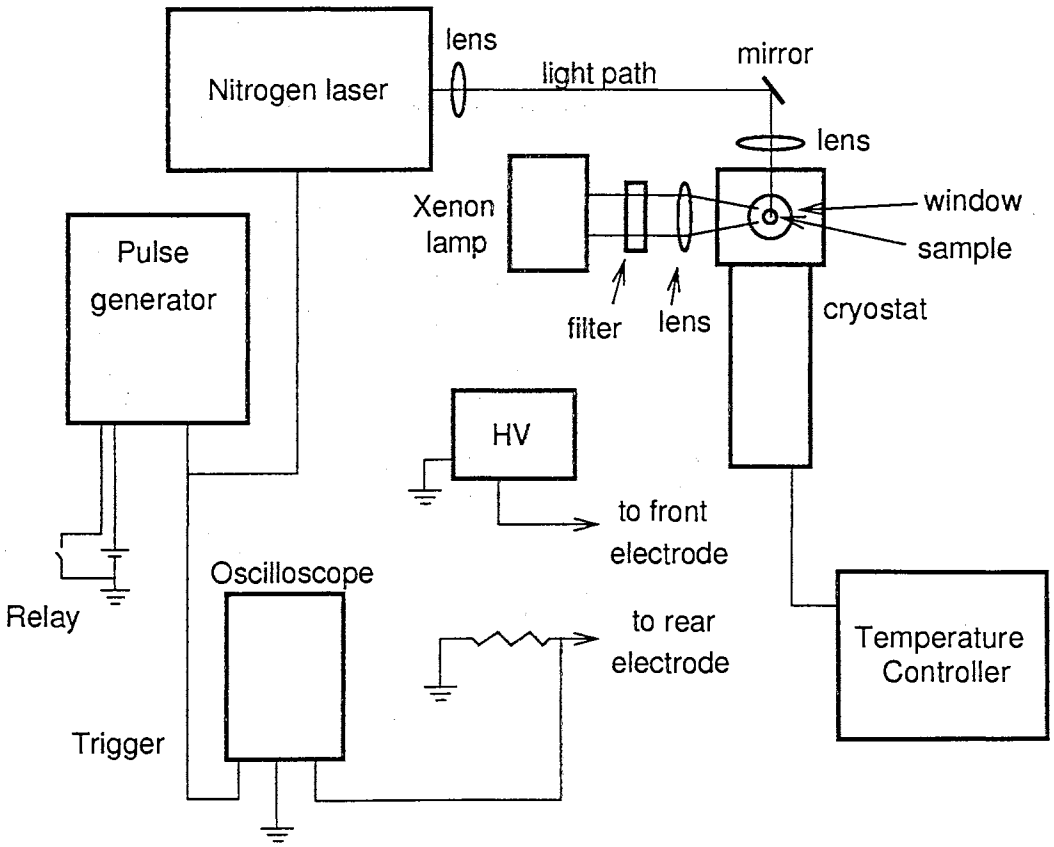

Figure 5.2: Experimental setup for time-of-flight experiments.

between 200 K and 300 K. The high voltage was applied to the sample and then the laser was pulsed, and the resulting current transient recorded on the oscilloscope. Immediately after the measurement the high voltage was removed from the sample. Before the next measurement the same high voltage, but with opposite polarity, was applied to the sample for about 1 s to help reduce the accumulation of space charge. In most of the measurements the laser beam was attenuated with a neutral density filter to an energy of $\sim$ 0.2 μJ per pulse, also to help reduce space charge accumulation. Measurements were performed both with the sample in the dark, and with the sample illuminated with a constant background illumination. The background light was provided by a 1000 W Xenon lamp with the output filtered by interference filters or passed through a monochromator to limit the incident light to the blue part of the spectrum. According to Ennouri et al. [64] background illumination reduces the accumulation of space-charge in the bulk of the sample. We found, however, that background illumination was unnecessary. The measurements performed in the dark gave very reproducible results while data measured with background illumination were more erratic and less reproducible. Measurements were taken at each temperature with applied voltages from -100 V to -1000 V, so that electrons were driven through the sample. Some measurements were also taken with positive biases, but the resulting current transients were much weaker and were featureless. Thus, it was not possible to measure transit times for holes.

5.4 Results

5.4.1 General description of the transients

Typical transients obtained in undoped BGO are shown in Fig. 5.3. These transients were recorded at the temperatures indicated using an applied field of $\sim$ 7300 V/cm

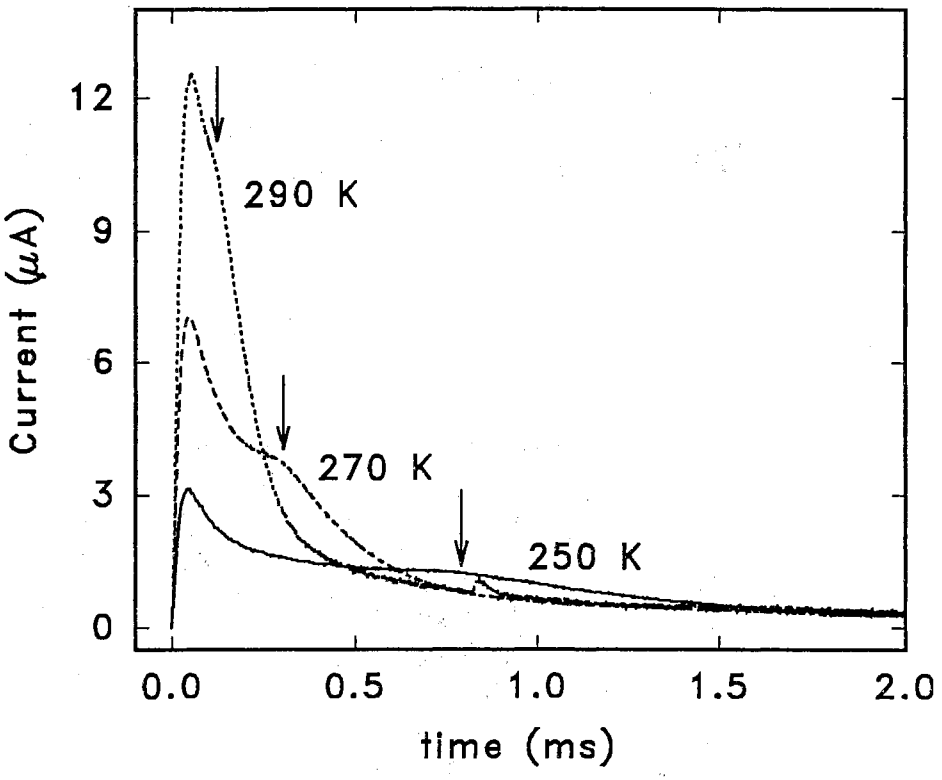

Figure 5.3: Typical electron current transients measured in undoped BGO at the indicated temperatures.

and no background illumination. The transit times of the fastest carriers are indicated by the arrows in the figure. At the time of the laser pulse there is a sudden rise in the current followed by a fast decay which becomes more gradual as time goes on for $t < t_T$. The rise time is independent of temperature, but does vary with the applied field; as the field is increased the rise time increases. The initial fast decay is believed to be due to recombination of free electrons and holes which are both present in high concentration near the surface of the sample immediately after the laser pulse, although trapping of carriers into defect states associated with the surface may also play a part. The interpretation of recombination of carriers is supported by our data which show a greater initial decay at lower applied fields (as will be shown later). This is consistent since in these circumstances the free electrons and holes spend more time near each other for lower applied fields. Once the holes are swept to the front contact and the electrons have been pushed into the bulk the recombination rate approaches zero and the rest of the decay becomes dominated by trapping. From the results of TSC measurements which were presented in Chapter 5 it is known that there are many traps present in these samples, distributed over a range of energies. We take the time of the break in the current (indicated by the arrows in Fig. 5.3) to be the transit time of the fastest carriers. If the transients are really due to a packet of electrons traveling through the sample and recombining at the back electrode the average transit time should depend linearly on 1/V, as required by Eq. (5.2). This dependence is shown on a log-log plot in Fig. 5.4. The straight lines have slope -1 and it can be seen that the data follow these lines fairly well. This result shows that the statistical process described by Scher and Montroll [67], which results in the average carrier velocity being a decreasing function of time, is not occurring here.

Additional support that we are actually measuring the drift of electrons through the bulk of the sample comes from the thickness dependence of the mobility. We

performed measurements on 0.3% Fe-doped BGO at the three thicknesses, 1.1, 0.4 and 0.25 mm. The values we obtained at 290 K were 0.011 cm^2/Vs for the 1.1 and 0.25 mm thicknesses and 0.010 cm^2/Vs at the 0.4 mm thickness showing that the drift mobility is independent of sample thickness.

The tail of the transient which is present for $t > t_T$ is due to the finite width of the carrier packet when it reaches the back electrode. Fig. 5.5 shows how the transients vary with applied field at 270 K in the 0.3% Fe-doped BGO sample. These transients were measured with no background illumination and a laser pulse energy of ~ 0.2 μJ. A kink is visible for the higher applied fields, but is much less well defined at lower fields. The pronounced cusp which is present in Fig. 5.5(a) is often seen for the higher applied fields. This effect has been seen by other authors as well [67,68]. For the lower applied fields the current reaches an essentially constant value for times shorter than the transit time, as defined by the "break". This is an indication that either no trapping is taking place or that the rate of trapping is equal to the rate of detrapping. If trapping was still dominating the signal should still be decreasing.

Fig. 5.3 shows how the transients vary with temperature. Near room temperature the transit time is very short and the kink is nearly hidden in undoped BGO. As the temperature decreases the transients become weaker and the transit times become longer. Since the transients become weaker at lower temperatures we were unable to obtain good results below about 200 K in undoped BGO and below about 230 K in both Fe-doped BGO and undoped BSO.

5.4.2 Analysis of transient shape

We fit the current transients using Eq. (5.8). For $s_0(t)$ we initially tried an exponential function, but we were unable to obtain a good fit to the initial part of the pulse.

Instead, we chose a stretched exponential function,

$$s_0(t) = A\exp(-t/\tau)^{\beta} + c, \tag{5.14}$$

where $0 \leq \beta < 1$ and c is a constant. The stretched exponential can be used to approximate a sum of exponential processes. Here it accounts for the recombination of free electrons and holes immediately after the laser pulse as well as the interaction of the electrons in the carrier packet with one or more trapping states during the propagation of the carrier packet through the sample. The constant c is needed because the current sometimes approaches a steady-state value for times shorter than the transit time as shown in Fig. 5.5. For the distribution of effective velocities we followed Scott et al. [78] and chose a Gaussian distribution,

$$p_v = \frac{1}{\sigma_v\sqrt{2\pi}}\exp\left[\frac{-(v-v_0)^2}{2\sigma_v^2}\right]. \tag{5.15}$$

In Eq. (5.15) σ_v is the standard deviation of the carrier velocities and v_0 is the mean carrier velocity. The distribution of arrival times can be found using Eq. (5.9). Substituting the resulting arrival time distribution and Eq. (5.14) into Eq. (5.8) gives the fitting expression,

$$s(t) = \left[A\exp\left(-(t/\tau)^{\beta}\right) + c\right]\left[1 - \int_0^t \frac{1}{\sigma_I t'^2\sqrt{2\pi}}\exp\left(\frac{-(1/t' - 1/t_0)^2}{2\sigma_I^2}\right)dt'\right] \tag{5.16}$$

which we use to fit the current transients. The fitting parameters are A, τ, β, c, σ_I and t_0. τ and β account for the processes of recombination and trapping. The constant c accounts for the concentration of carriers occupying the conduction band during the transit of the carrier packet. σ_I is the standard deviation of the inverse arrival times and is related to the width of the velocity distribution by $\sigma_I = \sigma_v/L$. σ_I reflects the spread of the carrier packet caused by dispersive processes such as trapping and detrapping. Lastly, $t_0 = L/\bar{v}$ is the mean transit time of the carriers.

We fit data measured in undoped and 0.3% Fe-doped BGO and undoped BSO using this expression. The fitting algorithm used was the Levenberg-Marquardt method

[79]. Some typical fits to the TOF transients measured at 250 K in the undoped BGO sample are shown in Fig. 5.6 and illustrative fits to data from the 0.3% Fe-doped sample are shown in Fig. 5.7. The applied field used during each experiment is given in the caption. The fitting expression fits well over the entire time range of the transient for all samples except in some cases over the very early portion of the transient. The arrows in the figures indicate the mean transit time, t_0. In all cases the mean transit time is well past the kink which is interpreted as the transit time of the fastest carriers. We believe that defining the transit time as the average time of transit for all the carriers is a better definition than defining the transit time from the small number which travel fastest.

We note that if the data did not show a shoulder when the fastest carriers reached the far electrode there was a range of parameters which gave good fits. The parameters t_0 and σ_I were able to vary by up to a factor of ~ 2 while still providing a close fit to the data. This, of course, affects the value obtained for the average drift mobility as well. When a kink is visible, however, t_0 and σ_I take on well determined values. Fortunately this is the case for most of our data measured with applied fields of greater than 2000 V/cm.

It was found, also, that the parameters A, τ and β could assume two distinct sets of values for any fit. For one of the combinations A was larger and τ and β were smaller than in the other combination. The variations were roughly an order of magnitude for A and τ and about a factor of 1.5 to 2 for β. This problem may be due to the stretched exponential being a poor approximation to the processes of recombination, trapping and detrapping during the early part of the current transient. For this reason interpretation of values obtained for A, τ and β is difficult. There is almost certainly a much more complicated functional dependence, but the stretched exponential provides a reasonable approximation which can be used for curve fitting.

Despite these problems we believe that fitting the transients using Eq. (5.16) is useful since it allows us to determine the value of the average mobility and to get an estimate of the width of the carrier packet from any current transient which shows a break in the current when the fastest carriers reach the far contact. As mentioned above this condition is met by nearly all of the current transients measured with applied fields of at least 2000 V/cm in our samples. For determination of the average mobility and packet width an accurate fit to the tail of the current transient is all that is required. The parameters t_0 and σ_I are independent of the initial current decay.

Fig. 5.8 shows the velocity distribution calculated from the parameters obtained from the fits shown in Fig. 5.6. The cutoff on the low velocity side of the distributions indicate the carriers that traveled with average velocities so low that they didn't reach the far electrode during the measurement. As expected the center of the distribution moves to higher velocities as the applied field is increased. It can be seen, also, that the packet width is larger for higher applied fields rather than shifting uniformly to higher velocities, i.e. the slow carriers are relatively unaffected by the applied field. We believe this happens because the carriers on the low velocity side of the distribution spend a larger fraction of their transit time localized in one or more traps. Since the time spent accelerated by the applied field is small compared to the time spent in traps these carriers won't have a substantially higher effective velocity for higher applied fields.

The temperature dependence of the width of the velocity distribution, σ_v, is shown in Fig. 5.9(a) for the results of fitting to the undoped BGO sample for applied fields of 7270 and 3640 V/cm. Fig. 5.9(b) shows the results for 0.3% Fe-doped BGO. We have similar data for applied fields of 5450 and 1820 V/cm, but they are not shown for the sake of clarity. The data for the 3640 V/cm applied field show some deviation on both the low and high temperature sides, but 6 of the points do form a straight line. From

the slope of the lines we obtain activation energies of 0.36, 0.34, 0.34 and 0.31 eV for applied fields of 7270, 5450, 3640 and 1820 V/cm, respectively for undoped BGO. For the Fe-doped BGO sample the activation energies for the same applied fields were 0.35, 0.32, 0.33 and 0.37 eV, respectively. The results for undoped BSO showed less consistency than for the BGO samples. This may have been a consequence of the shoulder at the initial current break being less well defined in BSO.

5.4.3 Determination of Mobility

The drift mobility can be calculated using Eq. (5.10) once the values of the fitting parameters have been determined or, since we assumed a Gaussian distribution of velocities, the drift mobility can be calculated more directly by substituting the mean transit time, t_0, into Eq. (5.2). Voltage independent mobilities were found at all temperatures and in all samples and are listed in Table 5.1. The temperature dependence of the mobility in all three types of sample is shown in Fig. 5.10. The temperature dependence is nearly exponential in all cases. This dependence is too strong to be caused by the temperature dependence of a scattering process, so we assume it is due to trapping. Using Eq. (5.6) we can determine the activation energy of the trap from which carriers are being excited during the measurement. Using linear regression we find $E_t = 0.31$ eV for undoped BGO, $E_t = 0.34$ eV for Fe-doped BGO and $E_t = 0.31$ eV for the undoped BSO sample.

A close inspection of Fig. 5.10 shows that the data are not perfectly straight, but have a slight curvature. We believe that the curvature is due to the active trap being distributed in activation energy rather than having a discrete activation energy. In addition there may be more than one trap species trapping and detrapping carriers during the measurement. From the results of TSC measurements performed on undoped BGO we know that there are many traps present, with a major trap being

distributed in activation energy centered at $\sim$ 0.29 eV with a distribution width of $\sim$ 0.06 eV [80].

We can obtain an estimate for the microscopic mobility, μ_0, by using Eq. (5.7). In Chapter 4 a concentration of 3×10^{17} cm^{-3} was found for the main trap in undoped BGO. Assuming $m_e/m \sim 14$ [81] where m_e is the electron effective mass and m is the electron mass we obtain a value of $\mu_0 = 5.9$ cm^2/Vs for undoped BGO. We didn't measure trap concentrations in Fe-doped BGO or undoped BSO, but if we assume the same value for the concentration of the main trap in these samples as that measured in undoped BGO we obtain values of 2.3 and 1.4 cm^2/Vs for 0.3% Fe-doped BGO and undoped BSO, respectively.

5.5 Discussion of Results

The present data support the concept of a trap limited drift of electrons through the conduction band under the action of the applied field. Using curve fitting we have determined the average mobility of the carriers and the width of the carrier packets. The average drift mobilities we obtained by fitting are independent of applied field, but are exponentially dependent on temperature. The independence of the drift mobility on applied field, and the quality of the fits to the tails of the current transients, are consistent with the drift of a Gaussian packet of carriers through the sample. The Gaussian distribution of carriers probably arises from multiple trapping and detrapping of the carriers in the carrier packet as it travels through the sample.

In contrast to the experiments performed by Ennouri et al. [64] we were able to obtain reproducible current transients in BGO and BSO using no background illumination. In fact, in our case additional blue or red illumination proved to be detrimental. When the samples were illuminated with blue or red light during the laser pulse the current transients were very erratic and irreproducible. This was

also true if the measurements were performed with the samples in the dark after illuminating them with blue light. Ennouri, however, found that the samples had to absorb a certain minimum number of photons before each measurement to reduce the accumulation of space-charge from the previous laser pulse. The differences may have been caused by differences in the intensity of the laser pulses and the background illumination. Our laser pulses were attenuated to an energy of 0.2 μJ which for the wavelength of 337 nm corresponds to only 3×10^{11} photons per pulse. Ennouri et al. used pulses with an energy of 2.5 mJ which is 4 orders of magnitude stronger. This high pulse energy may have generated enough carriers to cause the undesirable space-charge effects.

An interesting result shown by the curve fitting is seen by examining Fig. 5.8. This figure shows that some of the carriers have zero or negative average velocities. Scott et al. also found that some of the carriers had negative average velocities [78]. This is physically reasonable since it can be expected that some of the carriers will recombine or be trapped at very deep traps from which the probability of thermal emission is negligible. In addition, there may be high space-charge fields near the illuminated electrode right after the laser pulse which cause some of the carriers to travel in the opposite direction.

The nearly exponential dependence of the mobility and velocity distribution width on temperature can be explained by assuming that the electrons are trapped during their transit through the sample and are eventually released so that they can continue towards the back electrode where they recombine. The activation energies obtained from these temperature dependencies are consistent with activation energies obtained from the analysis of TSC data on these samples [80]. In undoped BGO there is a TSC peak at $\sim$ 145 K which, according to the analysis of Bloom and McKeever [80], is distributed in activation energy with a central value of $E_t = 0.29$ eV and a distri-

bution width of $\Delta E \approx 0.06$ eV. The upper limit of the distribution, then, extends to ~ 0.32 eV, so our result of $E_t = 0.31$ eV from the temperature dependence of the drift mobility corresponds to the upper part of this distribution. The temperature dependence of the width of the velocity distribution gave slightly higher values, however. For the 0.3% Fe-doped BGO sample our TSC results show that this trap has an activation energy of $E_t = 0.32$ eV with a width $\Delta E \approx 0.04$ eV. From the temperature dependence of the mobility we extracted an activation energy of $E_t = 0.34$ eV which, again, is in the upper part of the distribution determined from our TSC analysis. The values of E_t obtained from the temperature dependence of the velocity distributions agree well with those from the mobility and TSC measurements.

The reason that the drift mobility is approximately an order of magnitude less in 0.3% Fe-doped BGO than in undoped BGO may be that the active trap is slightly deeper in the Fe-doped material resulting in slower detrapping of the trapped carriers. We don't have fitting results to TSC data measured in undoped BSO, but our result here of $E_t = 0.31$ eV seems reasonable given the similarity of BGO and BSO. The temperature dependence of the width of the velocity distribution is consistent with that predicted by Eq. (5.13) for both the undoped and 0.3% Fe-doped BGO samples, but the results for the undoped BSO sample were not as good. In undoped BSO σ_v has a strong temperature dependence, but there is a lot of scatter to the values, and we have not made Arrhenius plots for these data.

The curvature shown by the data in Fig. 5.10 may be due to the active trap being distributed in activation energy rather than having a single valued activation energy. The curvature may also be due to carriers being trapped into multiple trapping states during their transit.

5.6 Summary and Conclusions

We performed time-of-flight measurements on undoped and Fe-doped BGO and undoped BSO between the temperatures of $\sim$ 210 K and 300 K. By fitting our data we were able to extract values for the average drift mobility of the carriers and show that the shape of the current transients is consistent with the propagation of a Gaussian distribution of electrons through the sample. We found an exponential dependence of the drift mobility and carrier packet width on temperature in all samples indicating that the drift mobility is trap limited. The drift mobility in undoped BGO varied from 6.1×10^{-4} cm^2/Vs at 210 K to 0.11 cm^2/Vs at 300 K. In Fe-doped BGO and undoped BSO the mobilities were about an order of magnitude smaller at all temperatures. An activation energy of $E = 0.31$ eV in undoped BGO determined from the temperature dependence of the mobility agrees well with values of activation energy determined from the analysis of TSC measurements on undoped BGO. We believe that the trap controlling carrier drift during a TOF experiment (and probably during grating writing as well) is responsible for a TSC peak centered at $\sim$ 150 K and is distributed in activation energy with a central value of $E = 0.29$ eV and a width of 0.06 eV, agreeing well with the value obtained from the temperature dependence of the drift mobility.

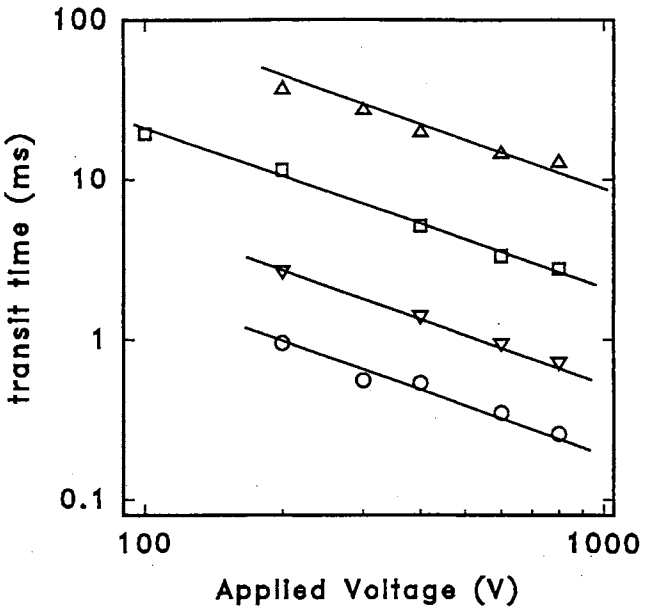

Figure 5.4: Figure showing linear dependence of transit time (as defined by the kink) on voltage at ○ 280 K, ▽ 260 K, □ 240 K and △ 220 K.

Table 5.1: Drift mobilities in cm^2/Vs obtained for undoped BGO, 0.3% Fe-doped BGO and undoped BSO.

Temperature (K)	undoped BGO	0.3% Fe-doped BGO	undoped BSO
210	0.00061	-	-
220	0.0013	-	-
230	0.0031	-	0.00059
240	0.0055	0.00062	0.0013
250	0.011	0.0014	0.0021
260	0.021	0.0021	0.0044
270	0.034	0.0040	0.0074
280	0.055	0.0064	0.011
290	0.075	0.010	0.014
300	0.11	0.019	-

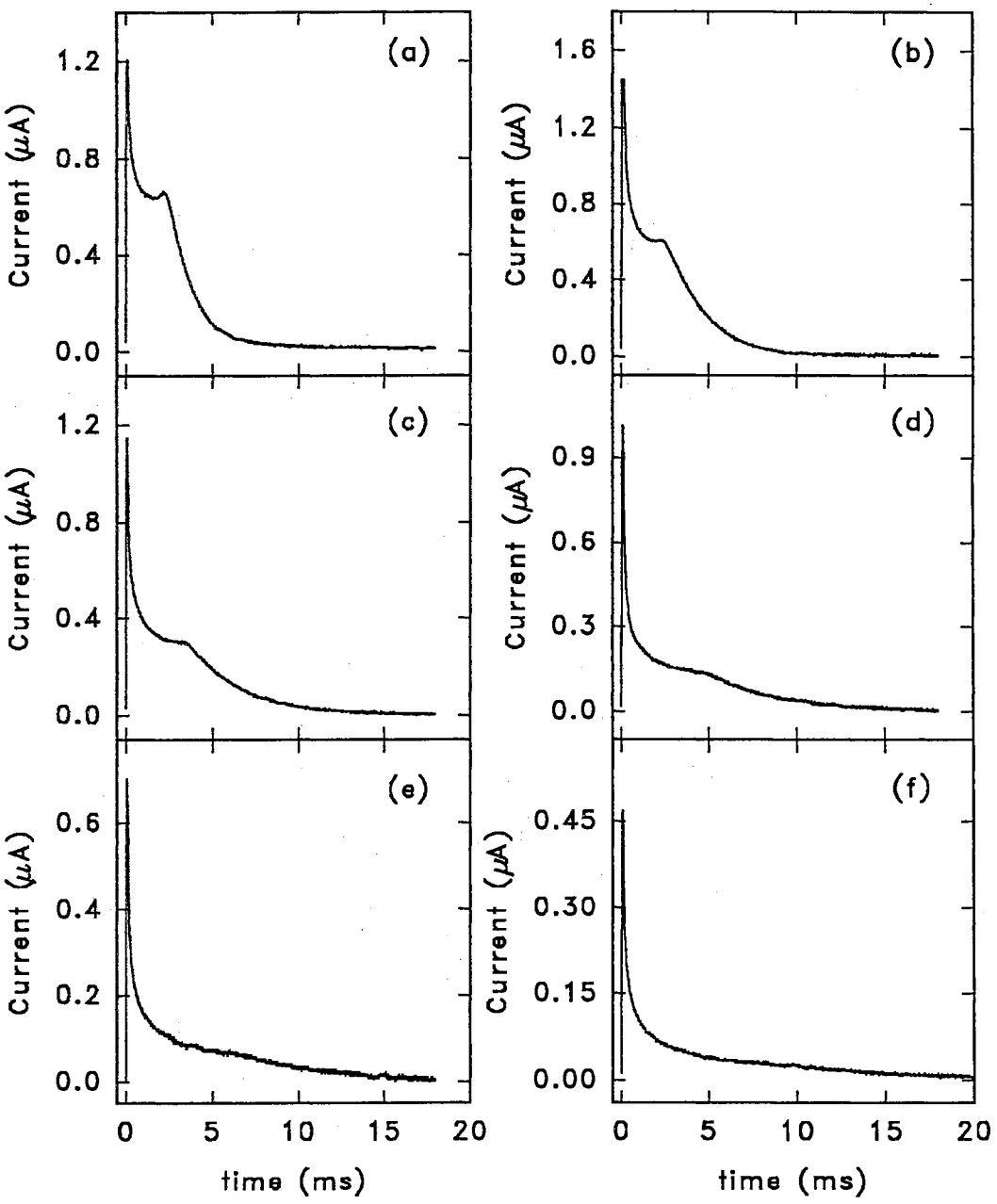

Figure 5.5: Electron TOF transients measured in 0.3% Fe-doped BGO at 270 K with applied fields of (a) 9100, (b) 7300, (c) 5500, (d) 3600, (e) 1800 and (f) 900 V/cm.

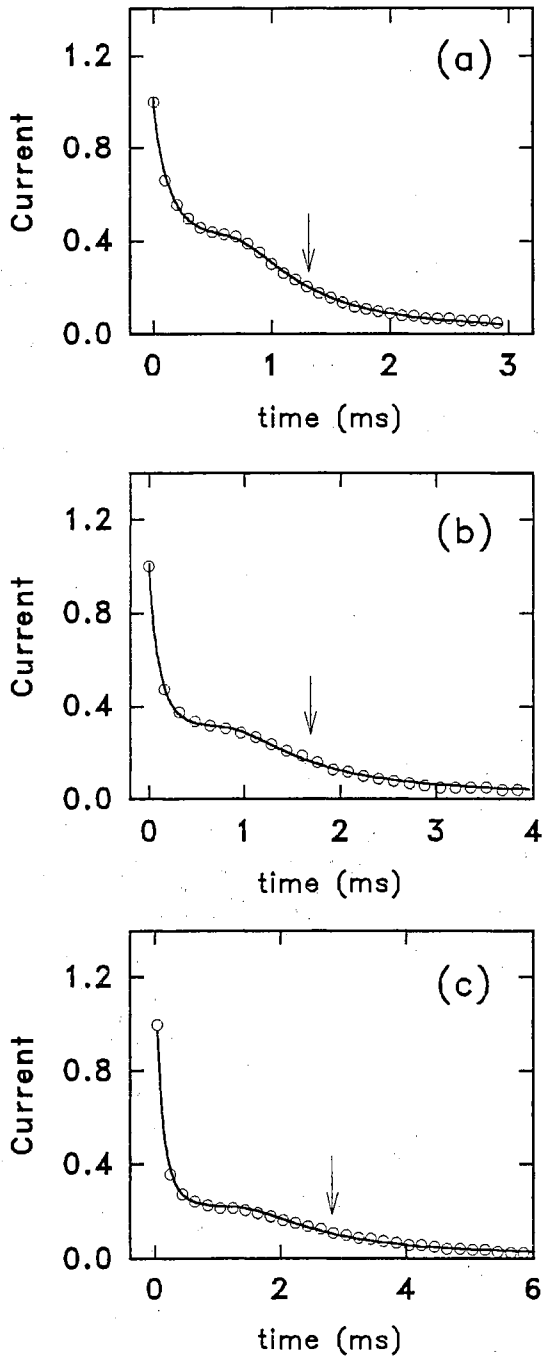

Figure 5.6: Fits to normalized TOF transients measured at 250 K in undoped BGO. The applied fields were (a) 7270, (b) 5450 and (c) 3640 V/cm.

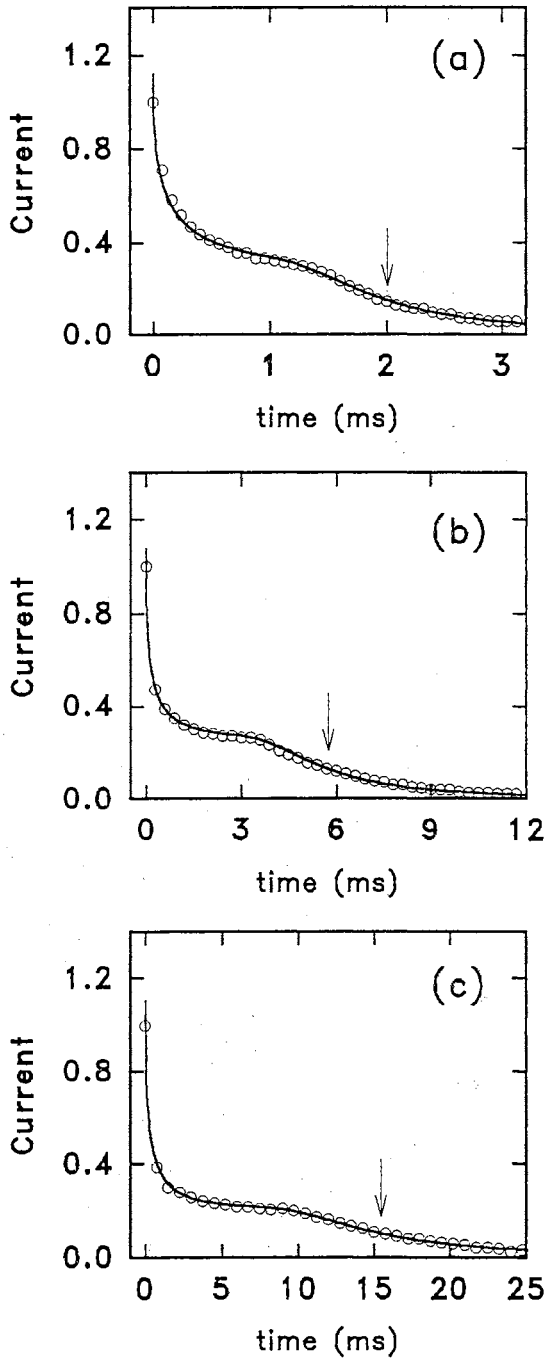

Figure 5.7: Fits to normalized TOF transients measured in 0.3% Fe-doped BGO at (a) 290, (b) 270 and (c) 250 K.

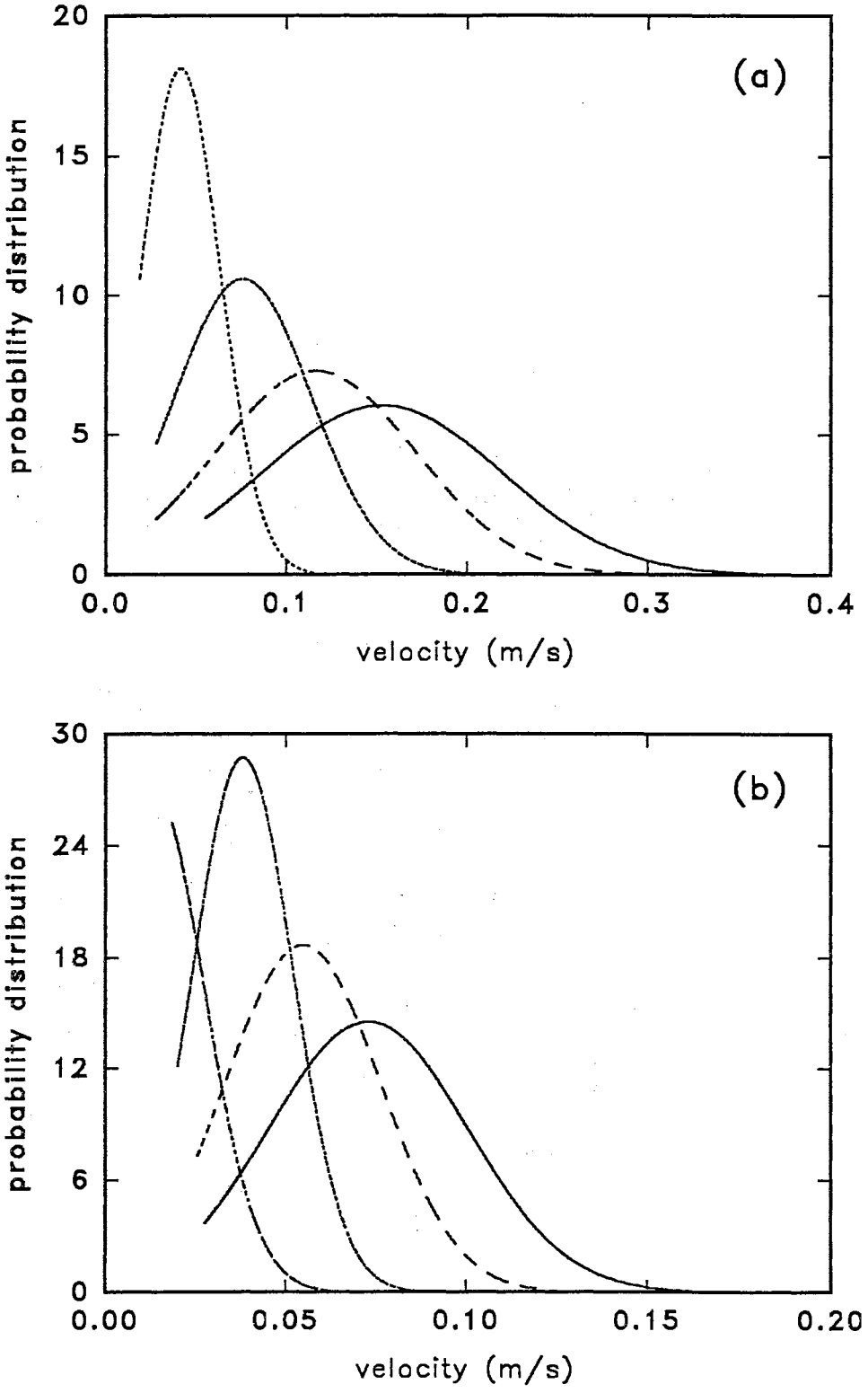

Figure 5.8: Velocity distributions resulting from fits to (a) undoped BGO transients at 260 K and (b) 0.3% Fe-doped BGO transients at 290 K. From left to right the applied fields were 1820, 3640, 5450 and 7270 V/cm.

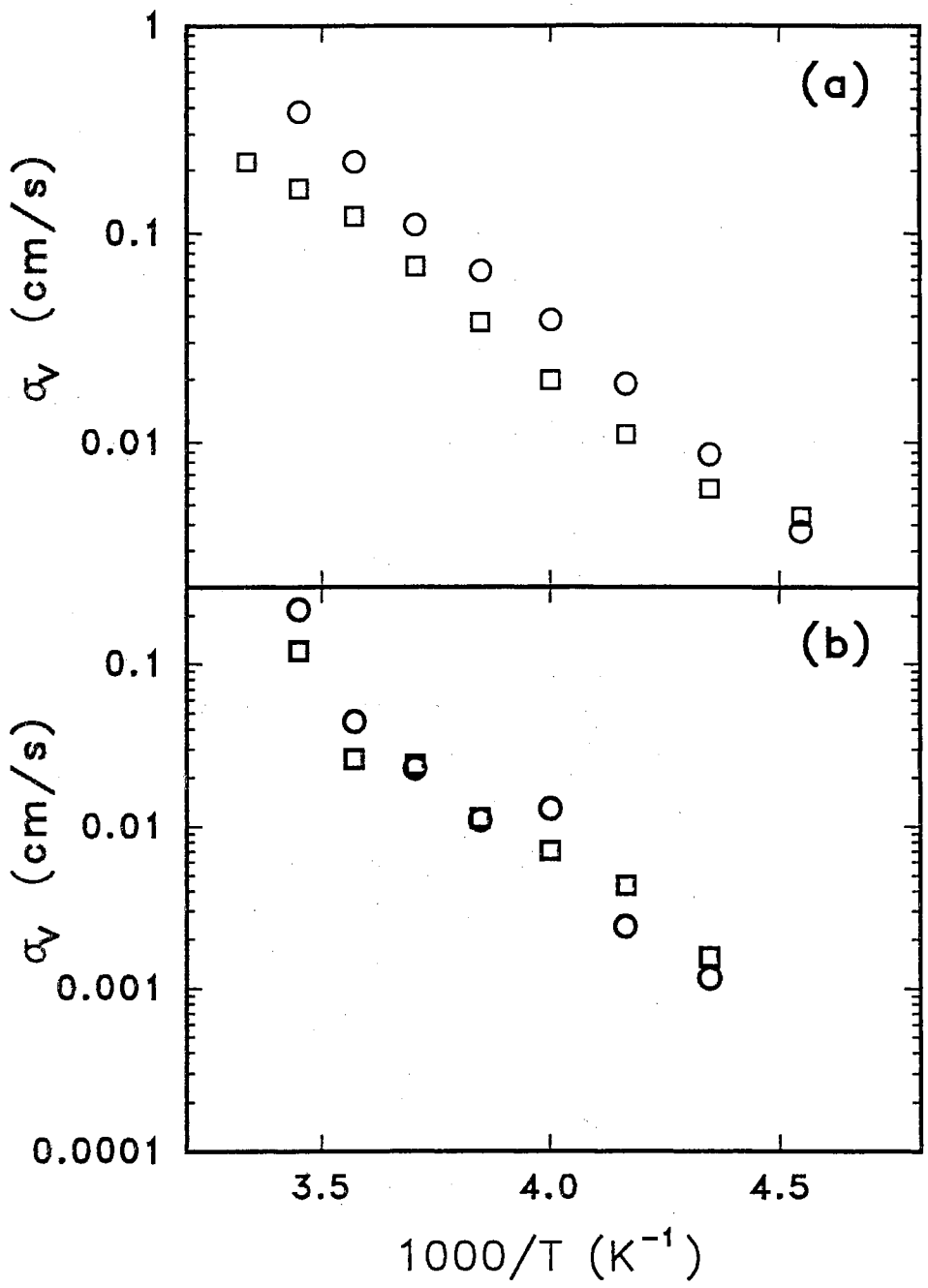

Figure 5.9: Temperature dependence of the width of the velocity distribution in (a) undoped BGO and (b) 0.3% Fe-doped BGO for applied fields of ○ 7270 V/cm and □ 3640 V/cm.

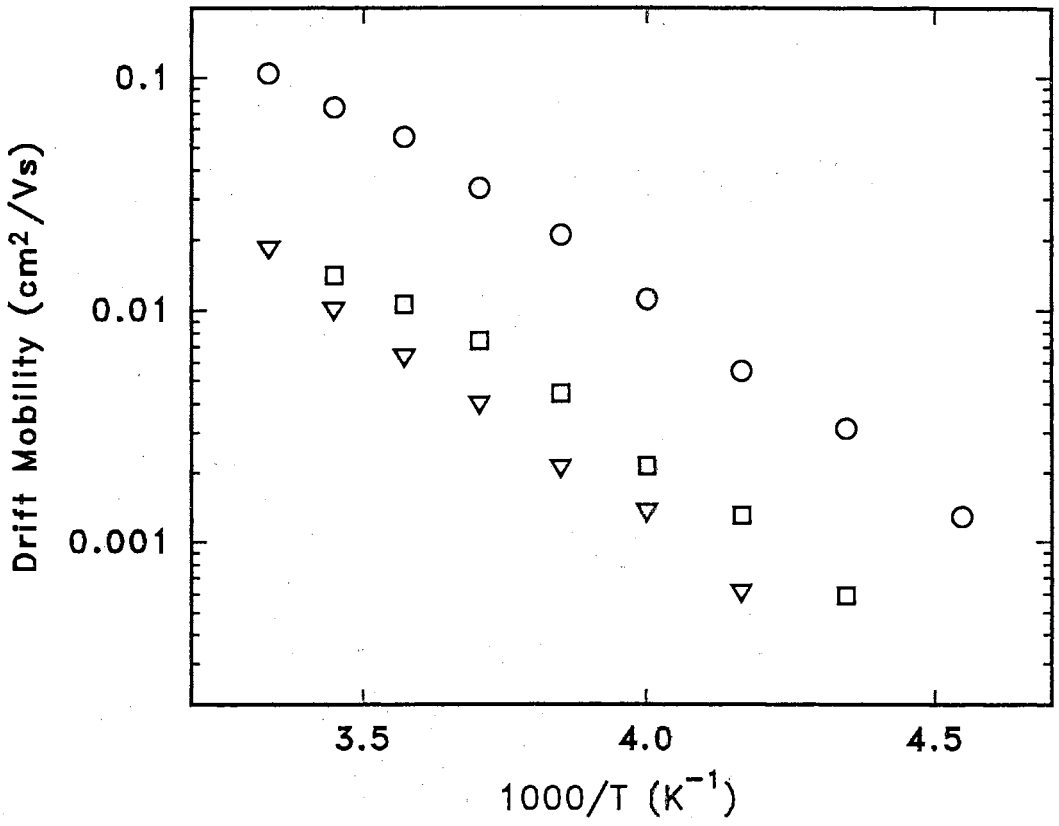

Figure 5.10: Temperature dependence of the drift mobility in ○ undoped BGO, □ undoped BSO and ▽ Fe-doped BGO.

Chapter 6

Photorefractive Measurements

6.1 Introduction

The photorefractive effect in the sillenites is of particular interest because it is the mechanism through which information is stored in these materials. As mentioned in the introduction there are a number of requirements which must be met by a material in order to be useful in photorefractive applications, although some of the requirements depend on the particular application itself. If no traps were present the storage time of information written in the material would be very short. With trapping, storage times increase to the trap lifetime. Also, the concentration of traps is important because this determines the maximum space-charge field and therefore the maximum modulation in the refractive index. In addition, shallow traps may affect the speed of response of a device since carriers may be temporarily trapped by shallow states before settling in a deep trap. Lastly, the cross-section of photon capture of trapped carriers plays a role in both information erasure and reading since light can excite the carriers out of the traps therefore causing the loss of information.

We performed photorefractive measurements on undoped and Ga-doped BGO between the temperatures of 20 K and room temperature. We studied the thermal stability of gratings written at low temperature and the effect of temperature on grating writing. Our purpose was to relate the thermal stability of the photorefractive

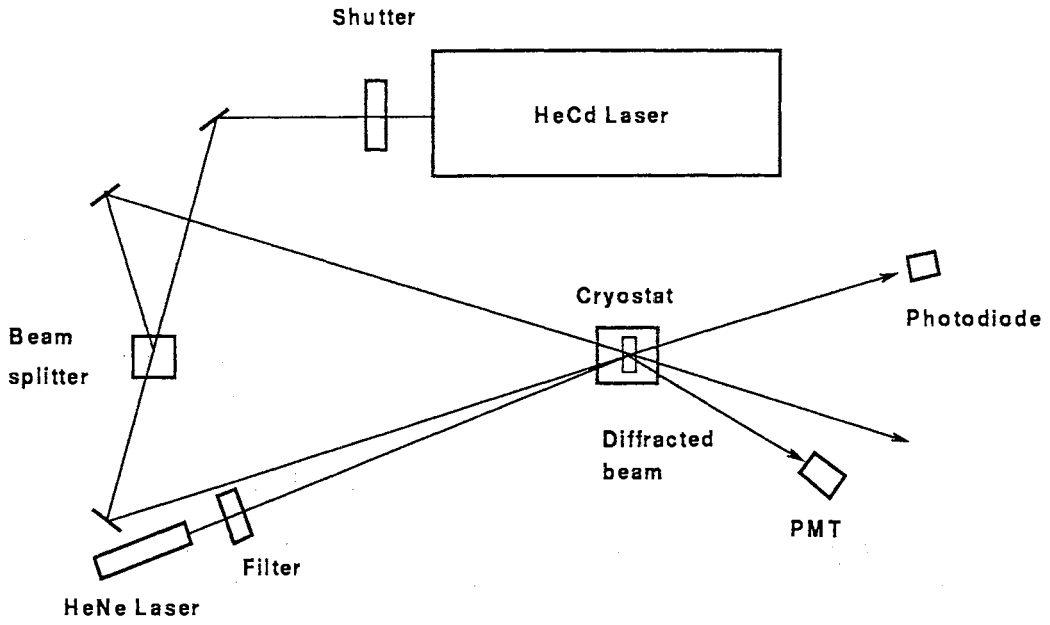

Figure 6.1: Experimental setup used for photorefractive measurements.

effect to specific traps.

6.2 Experimental Details

The experimental setup is shown in Fig. 6.1. A Helium-Cadmium laser at 442 nm was used to write gratings by splitting the beam and crossing the resulting two beams inside the sample. A Helium-Neon laser attenuated to 0.5 mW was used as the read laser. The samples were mounted in a Helium gas refrigerator and the diffracted signal was measured using a PMT. The fast response (grating write cycle) was measured on an oscilloscope while the slower response (grating decay) was measured on a digital multimeter. The oscilloscope was triggered by a photodiode placed in the path of one of the write beams. The data were downloaded to a PC and saved to the hard drive.

The experiments were performed by cooling the sample to the temperature of interest and then exposing the sample to the read beam (HeNe laser). The write shutter was then opened and a grating was written. The grating write time was

varied, from very short times to times long enough for the signal to saturate. After writing the grating, the write beam shutter was closed and the dark decay of the signal was monitored using the read beam. An oscilloscope was used to record the grating write period and the initial part of the decay and a digital multimeter was used to record the decay of the grating over a long time period. This measurement was performed over the temperature range from ~20 K to room temperature to study the efficiency of grating writing as a function of temperature.

The thermal stability of the gratings was also studied. In this measurement the sample was cooled to ~20 K and a grating was written using a write time that gave the maximum diffracted signal. Next the sample was allowed to warm up slowly (at a rate of ~2 K/min) and the diffracted signal was recorded every 2 K. In this measurement the sample was kept in the dark except for a 0.5 s interval when the read beam shutter was opened to take a measurement. This helped avoid erasure of the grating by the read laser.

6.3 Results

A typical write period is shown in Fig. 6.2. In this measurement the read beam is on continuously and the write beam shutter is opened at time $t = 0$ and turned off at $t = 5$ s. This measurement was performed at 100 K on an undoped BGO sample using a grating spacing of 2.1 μm. The data show that the diffracted signal increases steadily from 0 until it saturates at about 2.5 s. At higher temperatures the signal reaches its maximum value in a much shorter time of about 100 ms.

The write and decay periods of a grating written in undoped BGO are shown in Fig. 6.3 for temperatures of 125, 200 and 297 K. The write times were 0.5 s at 297 K and 200 K and 1 s at 125 K. These data show that the signal decays at all three temperatures after the write period with the fastest decay occurring at the highest

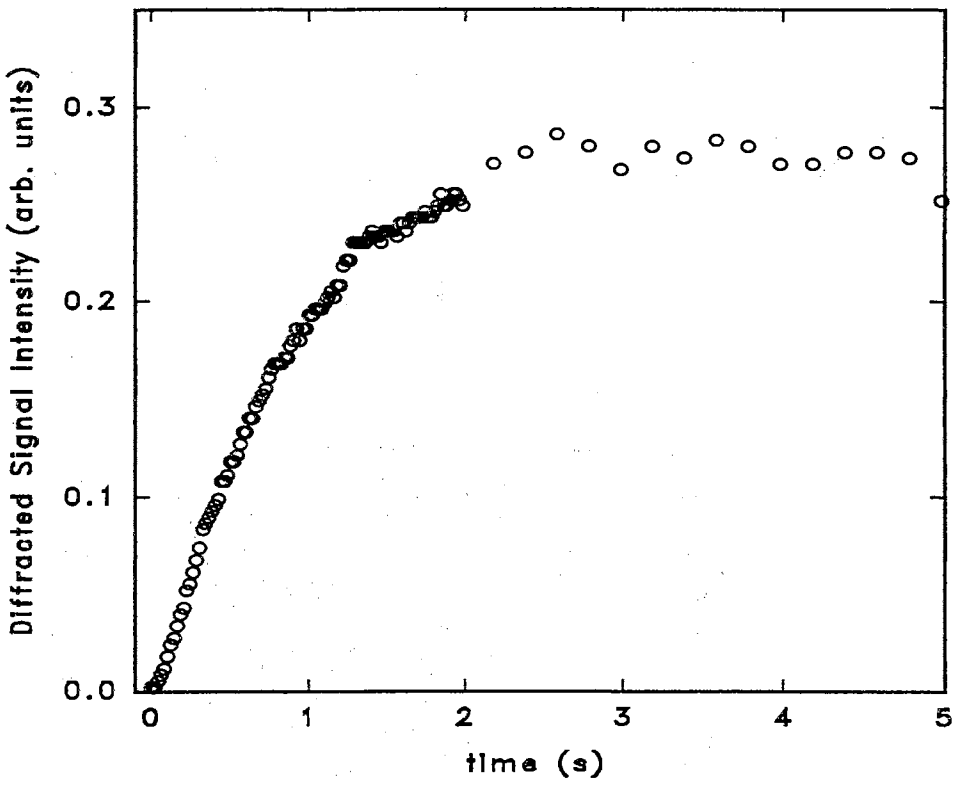

Figure 6.2: Writing of a grating in undoped BGO at 100 K. The grating spacing was 2.1 μm.

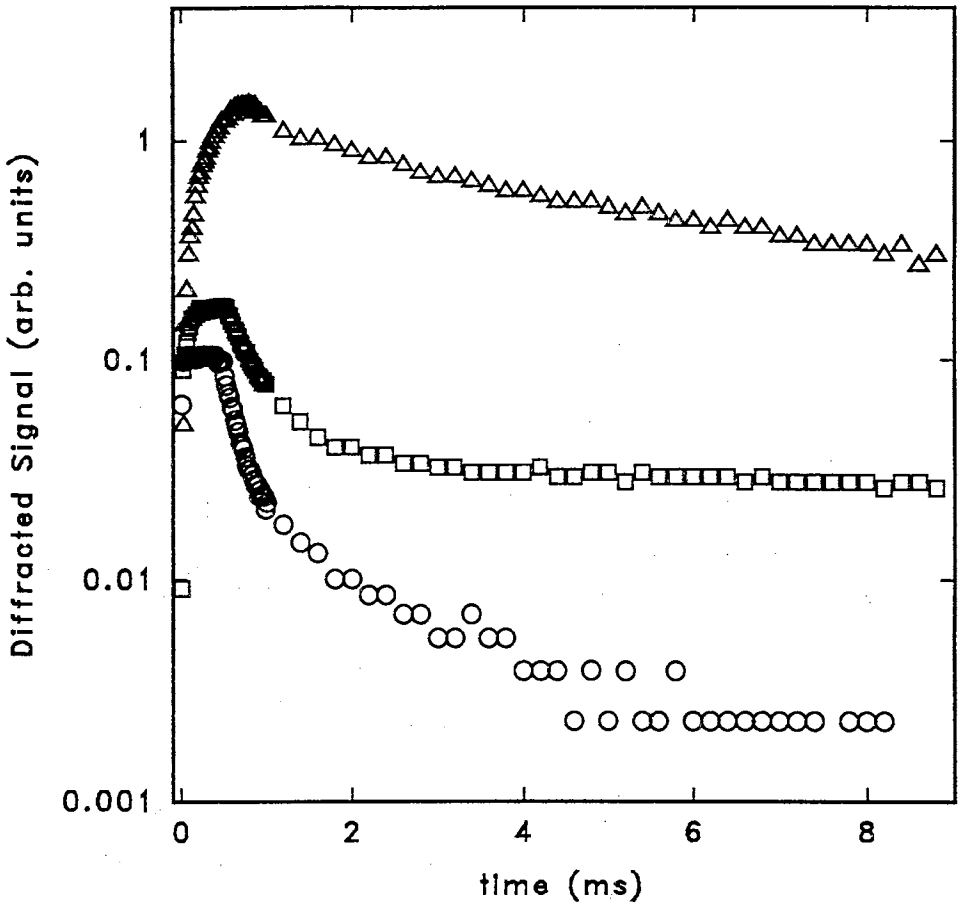

Figure 6.3: Write and decay of gratings in undoped BGO at △ 125 K, □ 200 K and ○ 297 K.

temperature. This is likely due to the shorter trap lifetime at higher temperature. It is also evident that the grating is much stronger at lower temperature than at higher temperature. This is also due most likely to the increased thermal stability of the traps at lower temperature. Fig. 6.4 shows similar data for the 2% Ga-doped sample.

The temperature dependence of the maximum value of the diffracted signal is shown in Fig. 6.5 for both the undoped and 2% Ga-doped samples over the temperature range from 40 K to 300 K. The diffracted signal in the Ga-doped sample increases over the entire temperature range measured, but the undoped BGO sample shows a peak which appears to occur between 75 and 100 K. This has been seen by

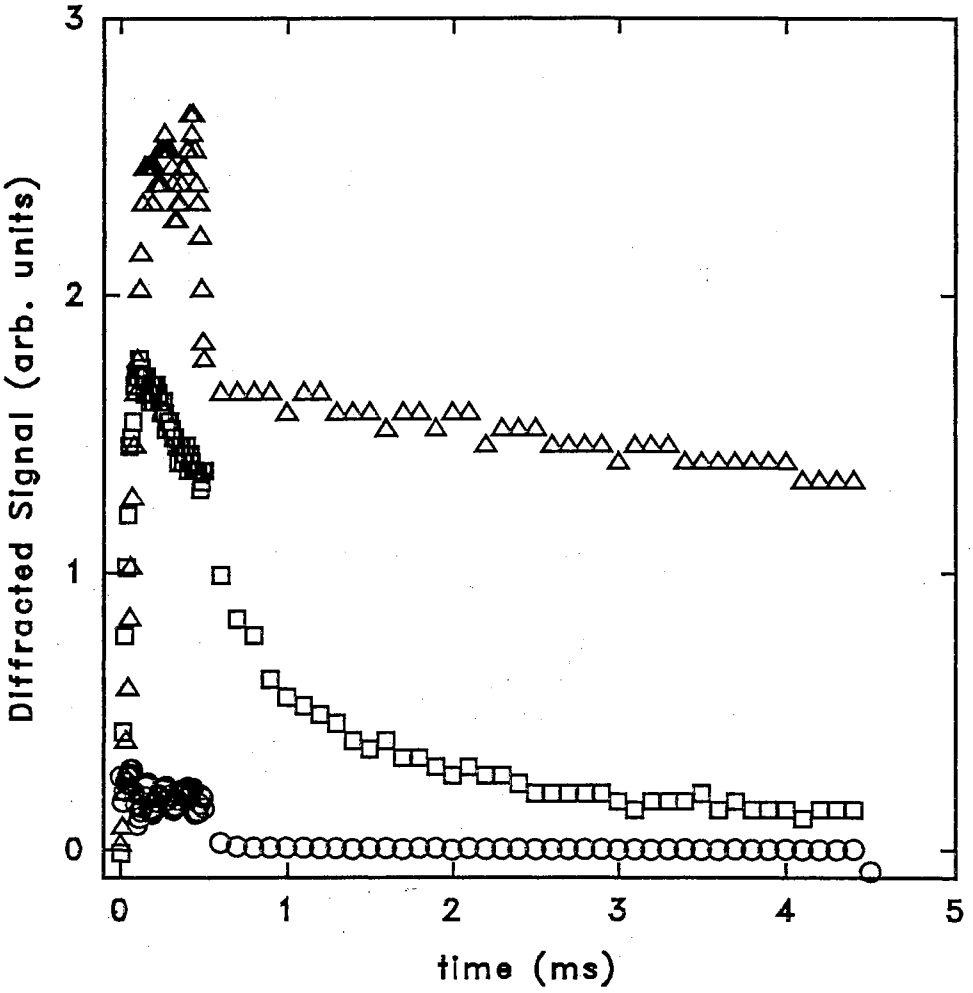

Figure 6.4: Write and decay of gratings in 2% Ga-doped BGO at △ 50 K, □ 200 K and ○ 300 K.

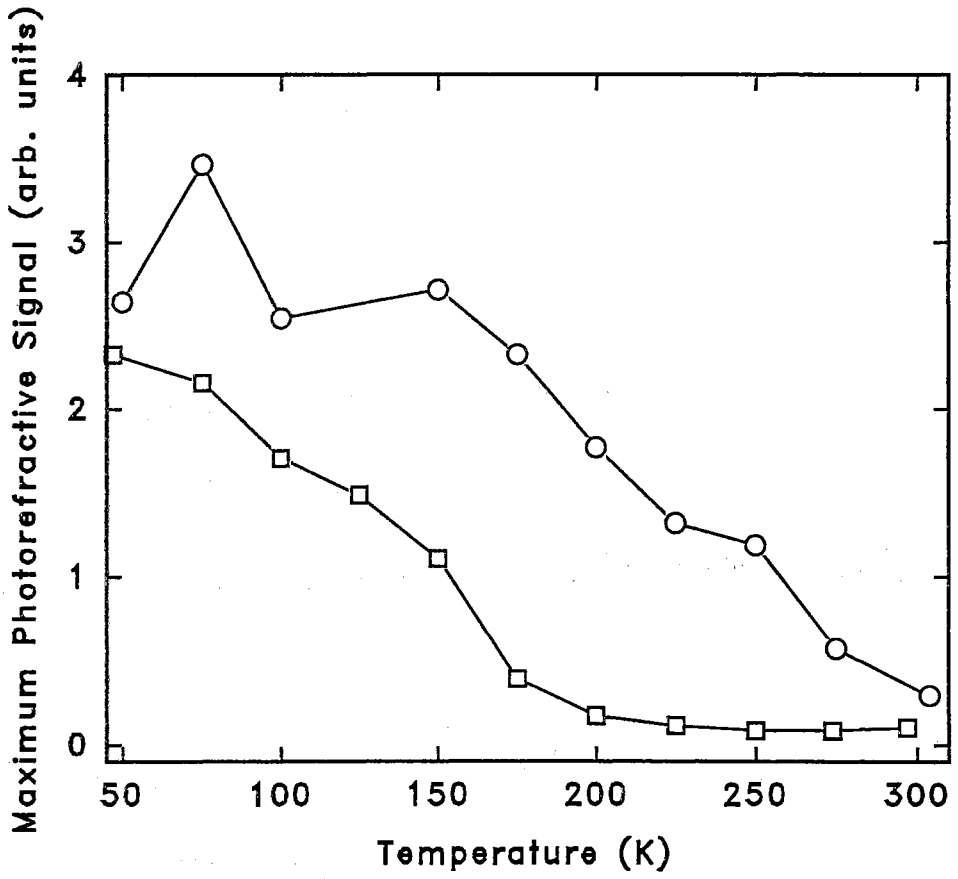

Figure 6.5: Temperature dependence of the maximum diffracted signal during grating writing in □ undoped and ○ 2% Ga-doped BGO.

other authors as well [88]. At higher temperatures the signal gets weaker until about 200 K for the undoped BGO sample where the signal amplitude reaches a residual level. The signal in 2% Ga-doped BGO, however, continues to decrease throughout the range from 200 K to 300 K.

In addition, the thermal stability of gratings written at low temperature was measured. This measurement was performed by monitoring the decay in the diffracted beam intensity as the sample was warmed up. Two methods were used. In one type of experiment the read beam was left on continuously during the heating cycle while in the other the read beam shutter was kept closed except for a 0.5 s interval during which a measurement of the diffraction efficiency was made. Fig. 6.6 shows data for

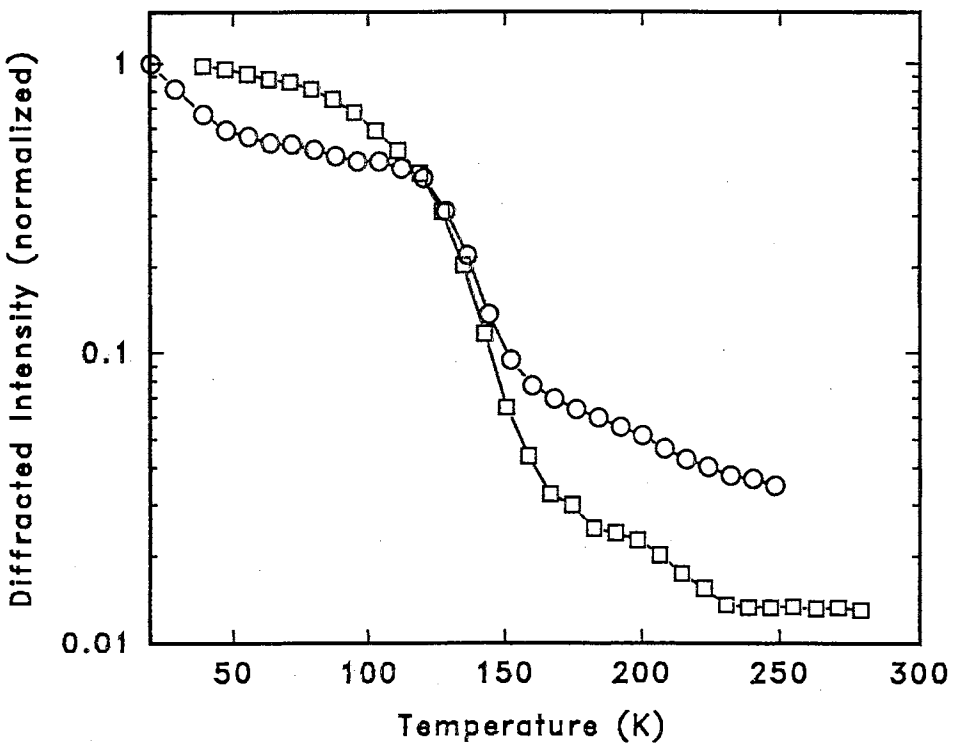

Figure 6.6: Thermal decay of gratings written at 20 K in □ undoped and ○ 2% Ga-doped BGO.

both undoped and 2% Ga-doped BGO for the conditions in which the read beam shutter was kept closed except when measuring the the diffraction efficiency. The data show that the grating decays gradually until ~110 K in undoped BGO and ~120 K in 2% Ga-doped BGO. After these temperatures the major decay takes place resulting in the signal being an order of magnitude weaker 50 K later. It will be shown later that this decay region matches the position of a large TSC peak and corresponds to the temperature at which the decay in photoconductivity occurs in both types of sample. After these temperatures the decay occurs more gradually. At 240 K the diffracted signal intensity in undoped BGO has reached its lowest value.

Fig. 6.7 compares the decay obtained for undoped BGO when the read beam is left on continuously during the heating cycle to the data obtained when the read beam shutter is closed except for a 0.5 s interval during the measurement. The data show

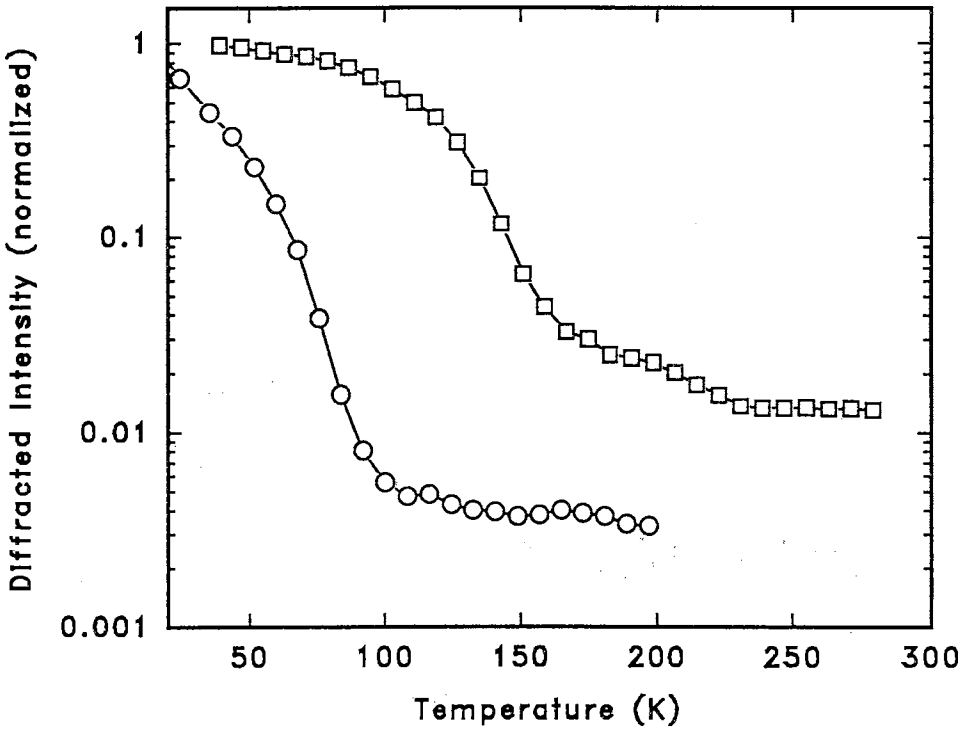

Figure 6.7: Thermal decay of gratings written at 20 K in undoped BGO under experimental conditions where the sample is exposed to the read beam continuously (○) and for 0.5 s (□) to take each data point.

that the decay is much faster when the read beam is incident on the sample during the entire heating cycle. This suggests that the read beam is emptying trapping states which contribute to the space-charge field.

6.4 Discussion

The increase in grating lifetime at lower temperature is an indication that the carriers causing the space-charge field have been trapped. As the temperature decreases the traps become more stable and therefore support a higher trapped carrier concentration resulting in larger space-charge fields and a stronger grating. We believe that the decay of the diffracted signal corresponds to the emptying of traps. Comparing results of TSC measurements and measurements of the anneal characteristics of photocon-

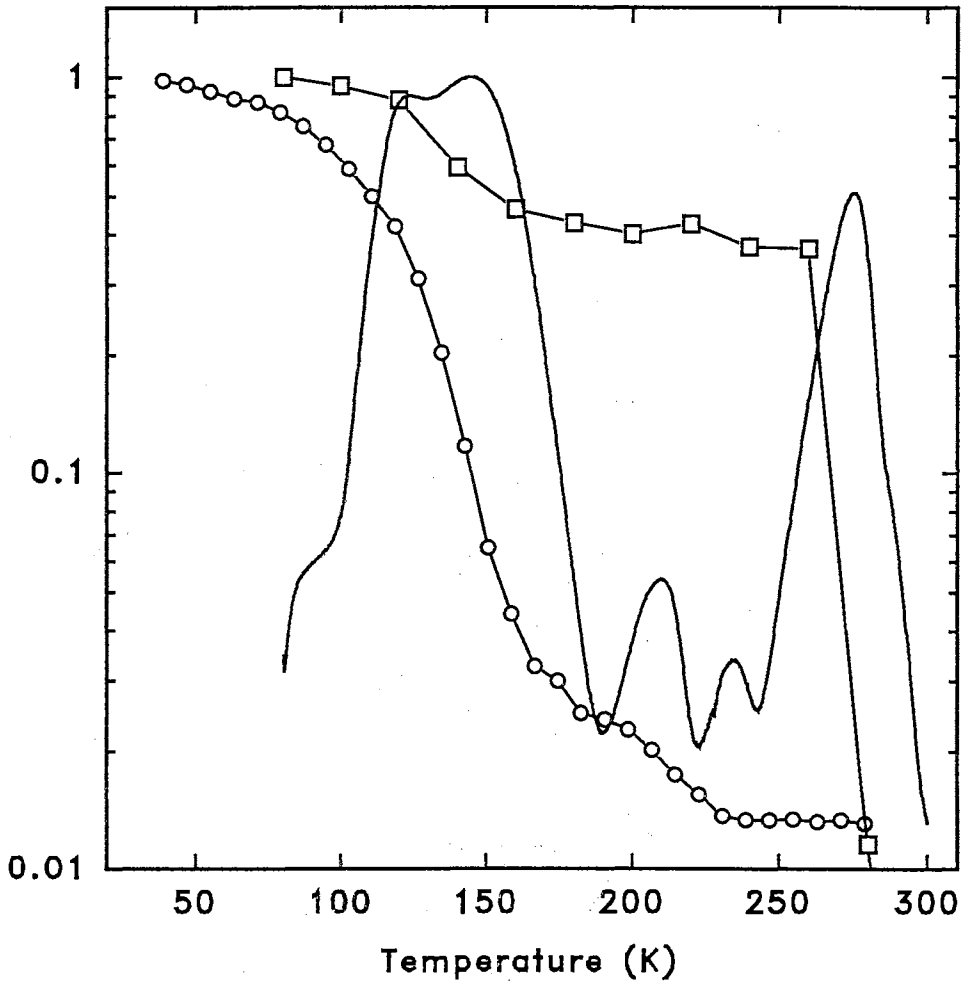

Figure 6.8: Comparison of the thermal decay of a laser-induced grating (circles) and photoconductivity signal (squares) with TSC spectra in undoped BGO (solid line).

ductivity signals, which both show the temperatures at which trap populations decay, with the temperature dependence of the laser-induced gratings provides support for this contention. This is shown in Fig. 6.8 for the undoped sample and in Fig. 6.9 for 2% Ga-doped BGO. In both figures the TSC, photoconductivity annealing curves and thermal grating decay data have been normalized and overlaid. A major decay in the photorefractive signal occurs over the temperature range from ~120–180 K in undoped BGO and ~120–160 K in 2% Ga-doped BGO and in both cases this coincides with the dominant peak in the TSC spectra and a pronounced decay in the photoconductivity anneal curves. Our TSC analysis, presented in Chapter 4 and in

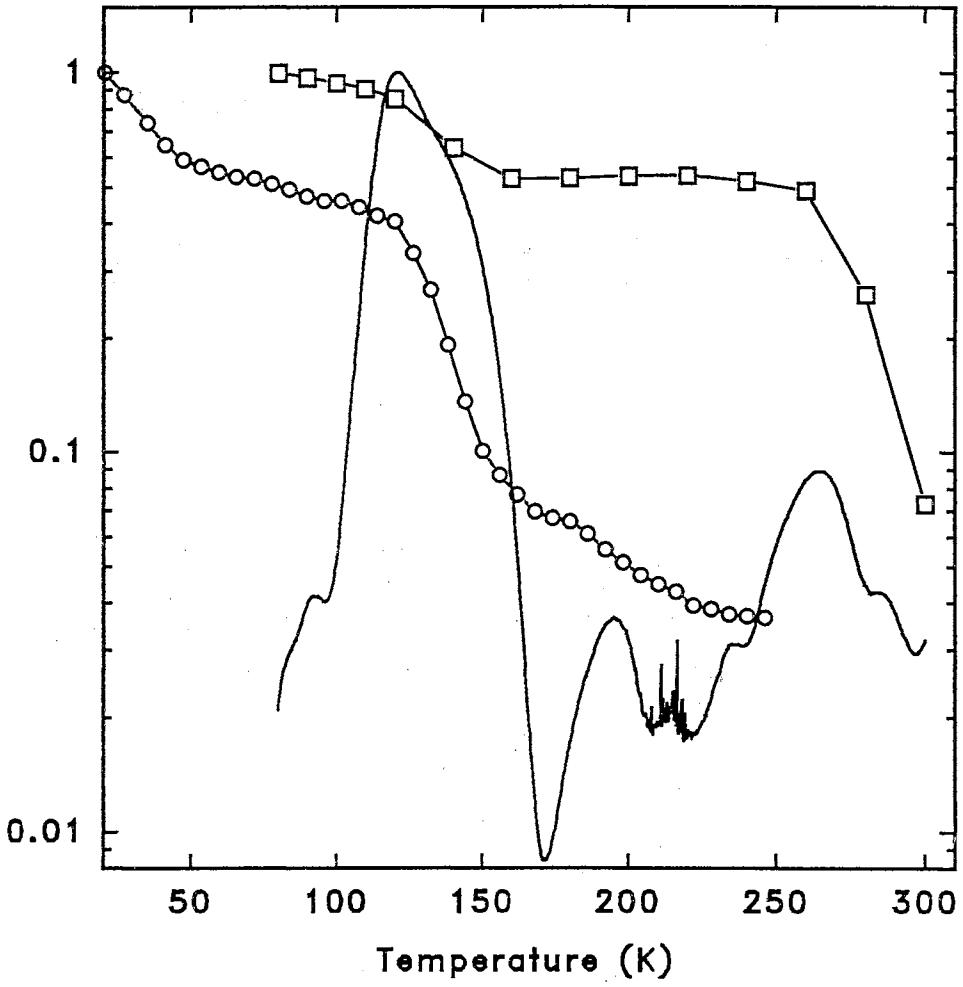

Figure 6.9: Comparison of the thermal decay of a laser-induced grating (circles) and photoconductivity signal (squares) with TSC spectra in 2% Ga-doped BGO (solid line).

reference [80], indicated that the trap responsible for this peak is distributed in activation energy and we have shown in Chapter 5 that this trap is the one which limits the mobility at temperatures between 200 K and 300 K. After the major decay in the diffracted signal the more gradual decay coincides with the group of overlapping TSC peaks which are present above ~190 K in undoped BGO and above ~170 K in 2% Ga-doped BGO.

6.5 Simulations

A large number of papers have been published regarding modeling of the photorefractive effect in a variety of materials including BGO and BSO [89-98], but many of these papers have been based on overly simplistic models or, in many cases, the method used to solve the equations required approximations which may make the results questionable. For example, some papers have been based on models that include a donor level which acts as the source of electrons, but includes no trapping states except for the empty donor states [89,90,93-96]. This is not a realistic model for BGO and BSO because TSC measurements show that there are a large number of trapping states in addition to the empty donor levels and the temperature dependence of the photorefractive effect appears to show that the traps play an important part in the photorefractive response. The assumption of no traps is commonly made to allow an analytical solution to the equations; however, in order to explain all of the experimental data traps need to be included. Even in cases where numerical techniques have been used to solve the equations allowing a more sophisticated model approximations still have to be made. One numerical technique which has been used involves expanding the concentrations and electric field in an infinite Fourier series which is then truncated to a small number of terms [94,95]. The problem with this method is that if too few terms are included the solutions will be inaccurate. In this section a

numerical method is presented which can be used to solve equations describing the photorefractive effect without any of these potential problems.

We used the model shown in Fig. 6.10. It is a simplification of a model which was presented in reference [27]. The model includes one electron trapping state of concentration N_t and the deep donor level, N_d, which is partially compensated by an acceptor level present with a concentration of N_A. Holes were not included in the simulations. Incident laser radiation excites electrons out of filled donor levels which may then drift under an applied electric field (if any) and diffuse until the electrons recombine with empty donors or become trapped in trapping states. The allowed electron transitions include optical excitation out of the donor level and the trap, thermal excitation out of the trap, capture of conduction band electrons by the trap and recombination of free electrons with empty donor states. The donor level is assumed to be deep enough that thermal excitations to the conduction band are negligible. The equations describing the dynamics of charge generation, trapping, detrapping, drift and diffusion in one dimension are:

$$\frac{\partial n_c}{\partial t} = -\frac{\partial n_t}{\partial t} - \frac{\partial n_d}{\partial t} + \frac{\partial}{\partial x}\left(\mu_e n_c E - \frac{k_b T}{e}\mu_e \frac{\partial n_c}{\partial x}\right) \tag{6.1}$$

$$\frac{\partial n_d}{\partial t} = -\alpha\phi(x) n_d + (N_d - n_d) n_c A_{De} \tag{6.2}$$

$$\frac{\partial n_t}{\partial t} = -\gamma_t n_t + n_c(N_t - n_t)A_t - \alpha_1 \phi(x) n_t. \tag{6.3}$$

The variables are: n_c, n_t, n_d — conduction band, trapped carrier and donor level concentration, respectively, μ_e — electron mobility, e — magnitude of charge on the electron, E — electric field, α and α_1 — probability that an incident photon is absorbed by an electron at a deep donor and at a trap, respectively, A_{De} and A_t — transition coefficients for free electrons to recombine and be trapped, respectively. The light intensity interference pattern is given by

$$\phi(x) = \phi_0 \left(1 + m\cos(kx)\right) \tag{6.4}$$

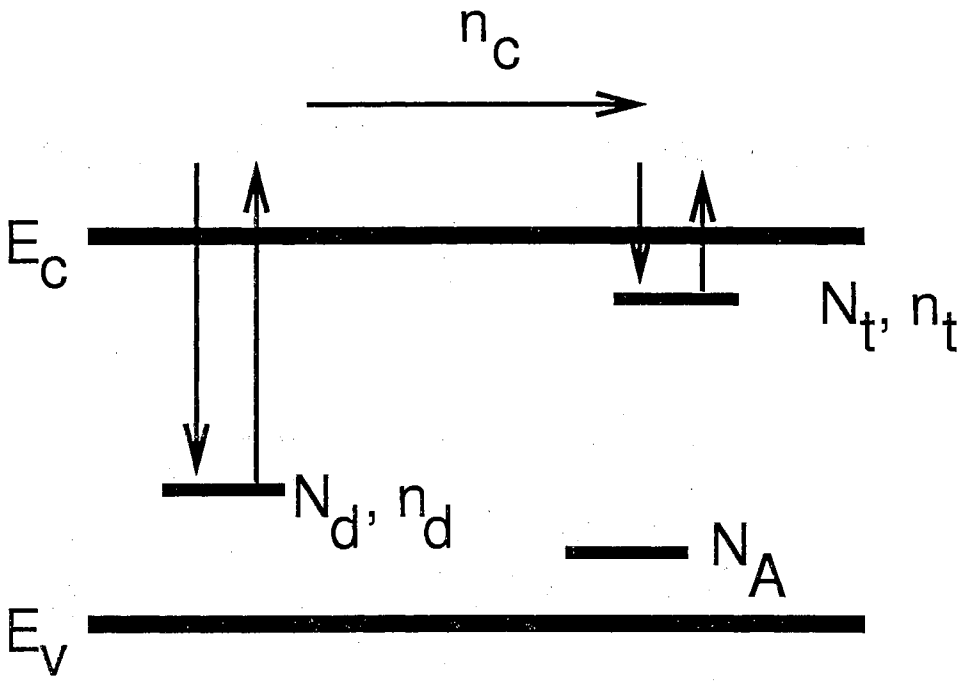

Figure 6.10: Model used for simulations of grating writing in undoped and Ga-doped BGO. The model consists of a deep donor level with a concentration of N_d, which is partially compensated by acceptor levels of concentration N_A, and one electron trap with a concentration of N_t.

where k is the grating wavevector and m is the spatial modulation in the light intensity due to the interference of the crossed laser beams.

We also need to use Poisson's equation to specify the electric field.

$$\frac{\partial E}{\partial x} = \frac{e}{\epsilon_0 \epsilon_r}(N_d - n_d - n_c - n_t - N_A) \tag{6.5}$$

ϵ_0 and ϵ_r are the permittivity of free space and the relative dielectric constant, respectively. Eq. (6.5) can be transformed to contain a derivative with respect to t by taking a time derivative and then using Eq. (6.1). The result is

$$\frac{\partial E}{\partial t \partial x} = \frac{e}{\epsilon_0 \epsilon_r}\left[-\frac{\partial}{\partial x}\left(\mu_e n_c E(x) - \frac{k_b T}{e}\mu_e \frac{\partial n_c}{\partial x}\right)\right]. \tag{6.6}$$

Integrating over x gives

$$\frac{\partial E}{\partial t} = -\frac{e}{\epsilon_0 \epsilon_r}\left[\mu_e n_c(x) E(x) - \frac{k_b T}{e}\mu_e \frac{\partial n_c}{\partial x}\right] + \frac{J_0}{\epsilon_0 \epsilon_r}. \tag{6.7}$$

The current density, J_0, is the constant of integration and is given by

$$J_0 = \int_0^1 e\mu_e n_c(x', t) E(x', t) dx' \tag{6.8}$$

where $x' = x/\Lambda$.

There is no analytical solution to these equations, so we solved them numerically using the "method of lines". This method involves discretizing the spatial coordinate and integrating the time coordinate. In this problem the x-dependence is periodic with a period equal to the grating spacing, Λ, so one period was broken into a number of subintervals. The center of each subinterval is a line with a constant value of x, hence the name, "method of lines". If the separation between the lines, Δx, is small enough the value of the concentrations and electric field at arbitrary x in each subinterval are well approximated by a quadratic, e.g.

$$B_i(x, t) \approx B_{1,i}(t)(x_i - i\Delta x)^2 + B_{2,i}(t)(x_i - i\Delta x) + B_{3,i}(t). \tag{6.9}$$

Here B_i represents any of the concentrations or the electric field a distance of Δx from line i. $B_{3,i}(t)$ is the value of the concentration or field at line i, i.e., the value which is calculated directly by solving Eqs. (6.1)–(6.3) or Eq. (6.7). The coefficients $B_{1,i}(t)$ and $B_{2,i}(t)$ which are needed to specify the concentration small distances from line i can be calculated from the boundary conditions of continuity of the value of the concentrations and electric field and their first derivatives at the midpoint between each pair of lines. Handling the spatial coordinate in this way allows the spatial derivatives of n_c and E to be calculated by differentiating Eq. (6.9) with respect to x. One set of Eqs. (6.1)–(6.3) and Eq. (6.7) was written for each line and then the time variable was integrated using the Runge-Kutta method. The number of lines used depended on the value of m. For $m = 0.1$ or lower only 13 lines were used, but for $m = 0.9$ as many as 53 lines were used.

Some typical results showing the buildup of the concentrations and space-charge field are shown in Fig. 6.11 for $m = 0.1$. The data have been normalized. The parameters which were used are as follows: $N_d = 10^{25}$ m^{-3}, $N_A = 2 \times 10^{24}$ m^{-3}, $N_t = 3 \times 10^{23}$ m^{-3}, $A_t = 10^{-19}$ m^3/s, $A_{De} = 10^{-18}$ m^3/s, $E = 0.3$ eV, $s = 10^8$ s^{-1}, $\mu_e = 10^{-10}$ m^2/Vs, $\Lambda = 10\mu$m, $T = 80$ K, $\alpha = 1$ and $\alpha_1 = 0$. As expected, the conduction band concentration reaches steady-state first, followed by the trap and donor concentrations and finally, the space-charge field. The space-charge field appears to reach steady-state last because it is very sensitive to small changes in the trap and donor level populations which don't appear on the scale of the graph. The space-charge field is very small initially because even though there are carriers in the conduction band and traps the space-charge field won't increase until the carriers have moved away from their original position. It should be noted that at 80 K with the parameters which were used the traps fill up completely.

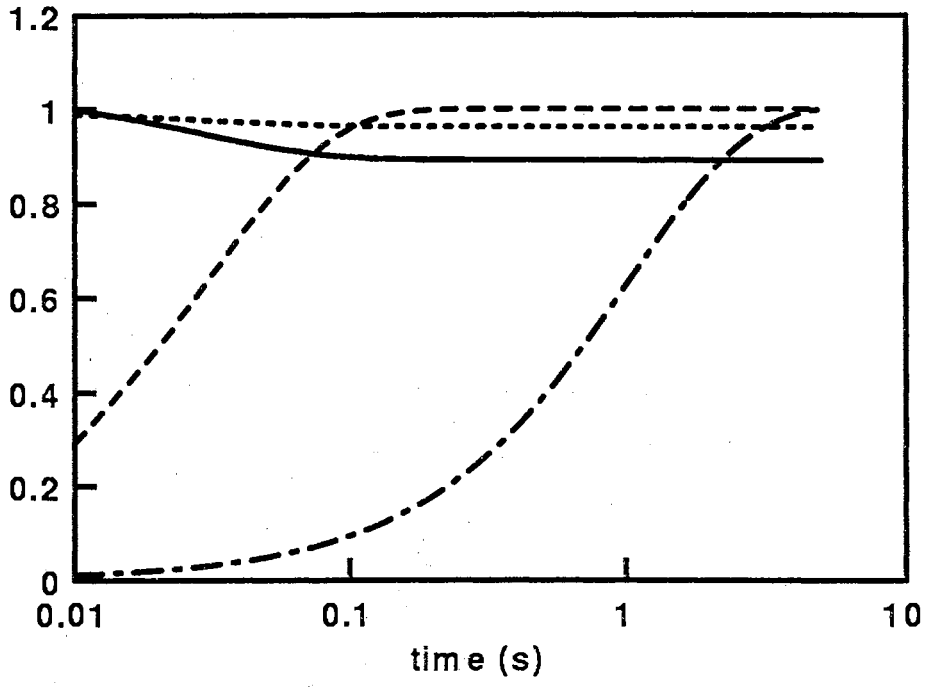

Figure 6.11: Simulation of build-up of carrier densities and electric field during writing of a grating. The curves are: solid line — conduction band concentration, dotted line — filled donor concentration, dashed line — trap concentration and dashed-dotted line — space-charge field.

6.5.1 Spatial profile

The spatial profile of the carrier densities and space-charge field is shown in Figs. 6.12 and 6.13. These figures show the x-dependence of the concentrations and electric field before saturation at 80 K for simulations performed with $m = 0.1$ and $m = 0.7$ and no applied field. The concentrations are symmetric since the applied field is zero. Fig. 6.12 shows that at low m the profile of the carrier densities and electric field retain their sinusoidal form. For low m the carrier densities and space-charge field retain their sinusoidal shape at saturation also, whereas for $m = 0.7$ the carrier densities lose their sinusoidal shape quickly. This has been seen by others as well [96]. Fig. 6.13 shows that the traps fill up first in the bright regions of the sample and as the illumination progresses electrons diffuse from the bright regions to the darker regions filling the traps as they go. If a higher mobility had been used in the simulation the traps would probably have filled more uniformly throughout the grating period.

Unfortunately we were unable to obtain solutions for the case where transport lengths were on the order of the grating spacing. The numerical method was unstable except for mobilities which were several orders of magnitude lower than those we measured and reported in Chapter 5. In these simulations we found that for a grating spacing of 10 μm a value for the mobility higher than about 10^{-10} m^2/Vs resulted in solutions which were unstable. An integration technique other than the Runge-Kutta method may eliminate this problem.

6.5.2 Temperature Dependence

We attempted to simulate the temperature dependence of laser-induced gratings. Fig. 6.15 shows simulations which were performed at 300 K. The parameters were identical to those used in the simulation shown in Fig. 6.13 except for the temperature. No attempt was made to compensate for the temperature dependence of

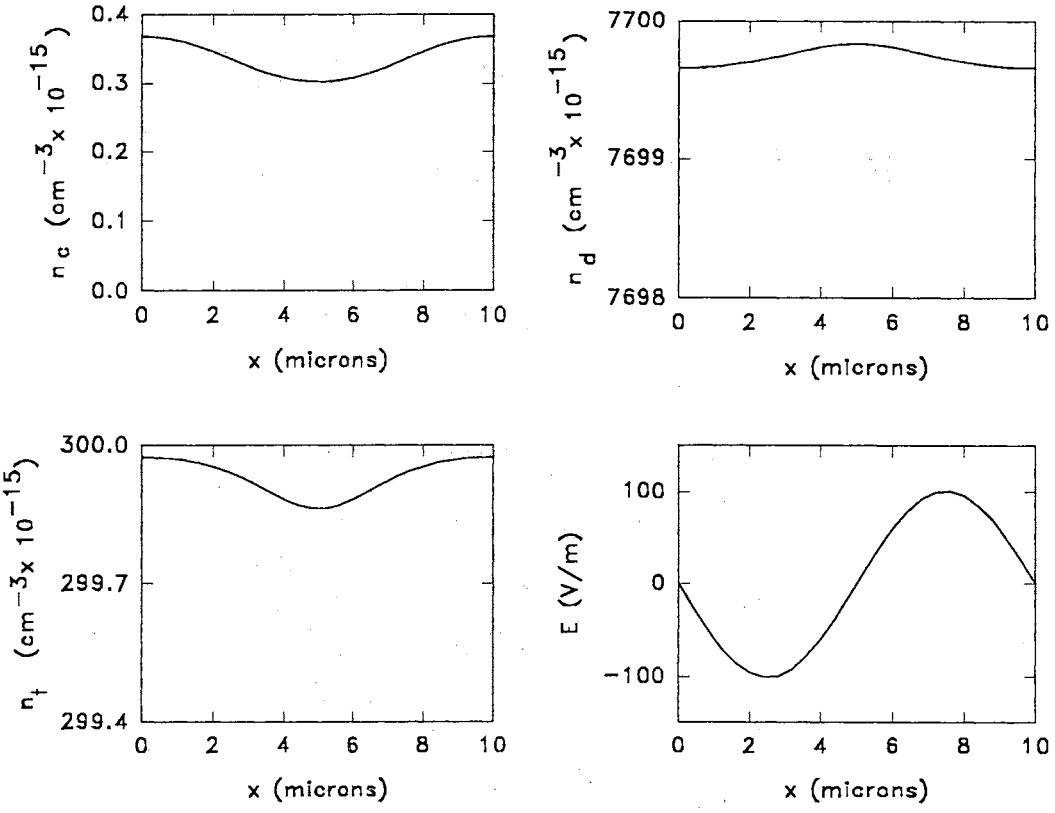

Figure 6.12: This figure shows the spatial dependence of the carrier concentrations and the electric field for m = 0.1 at 80 K.

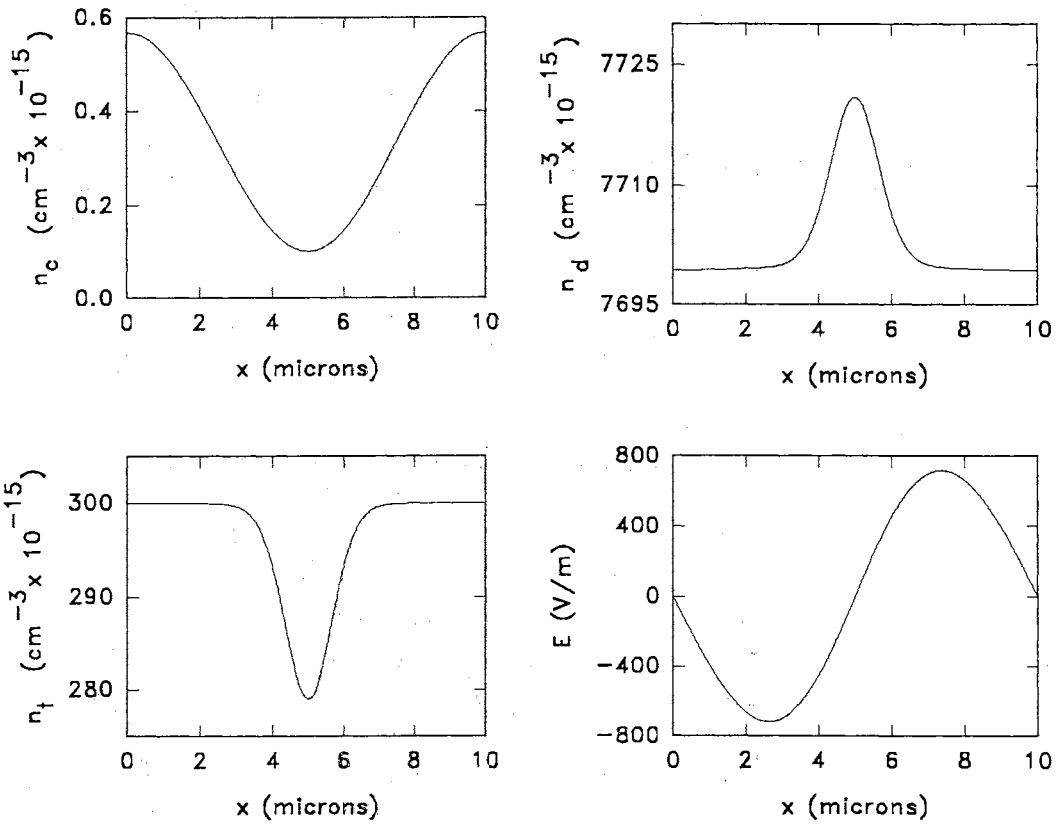

Figure 6.13: This figure shows the spatial dependence of the carrier concentrations and the electric field for m = 0.7 at 80 K.

parameters such as the mobility or frequency factor. Unfortunately, we were unable to simulate the temperature dependence with this model as we found that the simulated space-charge field was always larger at 300 K than at 80 K. Experiments show that the diffraction efficiency and, therefore, the space-charge field increases as the temperature is decreased. Figs. 6.14 and 6.15 show why the simulations don't behave this way. At 80 K the traps fill completely, so that they don't contribute to the space-charge field at all. Also, the modulation in the donor concentration is very small. In the simulation performed for 300 K, however, the traps aren't saturated and there is a spatial variation in the concentration. There is also a much larger modulation in the donor concentration resulting in a larger space-charge field than at 80 K. It may be possible to change the temperature dependence of the simulations by increasing the trap concentration, so that it is greater than the donor concentration. This is probably not physically reasonable, however, as the donor concentration has been reported to be on the order of 10^{25} m^{-3} whereas the trap concentrations which we measured were on the order of 10^{23} m^{-3} at most [80]. For this reason we did not perform any simulations with the trap concentration greater than the donor level concentration.

Our inability to reproduce the correct temperature dependence in the simulations may be partly due to the parameters which were used in the simulations. In order for the solutions to be stable we had to use a very low value for the mobility of 10^{-7} cm^2/Vs. The actual mobility at 300 K is about 0.11 cm^2/Vs, six orders of magnitude larger. We don't know the value of the mobility at 80 K.

Another possibility is that the model shown in Fig. 6.10 is too simple to reproduce the temperature dependent behavior of laser-induced gratings. The addition of a second trap which differs in activation energy from the first trap may be necessary.

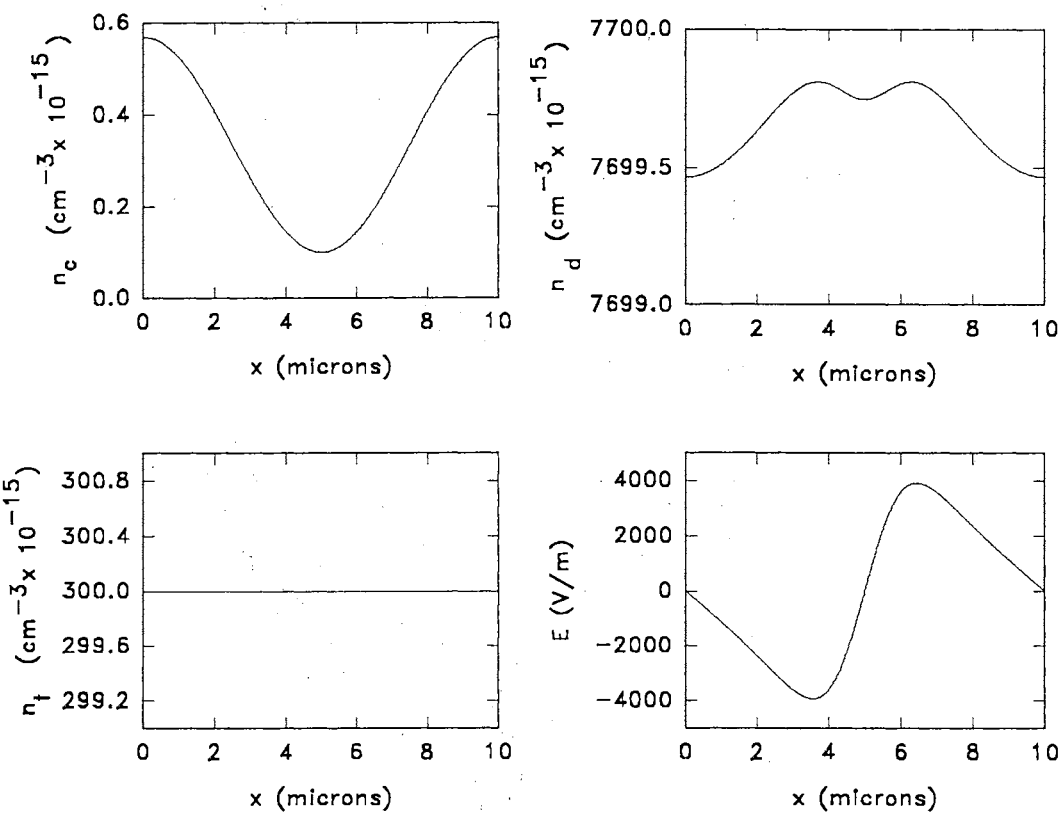

Figure 6.14: This figure shows the spatial dependence of the carrier concentrations and the electric field for m = 0.7 at 80 K.

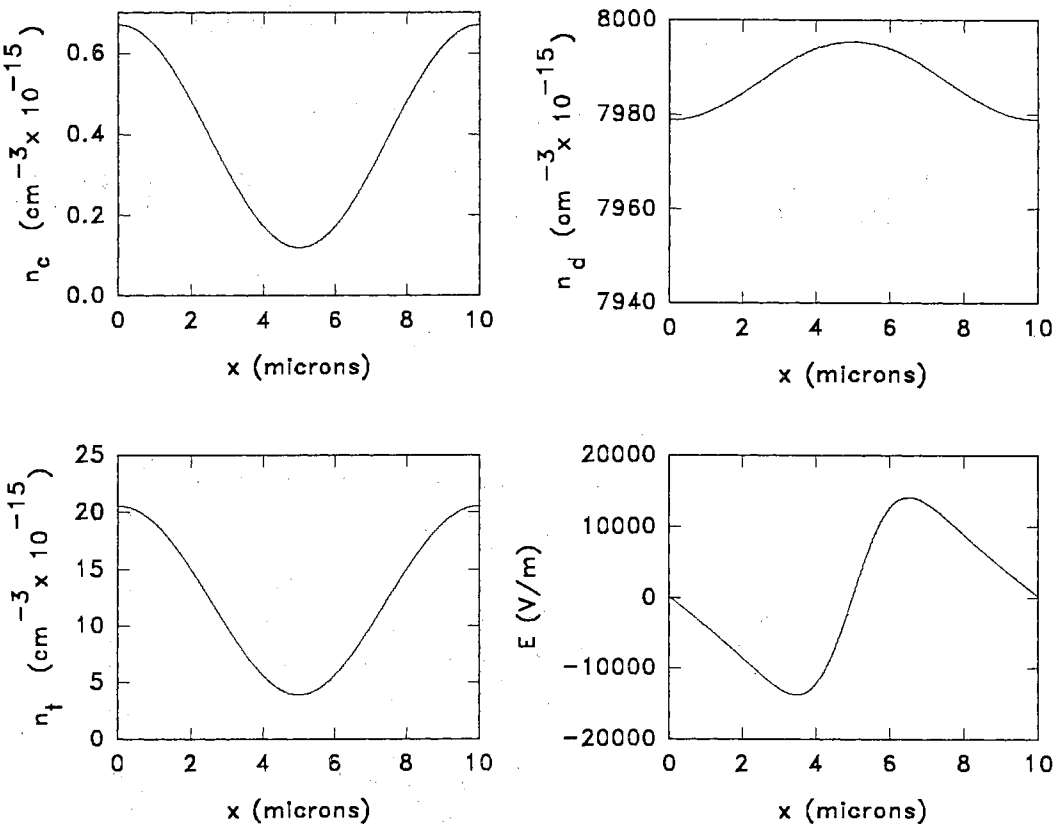

Figure 6.15: This figure shows the spatial dependence of the carrier concentrations and the electric field for m = 0.7 at 300 K.

6.6 Summary

We measured the temperature dependent behavior of laser-induced gratings in BGO. As the temperature is reduced the grating strength increases and the dark decay slows down. Our results show that the primary thermal decay of gratings in BGO agrees with the annealing of photoconductivity bands and occurs over the same temperature region as the largest TSC peak in the TSC spectra of BGO. In Chapter 5 we have shown, also, that this trap controls the drift mobility. These results indicate that trapping is playing an important role in the behavior of the photorefractive effect in this material. For this reason simulations of laser-induced gratings in BGO should include trapping levels in addition to the deep donor which acts as the source of electrons. In addition, a method for solving rate equations describing the photorefractive effect without approximations was presented.

Chapter 7

Conclusions

This dissertation has presented the results of a detailed study of the trapping levels which are important to the photorefractive behavior of $Bi_{12}GeO_{20}$ and $Bi_{12}SiO_{20}$. The results of optical absorption measurements show that there is an absorption shoulder due to a level about 2.7 eV from the band-edge. This level has been attributed to Bi^{3+} on a tetrahedral (Ge or Si) site. Doping with Ga or Al lowers the Fermi Level compensating the deep donor with a corresponding reduction in the absorption shoulder. By illuminating with light of the proper energy electrons are excited out of the donor level to the conduction band where they are trapped into a variety of trapping levels. This process results in additional (photochromic) absorption and photoconductivity bands.

Thermally stimulated conductivity measurements also show that there are a large number of trapping states in the forbidden band. The largest TSC peak appears between about 120 K and 180 K in undoped BGO and between 120 K and 160 K in 2% Ga-doped BGO. In order to fit these peaks we had to assume that the activation energy was not single-valued, but instead was characterized by a distribution of activation energies. We found that in undoped BGO two peaks were needed to obtain a good fit. The activation energies of these peaks were about 0.24 eV and 0.29 eV and the widths of the distribution were about 0.05 eV. In Ga-doped only one peak was needed for a good fit. The resulting activation energy was $\sim$0.29 eV and the

distribution width was 0.09 eV. Unfortunately, the defects which cause these states are unknown.

We performed thermoluminescence measurements simultaneously to the TSC measurements and found that the TL signals are very weak. Essentially no TL is observable after illuminating with sub-band-gap light. Band-edge light, however, produces weak TL signals. This suggests that the radiative recombination site is probably not empty donor states.

We measured mobilities in BGO and BSO between about 210 K and 300 K using the time-of-flight technique. We found that the mobility is exponentially dependent on temperature and the the results of fitting the current transients show that the shape of the transients is consistent with that expected for a Gaussian packet of carriers traveling through the sample. The Gaussian shape of the packet probably arises from the carriers undergoing multiple trapping and detrapping events during their transit. From the fitting procedure we obtain a value for the average drift velocity with which the carriers in the packet travel and from this drift velocity we compute the average mobility. Values of the mobility in undoped BGO range from about 6.1×10^{-4} cm^2/Vs at 210 K to 0.11 cm^2/Vs at 300 K. Our fitting procedure also provided an estimate of the width of the carrier packet. From the temperature dependence of the drift mobility and the width of the carrier packet we found that the trap limiting the mobility over the temperature range from 200 K to 300 K is the same one which causes the dominant peak in the TSC spectra between 120 K and 180 K.

The results of photorefractive measurements show, also, that this defect is the dominant defect in grating writing. We studied the saturation value of the diffraction efficiency vs. temperature and the thermal stability of gratings written at low temperature. We correlated these temperature dependencies with the TSC signals and

the annealing of the photoconductivity bands. We found that the thermal decay of laser-induced gratings in BGO show a major decay over the same temperature region as the main TSC feature between 120 and 180 K. This indicates that this trap plays a major part in the photorefractive response of BGO at low temperature. Unfortunately, at higher temperatures the photorefractive effect is very weak and the dark decay is very fast.

7.1 Future Work

In order for BGO and BSO to be viable materials for many photorefractive applications a deep trap level that is stable for long times at room temperature is needed. Unfortunately, none of the undoped samples or samples doped with Ga, Al or Fe have large, stable photorefractive signals at room temperature. This severely limits their use in applications. For this reason other dopants need to be studied. One dopant that looks promising is chromium. BGO doped with Cr shows a room temperature photorefractive signal which is much longer lived than undoped BGO or BGO doped with any of Ga, Al or Fe. It has been claimed [100] that the primary mechanism of the "dark" decay of the photorefractive signal of Cr doped BGO is optical erasure by the read beam. The deep trap which Cr seems to introduce should be studied using methods such as thermally stimulated conductivity and thermoluminescence.

In addition to the experimental work, the numerical method presented in Chapter 6 should be further refined. An integration technique other than the Runge-Kutta method may eliminate a lot of the difficulties with the stability of the method which were discussed in Chapter 6. A numerical technique which could be used to solve the equations describing the photorefractive effect using a realistic multi-trap model with both electrons and holes would help gain insight into the carrier kinetics during grating writing and erasure.

Bibliography

[1] A. Ashkin, G.D. Boyd, J. M. Dziedzik, R. G. Smith, A.A. Ballman and K. Nassau, Appl. Phys. Lett. **9**, 72 (1966).

[2] W. E. Moerner and S. M. Silence, Chem. Rev. **94**, 127 (1994).

[3] P. Gunter, Phys. Rep. **93**, 199 (1982).

[4] S. L. Hou and D. S. Oliver, Appl. Phys. Lett. **18**, 325 (1971).

[5] J. F. Heanue, M. C. Bashaw and L. Hesselink, Science **265**, 749 (1994).

[6] M. A. Neifeld and D. Psaltis, Appl. Opt. **32**, 4398 (1993).

[7] G. A. Rakuljic and V. Leyva, Opt. Lett. **18**, 459 (1992).

[8] T. J. Hall, R. Jaura, L. M. Connors and P. D. Foote, Prog. Quant. Electr. **10**, 77 (1985).

[9] L. Liu and X. Liu, J. Appl. Phys. **72**, 337 (1992).

[10] L. Arizmendi, J. M. Cabrera and F. Agullo-Lopez, Int. J. Optoelect. **7**, 149 (1992).

[11] M. P. Petrov, S. I. Stepanov and A. V. Khomenko, *Photorefractive Crystals in Coherent Optical Systems*, Springer–Verlag, New York, 1991.

[12] A. A. Ballman, J. Crys. Growth **1**, 37 (1966).

[13] J. C. Brice, M. J. Hight, O. F. Hill and P. A. C. Whiffin, Phillips Tech. Rev. **37**, 250 (1977).

[14] L. G. Sillen, Arkiv Kemi, Min. Geol. **12A**, 1 (1937).

[15] S. C. Abrahams, P. B. Jamieson and J. L. Bernstein, J. Chem. Phys. **47**, 4034 (1967).

[16] J. L. Bernstein, J. Crystal Growth **1**, 45 (1967).

[17] P. V. Lenzo, E. G. Spencer and A. A. Ballman, Appl. Opt. **5**, 1688 (1966).

[18] A. Feldman, W. S. Brower, Jr. and D. Horowitz, Appl. Phys. Lett. **16**, 201 (1970).

[19] R. E. Aldrich, S. L. Hou and M. L. Harvill, J. Appl. Phys. **42**, 493 (1971).

[20] B. C. Grabmaier and R. Oberschmid, Phys. Stat. Sol. (a) **96**, 199 (1986).

[21] T. Sawada, T. Hirao, H. Ohara and K. Ujihara, Jap. J. Appl. Phys. **29**, 108 (1990).

[22] W. B. Leigh, et. al., J. Appl. Phys. **76**, 660 (1994).

[23] M. T. Harris, J. J. Larkin and J. J. Martin, Appl. Phys. Lett. **60**, 2162 (1992).

[24] S. L. Hou, R. B. Lauer and R. E. Aldrich, J. Appl. Phys. **44**, 2652 (1973).

[25] R. Oberschmid, Phys. Stat. Sol. (a) **89**, 263 (1985).

[26] J. J. Martin, I. Foldvari. and C. A. Hunt, J. Appl. Phys. **70**, 7554 (1991).

[27] D. Bloom and S. W. S. McKeever, J. Appl. Phys. **77**, 6511 (1995).

[28] D. W. Hart, et. al., J. Appl. Phys. **73**, 1443 (1993).

[29] D. W. Hart, C. A. Hunt and J. J. Martin, J. Appl. Phys. **73**, 3974 (1993).

[30] D. Petre, I. Pintilie, T. Botila and M. L. Ciurea, J. Appl. Phys. **76**, 2216 (1994).

[31] D. Just and T. Takamori, Mat. Sci. and Eng. **B9**, 469 (1991).

[32] T. Takamori and D. Just, J. Appl. Phys. **67**, 848 (1990).

[33] T. Takamori and D. Just, J. Appl. Phys. **68**, 5700 (1990).

[34] R. B. Lauer, J. Appl. Phys. **42**, 2147 (1971).

[35] J. A. Baquedano and J. M. Cabrera, Phys. Stat. Sol. (a) **118**, 497 (1990).

[36] I. Foldvari, et. al., Solid State Commun. **77**, 181 (1991).

[37] T. Takamori, J. Appl. Phys. **69**, 8222 (1991).

[38] D. E. Davies and J. J. Larkin, Appl. Phys. Lett. **67**, 188 (1995).

[39] H.-J. Reyher, U. Hellwig and O. Thiemann, Phys. Rev. B **47**, 5738 (1993).

[40] J.-M. Spaeth and F. Lohse, J. Phys. Chem. Solids **51**, 861 (1990).

[41] I. Foldvari, J. J. Martin, C. A. Hunt, R. C. Powell, R. J. Reeves and S. A. Holmstrom, Opt. Mat. **2**, 25 (1993).

[42] W. Wardzynski, M. Baran and H. Szymczak, Physica **111** B, 47 (1981).

[43] W. Wardzynski, H. Szymczak, K. Pataj, T. Lukasiewicz and J. Zmija, J. Phys. Chem. Solids **43**, 767 (1982).

[44] W. Wardzynski, H. Szymczak, M. T. Borowiec and K. Pataj, J. Phys. Chem. Solids **46**, 1117 (1985).

[45] H. J. von Bardeleben, J. Phys. D: Appl. Phys. **16**, 29 (1983).

[46] M. G. Jani and L. E. Halliburton, J. Appl. Phys. **64**, 2022 (1988).

[47] J. A. Weil, Phys. Chem. Minerals, **10**, 149 (1984).

[48] G. F. J. Garlick and A. F. Gibson, Proc. Phys. Soc. **60**, 574 (1948).

[49] W. Hoogenstraaten, Phillips Res. Reports **13**, 515 (1958).

[50] R. Chen, J. Appl. Phys. **40**, 570 (1969).

[51] S.W.S. McKeever, Thermoluminescence of Solids, Cambridge University Press (1985).

[52] A. C. Lewandowski and S. W. S. McKeever, Phys. Rev. B **43**, 8163 (1991).

[53] J. T. Randall and M. H. F. Wilkins, Proc. Roy. Soc. (London) **A184**, 366 (1945).

[54] R. Chen, N. Kristianpoller, Z. Davidson and R. Visocekas, J. Lumin. **23**, 293 (1981).

[55] T. Kikuchi, J. Phys. Soc. Japan **13**, 526 (1958).

[56] S. Dorendrajit Singh and R. K. Gartia, J. Phys. D **26**, 119 (1993).

[57] W. F. Hornyak and R. Chen, J. of Luminescence **44**, 73 (1989).

[58] P. N. Keating, Proc. Phys. Soc. (London) **78**, 1408 (1961).

[59] S. W. S. McKeever, Phys. Stat. Sol. (a) **62**, 331 (1980).

[60] H. Gobrecht and D. Hofmann, J. Phys. Chem. Sol. **27**, 509 (1966).

[61] A. C. Lewandowski, B. G. Markey and S. W. S. McKeever, Phys. Rev. B **49**, 8029 (1994).

[62] A. Halperin and A. A. Braner, Phys. Rev. **117**, 408 (1960).

[63] R. H. Bube, *Photoelectric Properties of Semiconductors*, Cambridge University Press, Cambridge, 1992.

[64] A. Ennouri, M. Tapiero, J. P. Vola, and A. P. Zielinger, J. Appl. Phys. **74**, 2180 (1993).

[65] J. P. Partanen, J. M. C. Jonathan and R. W. Hellwarth, Appl. Phys. Lett. **57**, 2404 (1990).

[66] B. Kh. Kostyuk, A. Yu. Kudzin and G. Kh. Sokolyanskii, Sov. Phys. Solid State **22**, 1429 (1980).

[67] H. Scher, E. W. Montroll, Phys. Rev. B **12**, 2455 (1975).

[68] D. Allan, Phil. Mag. B **38**(4), 381 (1978).

[69] P. A. Bayley and J. M. Marshall, Phil. Mag. B **73**, 429 (1996).

[70] W. E. Spear and H. Steemers, Phil. Mag. B **47**, L77 (1983).

[71] P. B. Kirby and William Paul, Phys. Rev. B **25**, 5373 (1982).

[72] G. Pfister, Phys. Rev. Lett. **36**, 271 (1976).

[73] J. G. Ruch and G. S. King Phys. Rev. **174**, 921 (1968).

[74] R. K. Ahrenkiel, et. al., Appl. Phys. Lett. **49**, 725 (1986).

[75] C. Canali, M. Martini and G. Ottaviani, Phys. Rev. B **4**, 422 (1971).

[76] C. Cavalleri, G. Fabri, E. Gatti and V. Svelto, Nucl. Instr. Methods **21**, 177 (1963).

[77] R. H. Bube, *Photoconductivity of Solids*, John Wiley and Sons, New York, 1960.

[78] J. C. Scott, L. Th. Pautmeier and L. B. Schein, Phys. Rev. B **46**, 8603 (1992).

[79] D. W. Marquardt, J. Soc. Indust. Appl. Math. **11**, 431 (1963).

[80] D. Bloom and S. W. S. McKeever, J. Appl. Phys. **77**, 6521 (1995).

[81] R. B. Lauer, J. Appl. Phys. **45**, 1794 (1974).

[82] S. G. Lipson and P. Nisenson, Appl. Opt. **13**, 2052 (1974).

[83] D. C. Craig and N. C. Stephenson, J. Sol. St. Chem. **15**, 1 (1975).

[84] W. Rehwald, F. Frick, G. K. Lang and E. Meier, J. Appl. Phys. **47**, 1292 (1975).

[85] A. E. Attard, Appl. Opt. **27**, 232 (1988).

[86] T. Tiedje, Semiconductors and Semimetals **21**, 207 (1984).

[87] V. K. Gorchakov, V. V. Kutsaenok, and V. T. Potapov, Opt. Spectrosc. **67**, 380 (1989).

[88] I. Foldvari, J. J. Martin, C. A. Hunt, R. C. Powell and R. R. Reeves, J. Appl. Phys. **74**, 783 (1993).

[89] N. V. Kukhtarev, Sov. Tech. Phys. Lett., **2**, 438 (1976).

[90] N. V. Kukhtarev, V. B. Markov, S. G. Odulov, M. S. Soskin and V. L. Vinetskii, Ferroelectrics **22**, 949 (1979).

[91] G. C. Valley, J. Appl. Phys., **59**, 3363 (1986).

[92] M. G. Moharam, T. K. Gaylord, R. Magnusson and L. Young, J. Appl. Phys., **50**, 5642 (1979).

[93] F. P. Strohkendl and R. W. Hellwarth, J. Appl. Phys., **62**, 2450 (1987).

[94] E. Serrano, V. Lopez, M. Carrascosa and F. Agullo-Lopez, J. Opt. Soc. Am. B **11**, 670 (1994).

[95] E. Serrano, V. Lopez, M. Carrascosa and F. Agullo-Lopez, J. Quant. Elect. **11**, 875 (1994).

[96] J. G. Murillo, L. F. Magana, M. Carrascosa and F. Agullo-Lopez, J. Appl. Phys. **78**, 5686 (1995).

[97] M. Peltier and F. Micheron, J. Appl. Phys. **48**, 3683 (1977).

[98] D. M. Kim, R. R. Shah, T. A. Rabson and F. K. Tittel, Appl. Phys. Lett. **28**, 338 (1976).

[99] G. A. Brost, J. Opt. Soc. Am. B **9**, 1454 (1992).

[100] Dr. Joel Martin private communication.

2

VITA

Danning Wilford Bloom

Candidate for the Degree of

Doctor of Philosophy

Thesis: ELECTRICAL AND OPTICAL CHARACTERIZATION OF DEFECT LEVELS IN $Bi_{12}GeO_{20}$ AND $Bi_{12}SiO_{20}$

Major Field: Physics

Biographical:

Personal Data: Born in Boulder, Colorado, on April 28, 1967, the son of Danning W. Bloom and Susan R. Bloom.

Education: Received Bachelor of Arts degree in Physics from St. Cloud State University, St. Cloud, Minnesota in May 1989. Completed the requirements for the Doctor of Philosophy degree in Physics at Oklahoma State University in May 1997.

Professional Experience: Teaching Assistant from June 1990 to May 1992; Research Assistant from May 1992 to the present.

Professional Memberships: American Physical Society.